



R e m c o m

# Radio Propagation Prediction Software for Complex Mixed Path Physical Channels

14 August 2006

Sponsored by

Defense Advanced Research Projects Agency (DoD)

ATO

ARPA Order Nr. S241-20

Issued by U.S. Army Aviation and Missile Command Under

Contract No. W31P4Q-04-C-R245

By

Remcom Inc.

Stephen A. Fast

Principal Investigator

315 S. Allen St., Suite 222

State College, PA 16801-4850

Effective 24 Jun 2004

Mixed Path Propagation

Expires 28 Sept 2006

Reporting Period: 24 Jun 2004 – 28 Sept 2006

**DISCLAIMER – The views and conclusions contained in this document are those of the authors and should not be interpreted as representing the official policies, either express or implied, of the Defense Advanced Research Projects Agency or the U.S. Government.**

Approved for public release; distribution unlimited

REPORT DOCUMENTATION PAGE				Form Approved OMB No. 0704-0188	
<p>The public reporting burden for this collection of information is estimated to average 1 hour per response, including the time for reviewing instructions, searching existing data sources, gathering and maintaining the data needed, and completing and reviewing the collection of information. Send comments regarding this burden estimate or any other aspect of this collection of information, including suggestions for reducing the burden, to Department of Defense, Washington Headquarters Services, Directorate for Information Operations and Reports (0704-0188), 1215 Jefferson Davis Highway, Suite 1204, Arlington, VA 22202-4302. Respondents should be aware that notwithstanding any other provision of law, no person shall be subject to any penalty for failing to comply with a collection of information if it does not display a currently valid OMB control number.</p> <p><b>PLEASE DO NOT RETURN YOUR FORM TO THE ABOVE ADDRESS.</b></p>					
1. REPORT DATE (DD-MM-YYYY) 19-09-2006		2. REPORT TYPE Final Scientific and Technical Report		3. DATES COVERED (From - To) 24-06-2004 to 26-09-2006	
4. TITLE AND SUBTITLE Radio Propagation Prediction Software for Complex Mixed Path Physical Channels				5a. CONTRACT NUMBER W31P4Q-04-C-R245	
				5b. GRANT NUMBER	
				5c. PROGRAM ELEMENT NUMBER	
6. AUTHOR(S) Stephen A. Fast				5d. PROJECT NUMBER RTW9T 04	
				5e. TASK NUMBER	
				5f. WORK UNIT NUMBER	
7. PERFORMING ORGANIZATION NAME(S) AND ADDRESS(ES) Remcom, Inc. 315 S. Allen Street, Suite 222 State College, PA 16801-4850				8. PERFORMING ORGANIZATION REPORT NUMBER REM-MxPth-Final	
9. SPONSORING/MONITORING AGENCY NAME(S) AND ADDRESS(ES) US Army Aviation & Missile Command AMSAM-AC-RD-AY Linda Madden Redstone Arsenal, AL 35898-5280				10. SPONSOR/MONITOR'S ACRONYM(S)	
				11. SPONSOR/MONITOR'S REPORT NUMBER(S)	
12. DISTRIBUTION/AVAILABILITY STATEMENT Approved for public release; distribution unlimited.					
13. SUPPLEMENTARY NOTES					
14. ABSTRACT <p>It has become increasingly clear that the customers for the Mixed Path project desire API to the various Wireless InSite calculation engines. Thus the WI engines can be incorporated into tools such as OPNET and QualNet for network analysis or into various signal processing software. For network analysis all that is required is an extremely fast computing propagation model that captures the mixed path propagation at an acceptable resolution and fidelity. For signal processing analyses, the propagation channel is required. Thus a time domain capability API is required within WI. Lastly an easy to use graphics GUI is required by all of WI customers to allow the scene to be more easily rendered and modified. Thus the thrust for this effort was to develop rapid urban ray tracing and propagation computation methods that compute urban propagation predictions in less than one millisecond with an API that allows easy integration into network modeling tools. This was accomplished and an urban propagation API is now available for network simulation users.</p>					
15. SUBJECT TERMS <p>Urban Propagation, Ray Tracing, Urban Terrain, Uniform Theory of Diffraction, Parabolic Equation Models, Environmental Data Support, Graphical User Interface, Network simulation</p>					
16. SECURITY CLASSIFICATION OF:			17. LIMITATION OF ABSTRACT  UU	18. NUMBER OF PAGES  91	19a. NAME OF RESPONSIBLE PERSON Stephen A. Fast
a. REPORT  U	b. ABSTRACT  U	c. THIS PAGE  U			19b. TELEPHONE NUMBER (Include area code) 814-861-1299 ext. 260



## **Table of Contents**

1. Technical.....	1
1.1. Technical Objectives Accomplished.....	1
1.1.1. Task Progress .....	1
1.2. Immediate Plans.....	14
1.3. Technical Problems.....	14
1.3.1. Technical Problems Encountered .....	14
1.3.2. Cost/Schedule Impact .....	14
1.3.3. Steps taken to Remedy Problems.....	14
1.4. Resolutions to Previous Technical Problems.....	14
1.5. Recommendations.....	14
2. Cost Incurred and Outstanding Commitments.....	15
2.1. Current Costs Incurred .....	15
2.2. Cumulative Costs Incurred .....	15
2.3. Funds Remaining .....	15
2.4. Spending Costs.....	15
3. Project Management Review (PMR).....	16
3.1. Agendas.....	16
3.2. Presentation Materials.....	16
3.3. Minutes .....	16
4. Appendices Technical Reports .....	16
4.1. Vertical Plane Urban Propagation Model.....	16
4.1.1. Modifications and Extensions of Conventional Methods of Vertical Plane Urban Propagation .....	16
4.1.2. Urban Terrain Geometrical and Other Considerations for Implementation of Proposed Methods .....	22
4.1.3. Loss Evaluation Process .....	27
4.2. Fast Urban Predictions.....	31
4.2.1. Initial Effort .....	31
4.2.2. Technical Details .....	38
4.2.3. MITRE Model.....	38
4.2.4. Other models.....	49
4.3. Building Simplification.....	49
4.3.1. Two Dimensional.....	49
4.3.2. Three Dimensional Simplification.....	55
4.4. Extended Semi-Empiricism for (Complex) Soil Permittivity.....	56
4.4.1. Preface.....	56
4.4.2. Introduction.....	56
4.4.3. Empirical Algorithm for Frequency Range 1400-18000 MHz.....	57
4.4.4. Independent Semi-Empirical Algorithms for Frequency Ranges 300-1300 MHz and 1400-18000 MHz .....	62
4.4.5. (Unified) Semi-Empirical Algorithm for Frequency Range 300-14000 MHz .....	63
4.4.6. Applied Linear Regression Analysis in the Frequency Range 1-50 MHz .....	69
4.4.7. Projected Scaling to Measured Data in the Frequency Range .01-100 MHz .....	76

4.4.8.	Performance of the Model over Full Frequency .....	78
4.4.9.	REFERENCES .....	86

## **1. Technical**

The initial focus of the phase two effort is towards developing methods, tools and databases to support the various environmental data required by the RF propagation prediction models. Another aspect is to build upon the Phase I accomplishments to develop interfaces that allow different models to be coupled together in order to do mixed path propagation computations. Lastly, in order for a mixed path propagation model to be truly useful for many of today's problems, methods must be developed to couple the energy radiated from antennas to propagation models. This is especially necessary as the link budget equation becomes no longer applicable.

### **1.1. Technical Objectives Accomplished**

#### **1.1.1. Task Progress**

Over the past few months it has become increasingly clear that the customers for the Mixed Path project desire API to the various Wireless InSite calculation engines. This is because then the WI engines can be incorporated into too such as OPNET and QualNet for network analysis or into various signal processing software. For the network analysis all that is required is an extremely fast computing propagation model that captures the mixed path propagation at an acceptable resolution and fidelity. For signal processing analyses, the propagation channel is required. Thus a time domain capability API is required within WI. Lastly an easy to use graphics GUI is required by all of WI customers to allow the scene to be more easily rendered and modified. Further Wireless InSite customers require the ability to run many different permutations and combinations of scenarios. Thus scripting is being developed for Wireless InSite. Thus this report shall focus on accomplishments in these areas.

##### **1.1.1.1. Fast Urban API**

###### **1.1.1.1.1. Background**

In order for Wireless InSite to interface to network simulations such as OPNET and QualNet, it is necessary for an API to be constructed for the propagation models. An API could be made directly to point to point version of the fast propagation models. The calculation API originally conceived for newly developed faster ray based methods to support rapid computation.

###### **1.1.1.1.2. Status**

This capability is to be available as a commercial product in August 2006.

###### **1.1.1.1.3. Technical Details**

See Section 4.2

##### **1.1.1.2. Faster urban propagation models**

###### **1.1.1.2.1. Background**

In order to support rapid urban calculations suitable for integration into networks simulations, a rapid, perhaps lower fidelity, urban propagation models are required. This model shall be site

specific. Remcom's high fidelity models found in Wireless InSite could be used to form the basis of semi-empirical models or be used for validation.

#### **1.1.1.2.2. Current Status**

Remcom's vertical plane urban propagation model is complete and integrated into the fast urban API.

#### **1.1.1.2.3. Technical Details**

See Section 4.1.

### **1.1.1.3. Two Dimensional Building Simplification**

#### **1.1.1.3.1. Background**

While Wireless InSite currently has a two dimensional building simplification algorithm, it requires extensive user interaction and proficiency. Further the current simplification metrics must be applied one building at a time. This makes building simplification arduous and time consuming. This task is to find better methods that require little user interaction and can be applied over the entire area of interest.

#### **1.1.1.3.2. Current Status**

This was integrated into Wireless InSite.

#### **1.1.1.3.3. Technical Details**

See Section 4.3.1.

### **1.1.1.4. Three Dimensional Building Simplification**

#### **1.1.1.4.1. Three Dimensional Simplification Background**

Often the buildings in an urban or suburban scenario are too small/short for the urban canyon's propagation methods to function properly. Further time consuming 3-dimensional ray tracing computations are directly related to the number of faces found in the scenario. Thus it is desired to find methods to reduce the number of faces in the scenario to a reasonable yet representative realization.

#### **1.1.1.4.2. Three Dimensional Simplification Background Status**

Because of the technical complexity, this task was discontinued.

#### **1.1.1.4.3. Technical Details**

See Section 4.3.2.

### **1.1.1.5. Soil Dielectrics**

#### **1.1.1.5.1. Background**

In order to support an easy method to determine the world wide ground dielectric properties, Remcom investigated possible methods to compute the dielectric constants from the soil constituents and moisture content.

#### **1.1.1.5.2. Current Status**

The algorithms are complete. Software to determine the opil constituents worldwide is complete.

#### **1.1.1.5.3. Technical Details**

See Section 4.4.

#### **1.1.1.6. Wireless InSite Optimization**

The goal is to significantly reduce the computation time required by Wireless InSite's full three-dimensional (3D) propagation model. This will be accomplished by decreasing the run time of the SBR ray tracing procedure. Other goals include creating a calculation engine executable for a 32-bit Linux operating system, and to enable parallel processing on a Linux cluster.

##### **1.1.1.6.1. Reduce Run Time of Full 3D Propagation Model**

Tables 1 and 2 in Section 1.2.6 shows the speedup for version 2.2, and for the version of 2.3 that we are currently testing. The speedup for the 2.2 version is usually in the 5-9 range and generally improves slightly as the number of buildings increases. The speedup for version 2.3 is currently in the 7-13 range. We hope to improve that a little more before we release version 2.3 at the end of May.

##### **1.1.1.6.2. Shapefile Import**

Although this was no included in the current contract, we have decided to add the ability to version 2.3 to import building data from shapefiles which use the polygon and polygon Z shape types. We will import the data directly from the shapefile, not from the intermediate DXF file that you needed to use with version 2.1. We will support files with building coordinates in longitude/latitude, UTM and local Cartesian frames that are not geo-referenced. We are still investigating whether we will be able to import data using other map projections. Version 2.2 does not have any capabilities for directly importing shapefiles.

#### **1.1.1.7. Calculation Engine for Linux Operating Systems**

The 2.3 calculation engine will run on a computer with Linux operating system. The software can be licensed using either a node locked license or a floating license. The calculation engine can be executed either from the command line or by means of a script file. The name of the project file to run is one of the command line options that the user can specify. The GUI will still only run on a Windows operating system.

##### **1.1.1.7.1. Running Calculations on Linux Clusters**

The 2.3 Wireless InSite calculation engine now runs on a Linux cluster. The GUI will generate script files for submitting jobs to a cluster using PBS scheduler. All output can be viewed using the GUI once the files are moved to a location which the GUI can access.

#### **1.1.1.8. Building Pre-Processor**

We have made a number of improvements to the building preprocessor (building simplifier). Many of the new capabilities are available in version 2.2

#### **1.1.1.9. Test Cases and Run Time Benchmarks**

We have developed several test cases for comparing the new run times to the 2.1 run times in urban environments. The test cases use a variety of building shapes, transmitter heights and locations, and numbers of receivers. The test cases are also used to verify that the run time reductions are not affecting the accuracy of the results. Run times for downtown Chicago test cases are discussed below.

##### **1.1.1.9.1. Description**

The section of downtown Chicago used for the run time testing is shown in Figures 1 and 2. This area is about 1 km x 1 km and contains about 100 buildings with 2200 facets. The locations of the five transmitter sites are indicated by the green boxes. The calculations were performed for 1850 receiver locations spaced at 5 meters along the main streets in this area with only one transmitter active at a time. The path loss predictions along the streets for each transmitter location are shown in Figures 3-7.

The run times for each transmitter location were recorded using versions 2.1 and 2.2, and the preliminary version of 2.3. The run times and the computed speedups for versions 2.2 and 2.3 relative to 2.1 are shown in Table 1 and 2. The average speedup for version 2.2 relative to version 2.1 is about 7.0 for the total run time, and about 8.0 for just the ray-tracing portion of the calculation. The average speedup for version 2.3 relative to version 2.1 is about 10.4 for the total time, and about 11.4 for just the ray tracing.



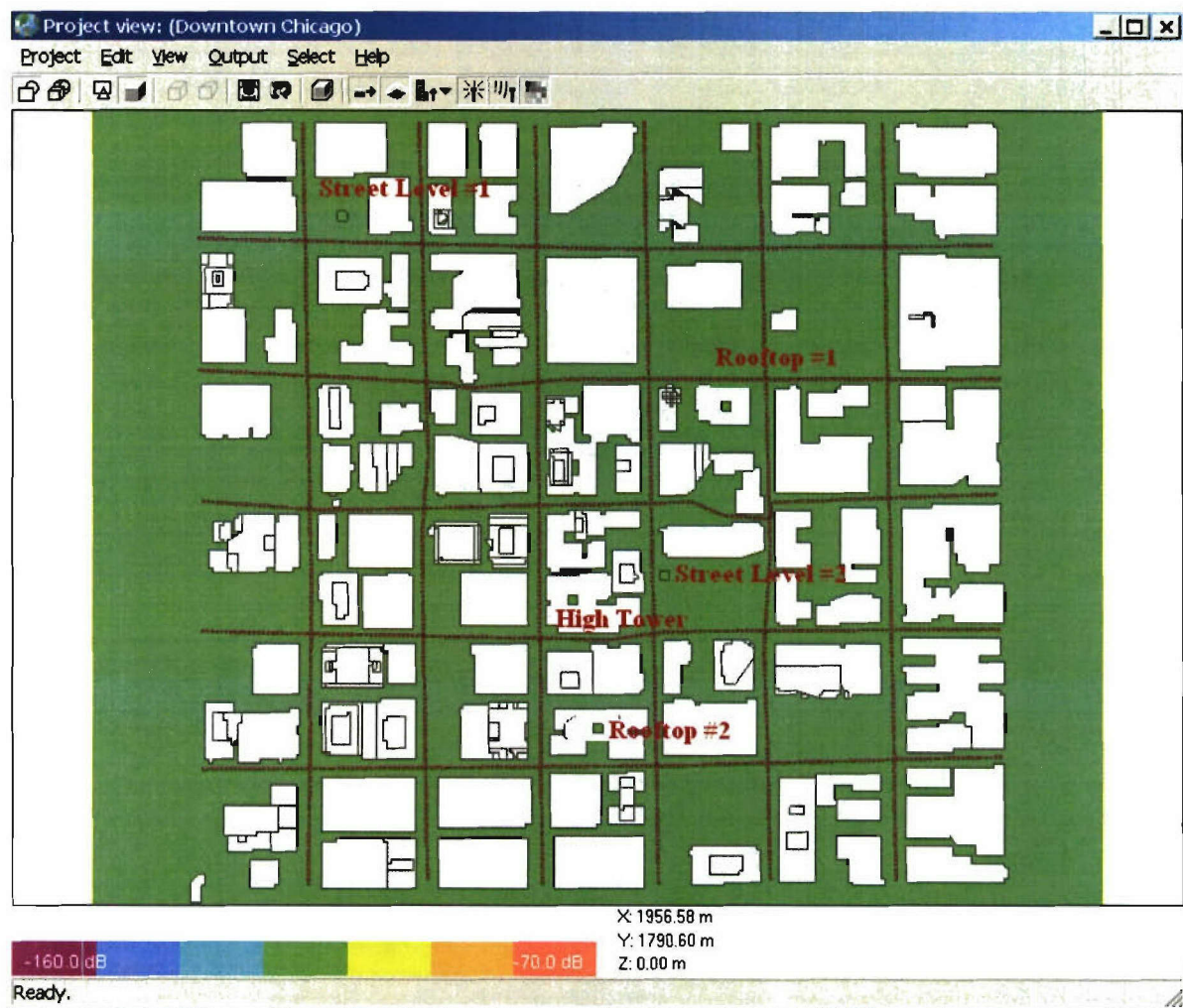


Figure 1: Plan view of downtown Chicago area with the transmitter and receiver locations

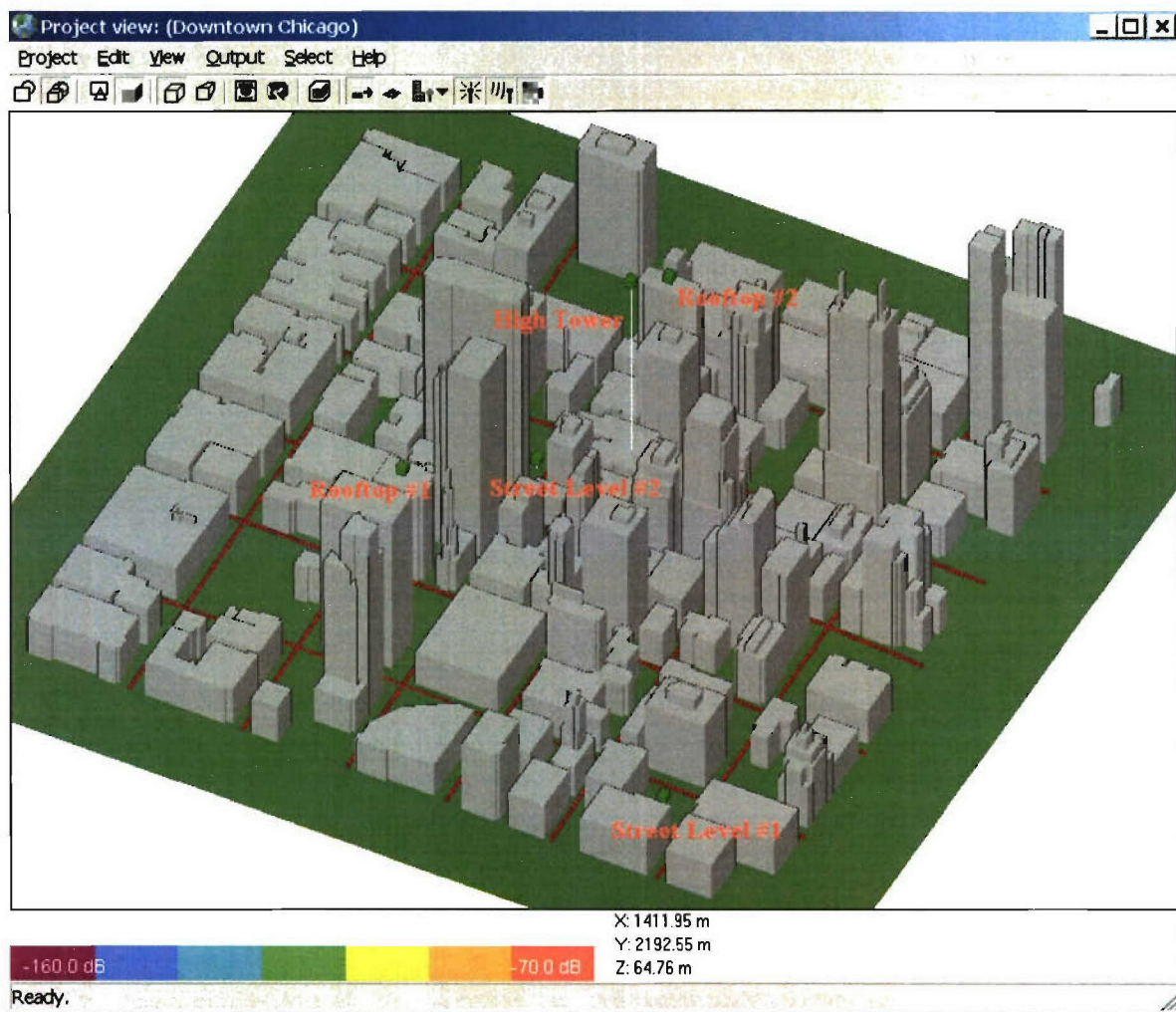


Figure 2: Three-dimensional view of downtown Chicago area with transmitter and receiver locations

#### 1.1.1.9.2. Runtime and Speedup

#### 1.1.1.9.3. Version 2.2 Run Time and Speedup

Table 1: Run times and speedup for version 2.2 on Downtown Chicago test cases

Test Case	Total Run Time (h:m:s)			Ray Tracing Run Time (h:m:s)		
	v2.1	v2.2	Speedup	v2.1*	v2.2	Speedup*
Street Level Tx #1	8:57:42	1:28:42	6.1	8:52:05	1:24:03	6.3
Street Level Tx #2	14:14:00	2:25:06	5.9	14:06:42	2:13:15	6.4
Rooftop Tx #1	10:32:00	1:26:52	7.3	10:22:38	1:14:44	8.3
Rooftop Tx #2	8:31:00	1:05:19	7.8	8:24:01	0:56:15	9.0
High Tower Tx #1	13:58:00	1:39:56	8.4	13:54:07	1:36:47	8.6

\* Estimate

#### 1.1.1.9.4. Version 2.3a Run Time and Speedup

**Table 2: Run times and speedup for version 2.3a on Downtown Chicago test cases**

Test Case	Total Run Time (h:m:s)			Ray Tracing Run Time (h:m:s)		
	v2.1	v2.3a	Speedup	v2.1*	v2.3a	Speedup*
Street Level Tx #1	8:57:42	1:04:12	8.4	8:52:05	1:01:01	8.7
Street Level Tx #2	14:14:00	1:34:44	9.0	14:06:42	1:23:50	10.1
Rooftop Tx #1	10:32:00	0:59:00	10.7	10:22:38	0:47:37	11.4
Rooftop Tx #2	8:31:00	0:45:16	11.3	8:24:01	0:36:39	13.1
High Tower Tx #1	13:58:00	1:05:48	12.7	13:54:07	1:00:00	13.9

\* Estimate



#### 1.1.1.9.5. Path Loss Predictions

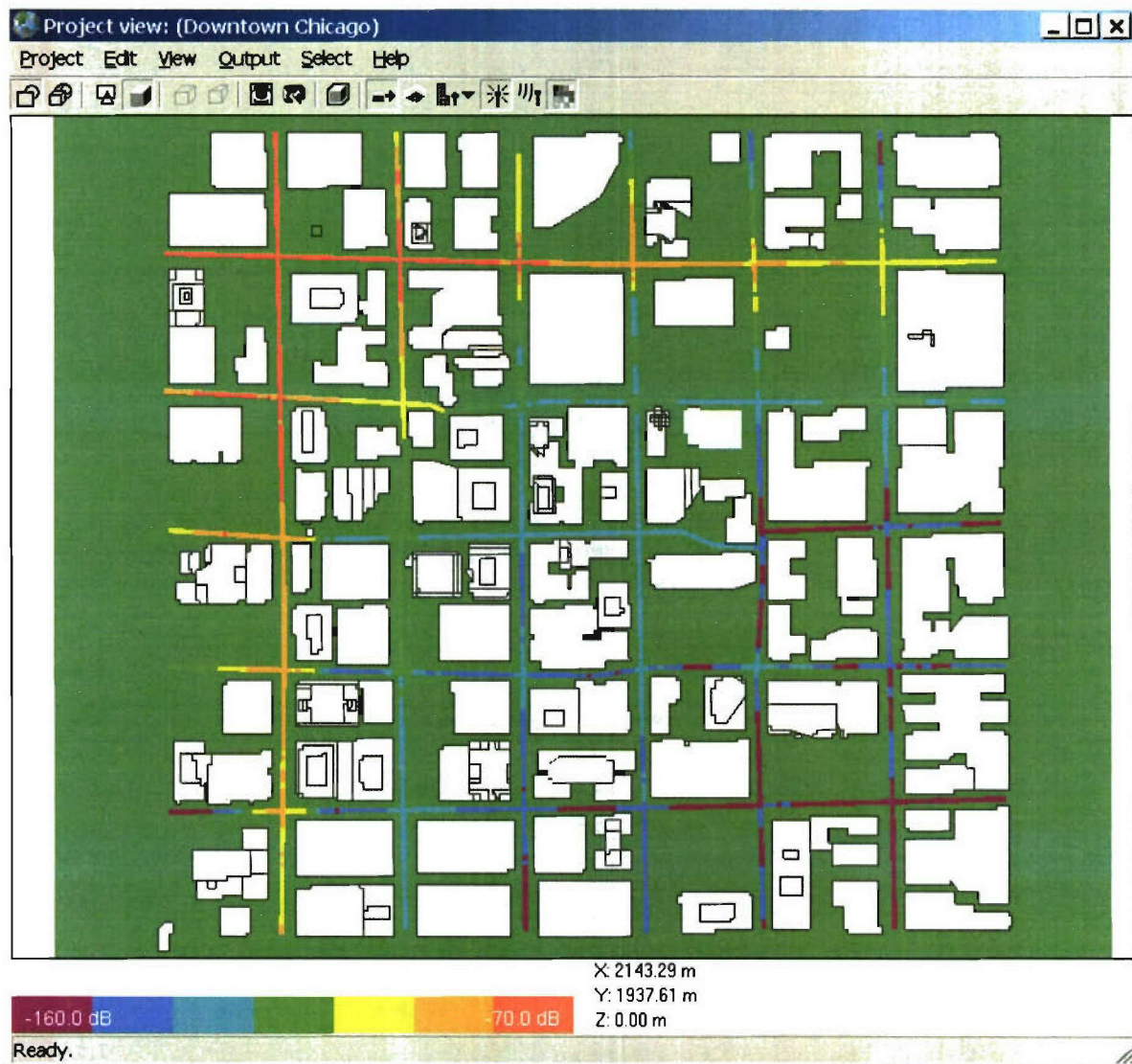


Figure 3: Path loss predictions along streets for Street Level Transmitter #1 at 600 MHz

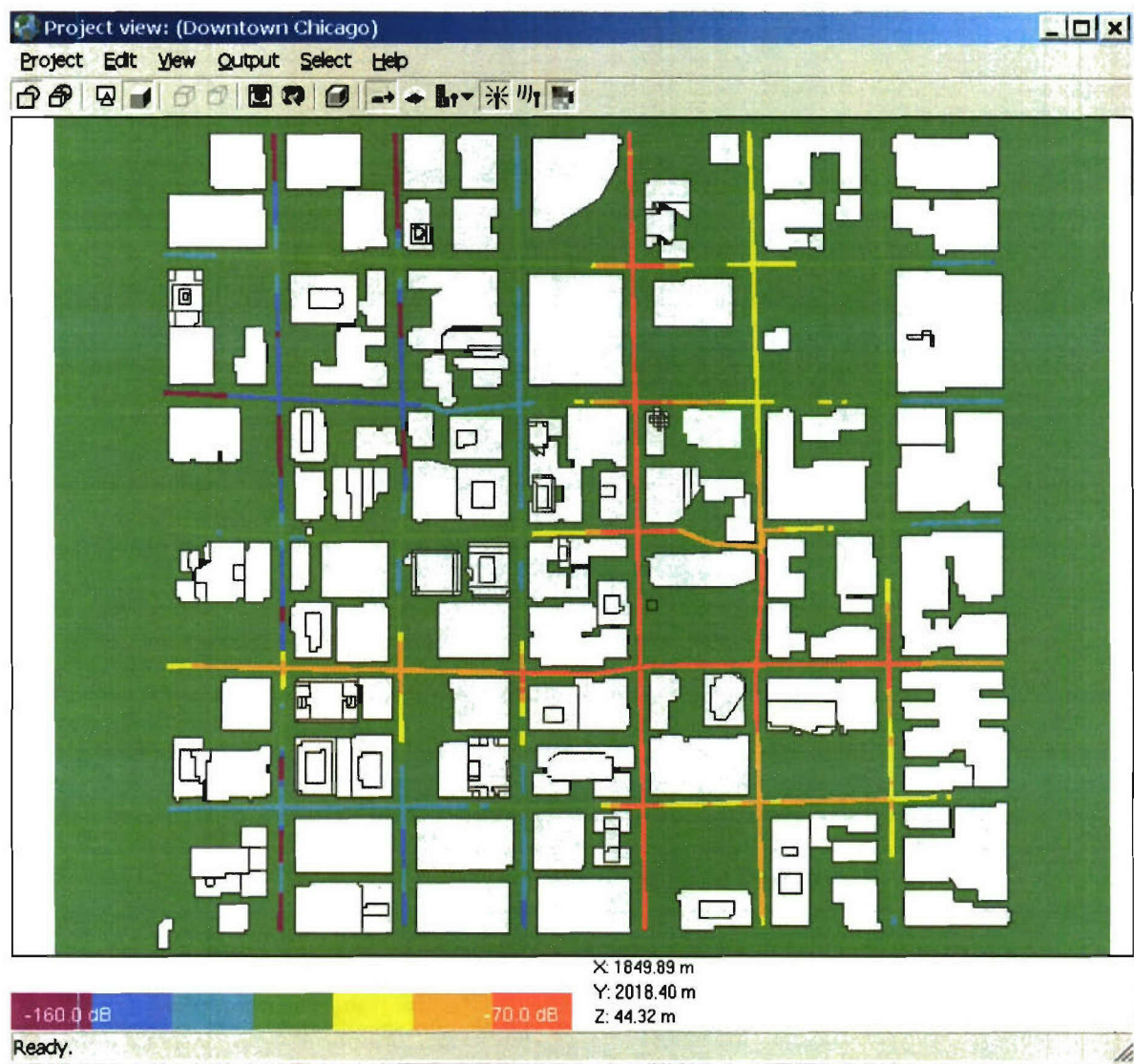


Figure 4: Path loss predictions along streets for Street Level Transmitter #2 at 600 MHz



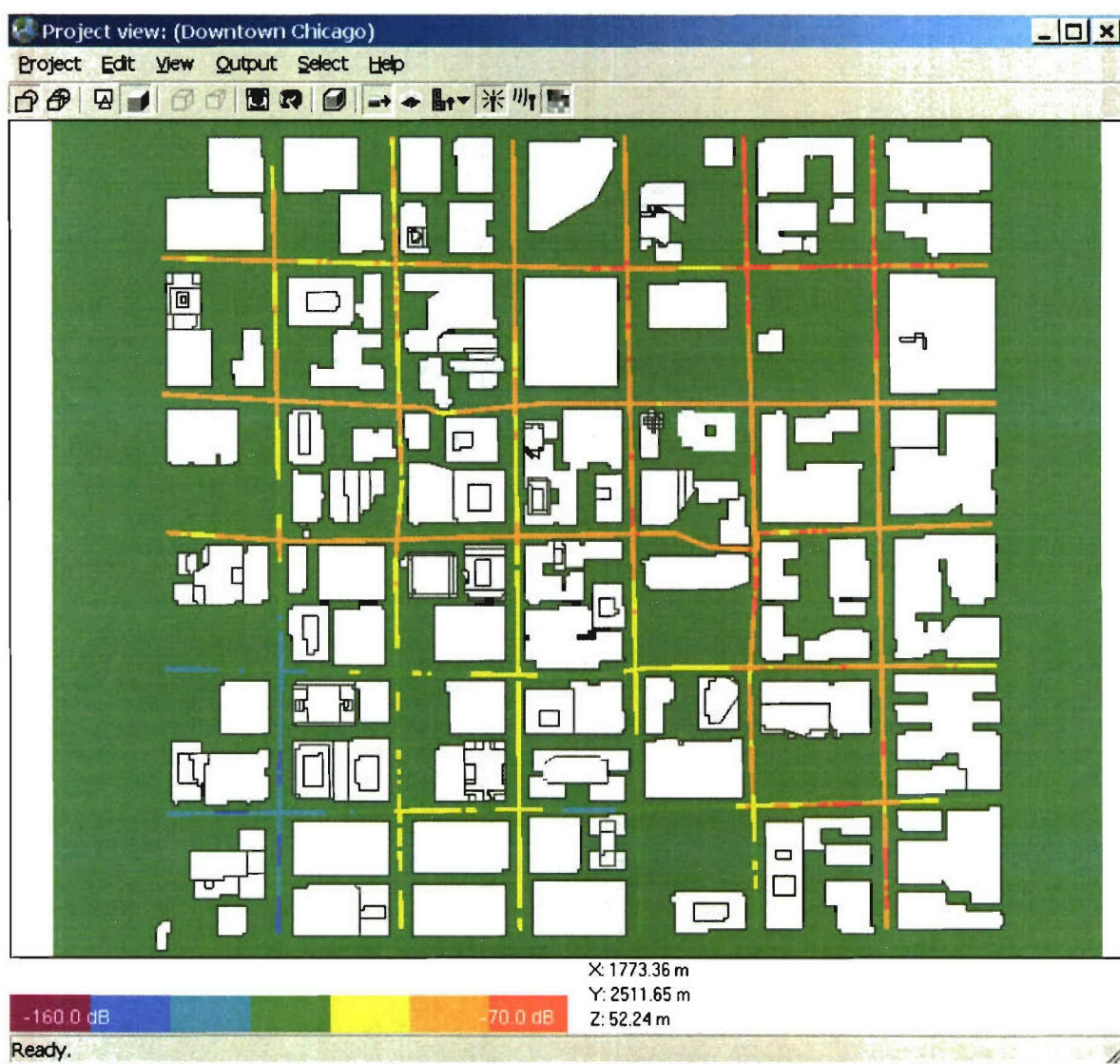


Figure 5: Path loss predictions along streets for Rooftop Transmitter #1 at 600 MHz



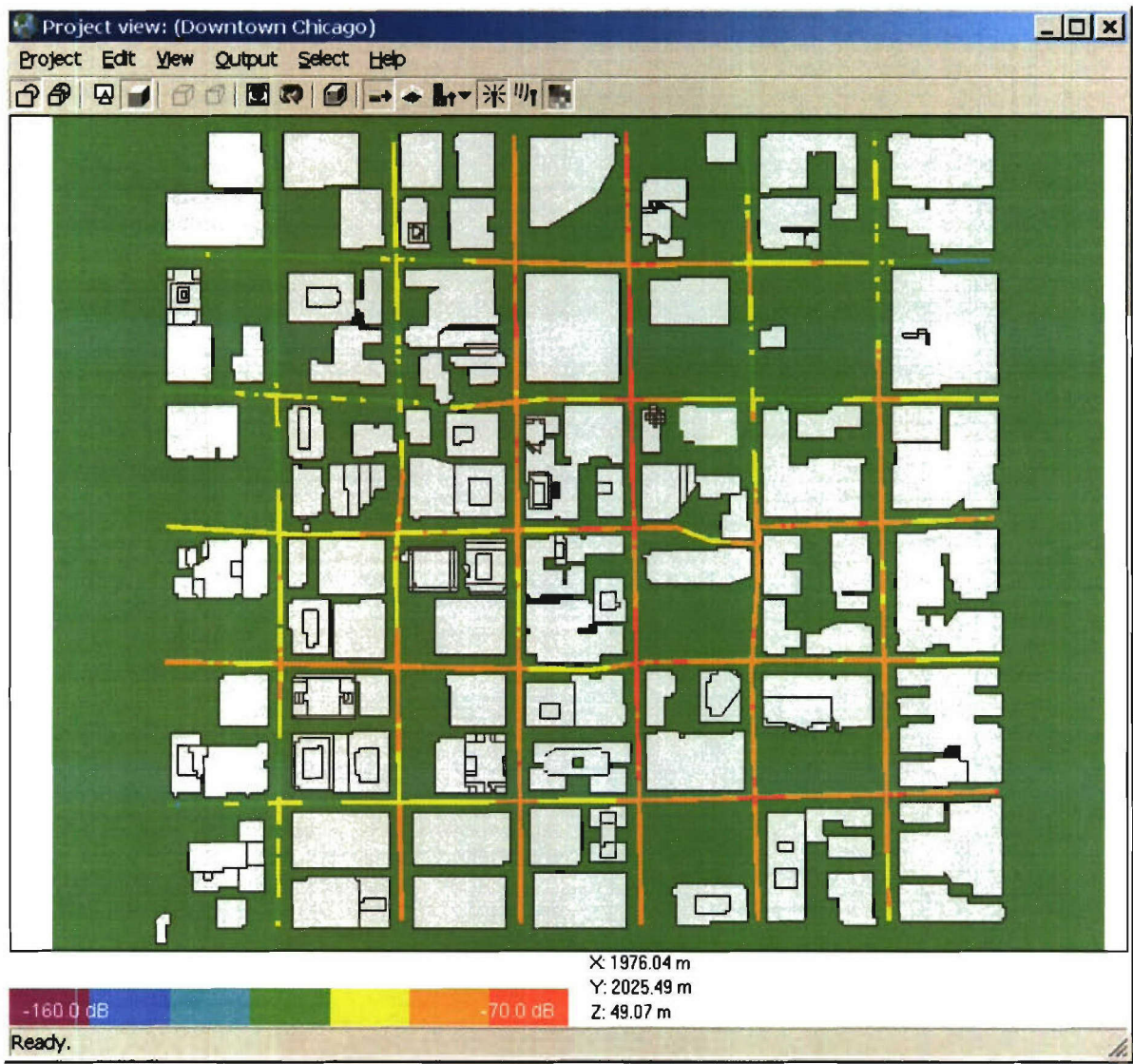
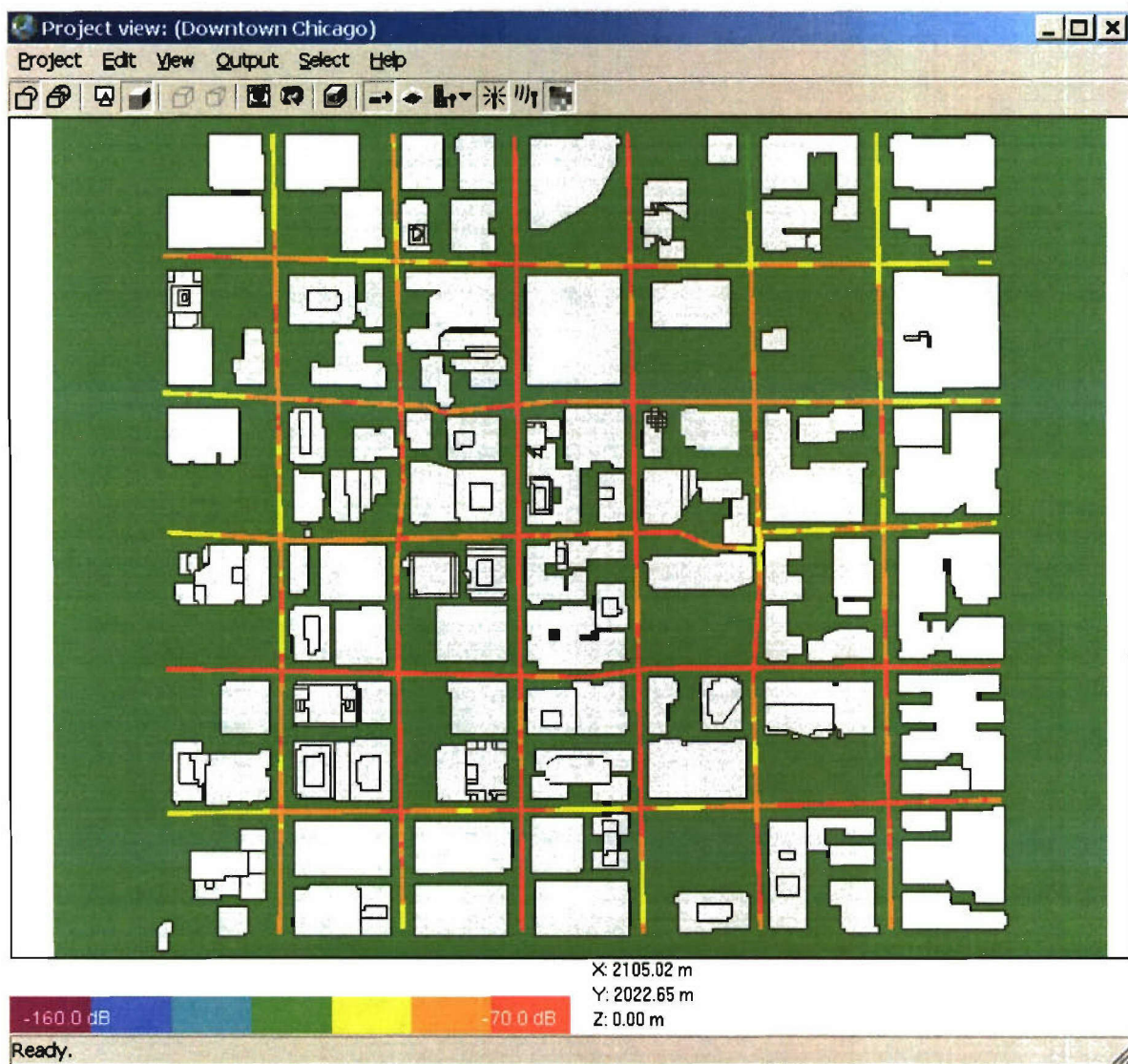


Figure 6: Path loss predictions along streets for Rooftop Transmitter #2 at 600 MHz



**Figure 7: Path loss predictions along streets for the High Tower Transmitter at 600 MHz**

The goal is to significantly reduce the computation time required by Wireless InSite's full three-dimensional (3D) propagation model. This will be accomplished by decreasing the run time of the SBR ray tracing procedure. Other goals include creating a calculation engine executable for a 32-bit Linux operating system, and to enable parallel processing on a Linux cluster.

#### 1.1.1.9.6. Timing Functions

During this month we began work on creating "timer" functions that can be inserted around any section of code. These functions are inserted permanently into the source code for accurately monitoring run time of different components. A summary of all run time data this is collected will be written to the diagnostics (.diag) file when the calculation finishes. When the calculation engine is run from the GUI, the run time diagnostics will also be written to the window which displays calculation progress (calculation log).



The C++ language was used to develop classes capable of timing sections of code and of reporting the collected timings in a unified format. An interface was developed between the C++ classes and the Fortran code used in the calculation engine. 103 important locations in the calculation engine were identified and a timer was placed in each location. InSite projects were built that use parts of the calculation engine that AFIWC will use. Those projects were run and the timing results were analyzed.

The analysis successfully identified the critical path of the computation and sections of the calculation engine important to the overall run time. Critical sections were closely examined. Small changes in those sections, most of which were in the ray-tracing portion of the engine, proved effective in reducing total run time. The extent of improvement varies by project. Some projects currently run 17-22% faster. A developer reports that one project runs in 25% of the original time, now running in 15 minutes compared to previously running in an hour. Projects with more diffractions appear to have more improvement. Note that some portion of the improvements come from using a new version of the Lahey Fortran compiler.

Summary timing data now is written to the calculation log window, visible in the graphical user interface whenever a calculation is running. Timings are shown with each percentage complete indicator written to the calculation log window. Detailed timing data is also written in the .diag file associated with each project.

The work on this task has been completed.

#### **1.1.1.10. Develop a Faster 3D SBR Ray-Tracing Algorithm**

Because of the similarities of the SBR approach used in WI to the ray tracing performed for computer graphics applications involving the rendering of complex scenes, there are a number of promising techniques available for decreasing the computation time. We have begun to adapt recent developments in computer graphics techniques to the ray tracing required by electromagnetics computations. The work on this task will continue into next month.

With the integration of C++ in the calculation engine described in section 1.1.1.9.6, the foundation has been laid for replacing the ray-tracing portion of the Fortran engine with Remcom's highly-optimized C++ Optimized Ray-Tracing Engine (ORE). A design for integrating ORE has been reviewed and approved by the InSite Project Leader.

The work on this task will continue into next month.

##### **1.1.1.10.1. Calculation Engine Executable for Linux Operating Systems**

The Linux port of the calculation engine is in progress. A set of regression tests has been put in place and results from 44 separate runs of the Linux version of the engine are regularly compared to results from the Windows version. The Linux test cases are run on Remcom's Linux cluster under PBS, with results brought back to the Windows computer for comparison in the regression tests.

The test cases include both optimized runs and debug runs. The debug runs use the full checking capabilities of the Lahey Fortran compiler to ensure, for example, that array indices remain in bounds and that inputs to intrinsic numeric functions are within the correct range.

The work on this task will continue into next month.

#### **1.1.1.10.2. Enhancements to Building Pre-Processor**

The building pre-processor is used to eliminate unnecessary detail from urban building data. During this month we have begun testing the new building pre-processing algorithms and interface. The work on this task will continue into next month.

The work on this task will continue into next month.

#### **1.1.1.10.3. Test Cases**

During this month we have modified the test cases which will be used in the future to demonstrate run time reduction. Test cases have been developed for the following scenarios:

- a. Dense urban area with street level transmitters and street level receivers
- b. Dense urban area with rooftop transmitters and street level receivers
- c. Dense urban area with airborne transmitters above rooftops and street level receivers.

The work on this task will continue into next month.

### **1.2. Immediate Plans**

Begin work on Wireless 2.3 capabilities.

### **1.3. Technical Problems**

N/A

#### **1.3.1. Technical Problems Encountered**

N/A

#### **1.3.2. Cost/Schedule Impact**

N/A

#### **1.3.3. Steps taken to Remedy Problems**

N/A

### **1.4. Resolutions to Previous Technical Problems**

N/A

### **1.5. Recommendations**

N/A

## 2. Cost Incurred and Outstanding Commitments

### 2.1. Current Costs Incurred

\$0.00

### 2.2. Cumulative Costs Incurred

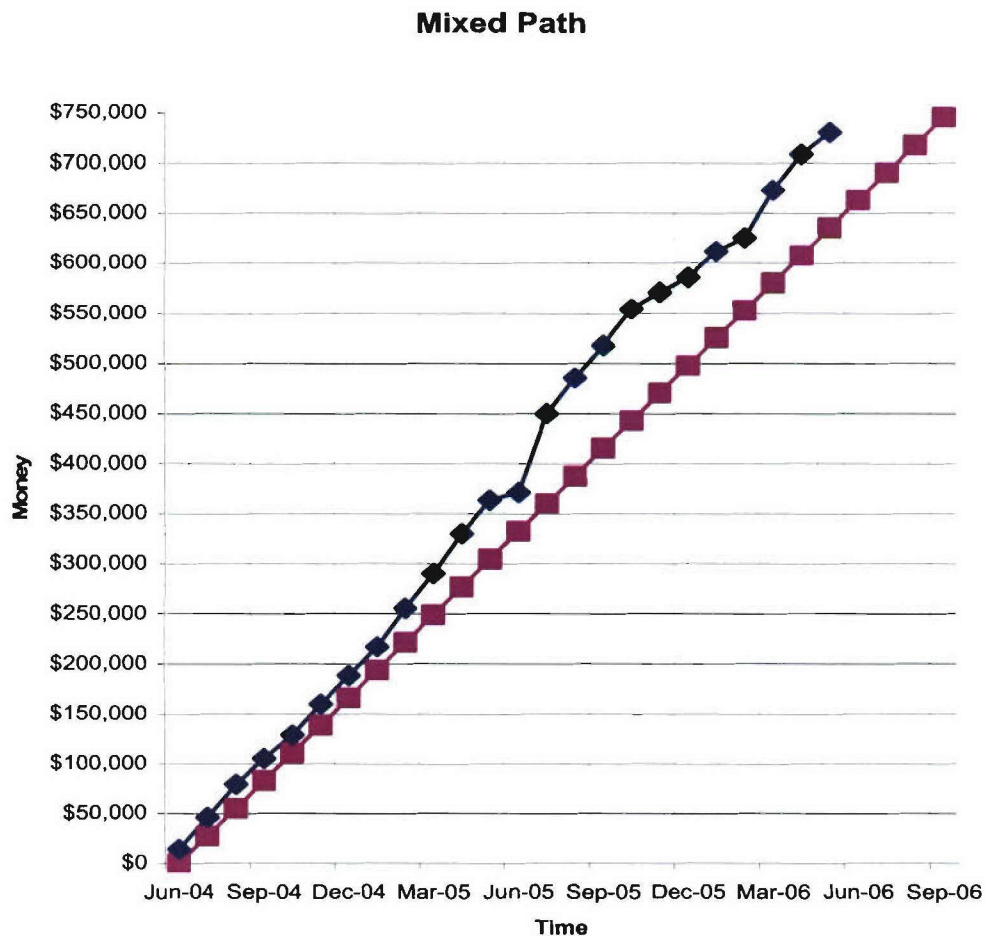
\$730,759.39

### 2.3. Funds Remaining

\$15,801

### 2.4. Spending Costs

The total available funding on this project is \$746,560. Based on this expectation, we have revised our spending plan as shown in the following chart.



### **3. Project Management Review (PMR)**

#### **3.1. Agendas**

N/A

#### **3.2. Presentation Materials**

N/A

#### **3.3. Minutes**

N/A

### **4. Appendices Technical Reports**

#### **4.1. Vertical Plane Urban Propagation Model**

The essential characteristics of the empirical models originally attributable to Bertoni and Ikegami are identified and incorporated as components of a more general model which provides alternate formulations of the established algorithms for multi-screen diffraction (MSD), roof-to-street attenuation and novel formulations for base station elevations below that of roof-top level. The applicability of the conventional elements is enhanced with supplementary methods appropriate for more general urban terrain not confined to collinear buildings of uniform spacing, thus permitting more general ray paths composed of isolated MSD diffraction configurations and conventional (optically independent) multiple knife edge diffracting elements.

##### **4.1.1. Modifications and Extensions of Conventional Methods of Vertical Plane Urban Propagation**

##### **4.1.1.1. Alternative Formulation of Multi-Screen Diffraction Loss for Base Stations of Arbitrary Elevation Relative to Neighboring Buildings**

The Walisch Ikegami model [6] is valid for urban terrain conforming to the assumptions of uniform spacing and of nearly collinear roof tops as in Figure 8. The model is unreliable for transmitter elevation approaching roof top level and performs poorly for base station heights below roof top level. Acknowledging these deficiencies, the proposed model provides an accurate and numerically tractable alternative formulation of multi-screen diffraction (MSD) based on the exact solutions of Boesma [1] and valid at arbitrary transmitter elevations relative to the line of screens used to approximate buildings in an urban terrain. The proposed alternate formulation of the MSD loss is expressed as a height dependent correction of the value for collinear transmitter and roof tops and is of the explicit form.



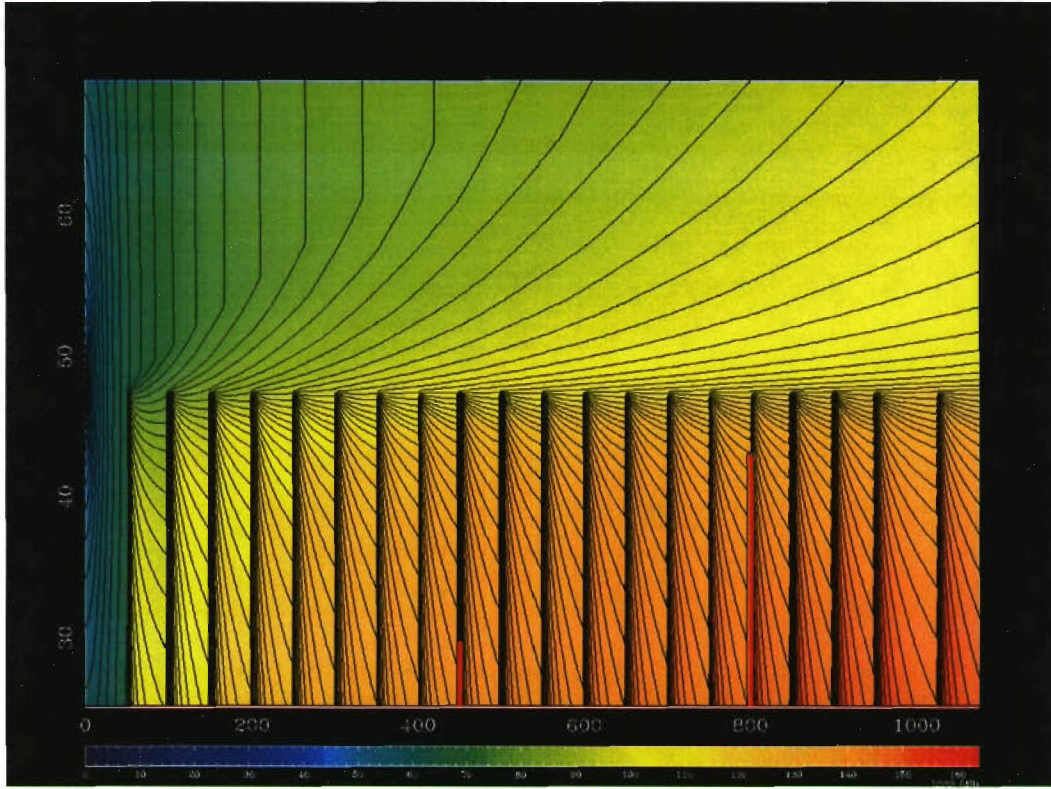


Figure 8

$$Q_c^M(g_c) = Q_c^M(0) + f_{<} [Q_c^M(g_{c<}) - Q_c^M(0)], (g_c < 0) \quad (1)$$

$$Q_c^M(g_c) = Q_c^M(0) + f_{>}^p [Q_c^M(g_{c>}) - Q_c^M(0)], (g_c > 0) \quad (2)$$

where

$$f_{>} = \frac{\log(1 + |g_c|)}{\log(1 + |g_{c>}|)} \quad (3)$$

$$f_{<} = \frac{\log(1 + |g_c|)}{\log(1 + |g_{c<}|)} \quad (4)$$

and where  $g_{c<} = g_{c>} = 2$  and where  $g_c$  is the (scaled) deviation ( $\Delta y$ ) of the transmitter height from roof top level,  $g_c = \Delta y / \sqrt{\lambda d}$ ,  $Q_c^M(0)$  is the exact loss ( $-20 \log_{10}(1/M)$ ) for incidence upon the edge of the Mth screen for a transmitter aligned exactly with the (M) roofs and  $Q_c^M(g_{c<})(Q_c^M(g_{c>}))$  is a numerical approximation of the exact value obtained using Boesma's formulation as evaluated for  $g_c = g_{c<}(g_{c>})$ . In addition, the parameter  $p$  appearing in Eq.(2) is computed according to the relation

$$p_+(g_c) = \frac{9 - 2g_c}{10}; (g_c < (1/2))$$

$$p_+(g_c) = 0.8; (g_c > (1/2))$$

The two bounding interpolation control quantities  $Q_c^M(g_{c>})$ , and  $Q_c^M(g_{c<})$ , which are the values of loss at two reference values of the scaled arguments  $g_{c>}$  and  $g_{c<}$ , are independently evaluated according to a similar approximate expressions.

$$Q_c^M(g_{c<}) = Q_c^M(g_{c<<}) + \left\{ \log \left( \frac{1 + |(M-2)|}{1 + |(100-2)|} \right) \right\} [Q_c^M(g_{c\infty}) - Q_c^M(g_{c<<})] \quad (5)$$

$$Q_c^M(g_{c>}) = Q_c^M(g_{c>>}) + \left\{ \log \left( \left[ \frac{1 + |(M-4)|}{1 + |(100-4)|} \right] \right)^q \right\} [Q_c^M(g_{c\infty}) - Q_c^M(g_{c>>})] \quad (6)$$

where  $q$  is an empirical parameter optimized as  $q = 1.7$ . Other optimized numerical parameters required in the approximation of Boesma's expressions include

$$Q_c^M(g_{c<<}) = 19.09091, Q_c^M(g_{c\infty}) = 60.5257, Q_c^M(g_{c>>}) = -0.74775, Q_c^M(g_{c>>}) = 22.52014 \quad (7)$$

Specific results for the approximate expression and the exact equivalent due to Boesma appear in Figure 9 in which the multi-screen diffraction loss  $Q_c^M(g_c)$  is plotted as a function of the scaled height displacement coordinate  $g_c$  for values of the number of screens (knife edges) in multiples of two between two and 100. It is noted that for the minimum number of screens considered,  $M=2$ , the physical interpretation of  $Q_2(g_c = 0)$  is the loss evaluated at the apex of the Mth (2nd) screen, an exact value of  $-20 \log_{10}(1/(M=2)) = 6.0206$  dB which is correctly suggestive of the well know result for a single (M-1) knife edge which is also plotted periodically with values shown as solid black circles. The exact confluence of multi-screen diffraction theory with known results for a single knife edge inspires the inclination to attempt a general diffraction scheme involving both formalisms. Direct comparison with the conventional Walfisch-Ikegami result is shown in Figure 9.1 where the loss at 900 MHz is plotted as a function of scaled base elevation (normal) deviation from building alignment. The exact result using the equations of Boesma are shown again as solid circles. The numerical simulation and conventional Walfisch-Ikegami are observed to agree well with the exact result for positive values of the argument but the conventional result diverges for base elevations below roof-top alignment. The linear behavior of the loss below roof top level apparent in the (COST 231) Walfisch-Ikegami model (with a slope of .8 dB/ meter) is characteristic of the model's MSD diffraction loss which is of the specific form.

$$L_{msd} = L_{bsh} + k_a + k_d \log_{10}(d) + k_f \log_{10}(v_c) - 9 \log_{10}(b) \quad (7A)$$

where for base station elevations above roof top level,  $k_a$  is given by

$$k_a = 54 - .8(\Delta h_b) \quad (7B)$$

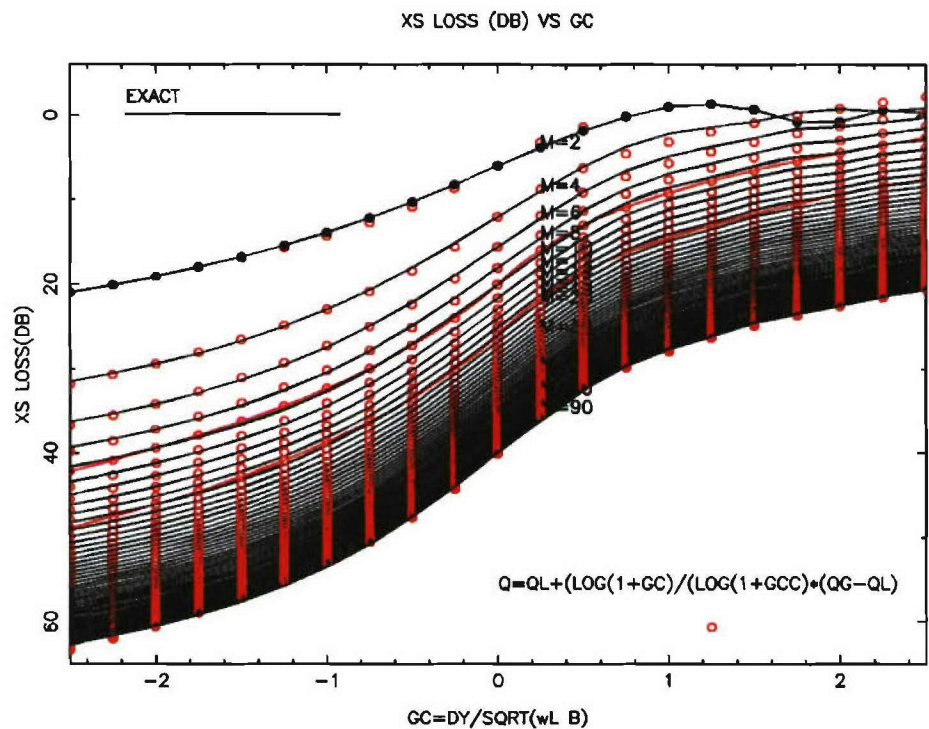


Figure 9

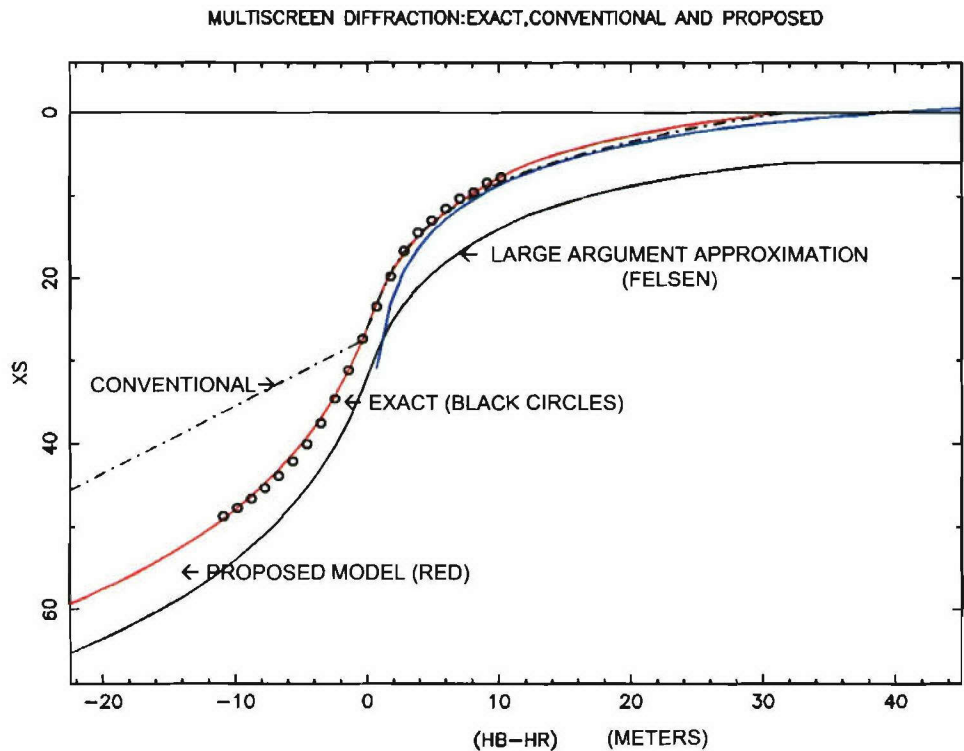


Figure 9.1



#### 4.1.1.2. Extension of Urban Vertical Plane Propagation to Non-Uniform Building Heights and Inter-Building Spacing

The proposed model also considers urban terrain profiles more complex than the simple two ray paths addressed by the Walfisch-Ikegami model. Whereas the Walfisch-Ikegami model is restricted to urban terrain consisting of at most two ray paths including an unobstructed ray associated with multi screen diffraction and a final ray associated with roof-to-street diffraction, the proposed model considers more general urban terrain as shown in Figure 10 which may include localized segments conforming to the Walsich-Ikegami assumptions, but may also include other portions which are not aligned with a segment of local uniformity. In the proposed model the partial attenuations attributable to such portions of the terrain are computed according to multiple (optically independent) knife edge diffraction. The idealized multi-screen diffraction (MSD) portions are indicated in Figure 10 with white arcs spanning the angle between effective source and receiver horizon. The independent knife edge diffraction centers are indicated by black arcs centered at the screen which subtend the angle between the localized source and its effective receiver horizon. The urban terrain of Rosslyn, Virginia rarely offers profiles in conformity with the idealized Walfishch-Ikegami assumptions and is exemplified by the terrain profile shown in Figure 11.

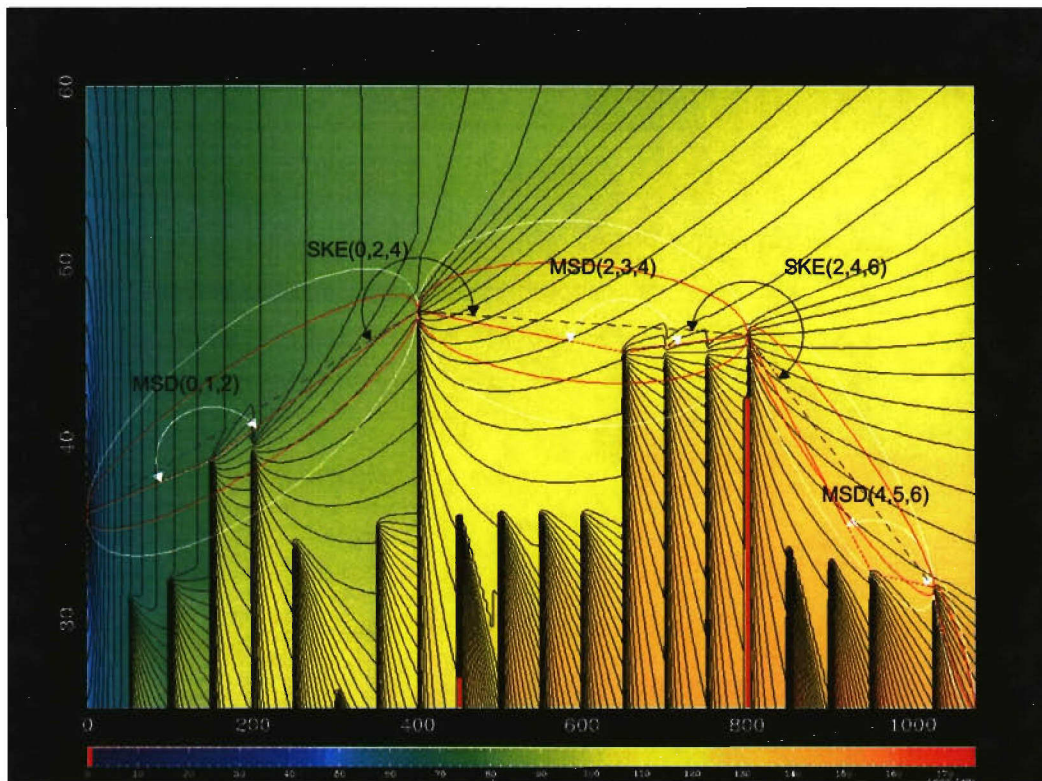


Figure 10

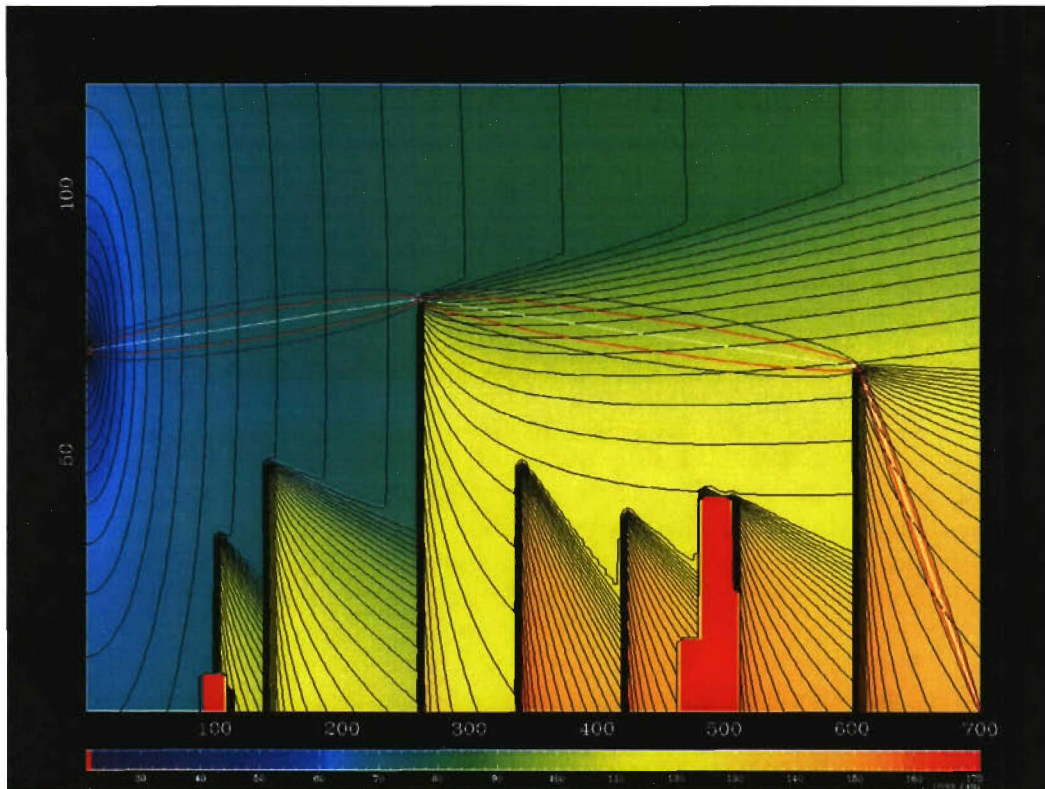


Figure 11

#### 4.1.1.3. Alternative Formulation of Roof-to-Street Diffraction with Recent Heuristic Modifications of UTD

A final perceived deficiency of the Walfisch-Ikegami model is its use of flawed diffraction coefficients from a dated formulation of the geometrical theory of diffraction which have since been corrected. In its modeling of roof-to street diffraction, the Walfisch-Ikegami model uses a diffraction coefficient for perfectly absorbing wedges and screens derived by Felsen [2] from geometrical optics and therefore incorrect for configurations approaching an incidence shadow boundary. The UTD diffraction coefficients of Kouyoumjian and Pathak [4] are properly behaved in the shadow boundary and admit to an exact solution for screen diffraction (exterior wedge angle  $= 2\pi$ ). In addition Holm has shown that his heuristic UTD modeling of wedge diffraction for imperfectly conducting materials reduces to a single partial diffraction coefficient in the perfectly absorbing limit obtained from the following expression for  $R_0 = R_n = 0$ ,

$$D = D_1 + R_0 D_2 + (R_0 R_n) D_3 + R_n D_4 \quad (8)$$

Such a formulation of roof-to-street diffraction, generalized to include reflection from the walls of adjacent buildings, is employed in the proposed model.



#### 4.1.2. Urban Terrain Geometrical and Other Considerations for Implementation of Proposed Methods

##### 4.1.2.1. Extraction of Terrain Profile

Provided with traditional data files for urban terrain, faces of constant elevation are first detected and interpreted as floor levels or rooftops of buildings. The surface dimensions of the vertices and their constant elevation are stored and a building identification index is assigned to the coordinates so stored for immediate retrieval. The information collected can be used to create an urban building footprint map as appears in Figure 12. Given a point of initiation on the urban terrain for the profile of interest and either a receiver location or intended orientation of the vertical plane relative to the origin, the intersection of the vertical plane with the buildings lying in its path may be computed to create an array of distances from the transmitter in the one dimensional range coordinate and the vertical elevation of the points of intersection along the profile at each intersection. The intersections in the footprint map appear in the Figure 12 as solid (black) circles and the corresponding urban profile in the resulting vertical plane is shown in Figure 13. For the purposes of examining an urban terrain profile exhibiting a more general composition including localized structures consistent with multi-screen diffraction as well as optically isolated knife edges, the urban terrain profile shown in Figure 14 will be considered in the discussion which follows.

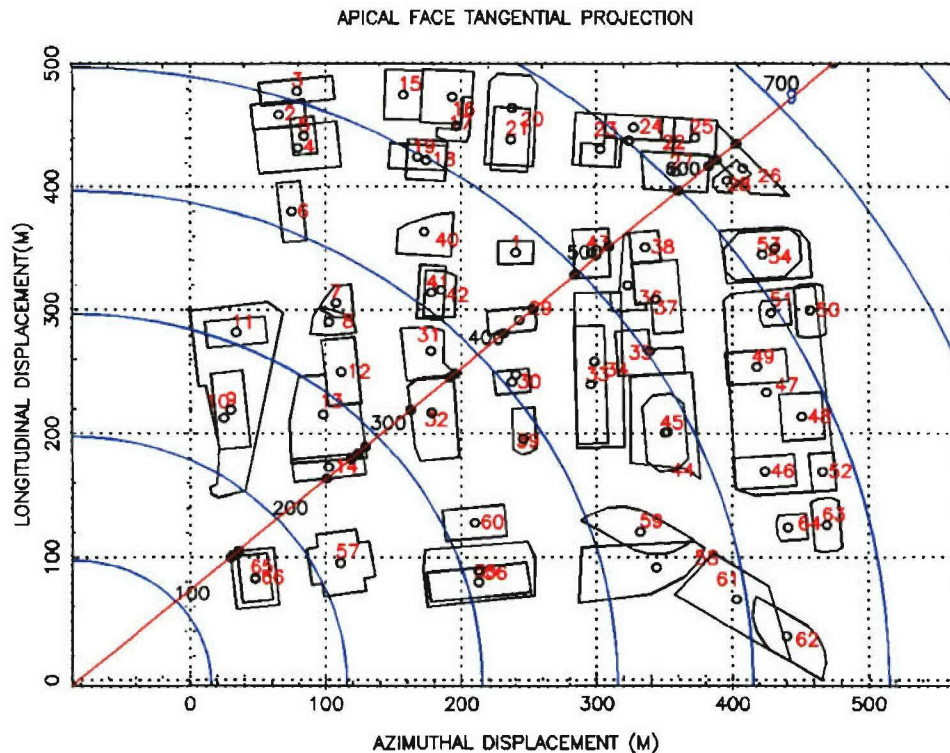


Figure 12



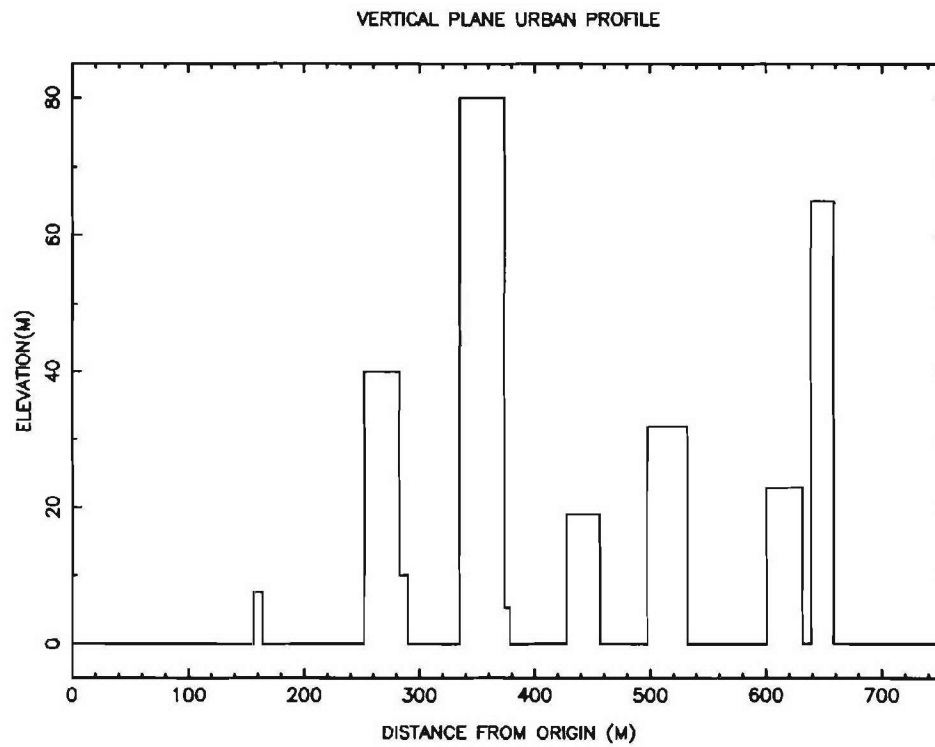


Figure 13

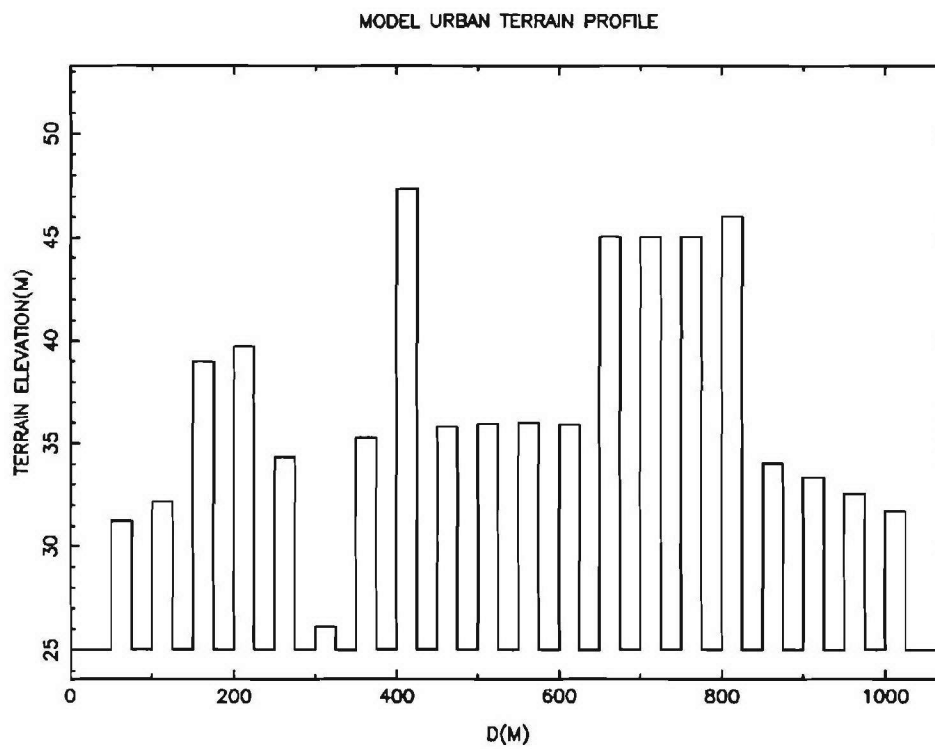


Figure 14

#### 4.1.2.2. Formalism for Geometrical Definition and Detection of Buildings

Since as suggested by Bertoni [7] [8], buildings are to be approximated by single diffracting screens, it becomes necessary to establish a formalism for geometrically defining a building. Aware of the definition of a diffraction centers as any local convexity introduced by physical structures to incident ray paths, the definition of a building adopted for this study is any region of monotonic local curvature in which the inclination of ray paths is reduced by each successive component vertex. The building identification sequence resulting from this definition for the urban terrain shown in the Figure 14 as red numerals corresponding to building count assignments. A corresponding sequence of index arrays are created for identifying the terrain index associated with a particular building assignment and an inverse array for recovering a possible building assignment associated with a given terrain index. The accumulation of the building identification sequence permits the construction of individual building parameter arrays which contain the coordinates (range and heights) of the vertices understood to comprise a given building. This information is vital to establishing building statistical parameters such as average width and periodic spacing, pending identification of the relevant multi-screen diffraction configurations. Anticipating the recommended constraint that each building provide but a single absorbing screen in the effective urban diffraction model, the urban terrain profile is next reduced to a sequence of half screens of negligible thickness, resulting in the essential urban profile shown in Figure 15.

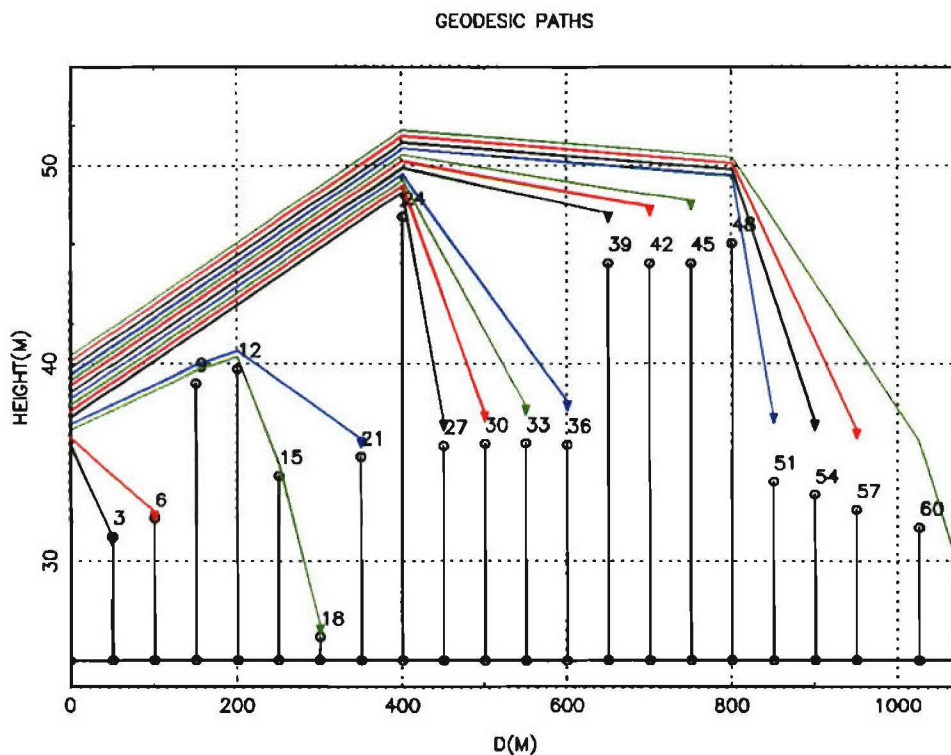


Figure 15

#### **4.1.2.3. Extraction of Indexed Geodesic Path to all Points in Terrain Profile**

The generalized Fermat Principle for diffraction states that a diffracted ray path will proceed from the transmitter to the receiver along the shortest possible (geodesic) path. In anticipation of the most general preference to evaluate path losses at an arbitrary intermediate range of the profile and at an arbitrary height, and in view of Fermat's principle for diffraction, it becomes of interest to systematize a description of the points encountered in a geodesic excursion from a fixed transmitter (understood to occupy a specified elevation at the beginning of the profile) to any intermediate point in the profile. An intermediate profile locus is understood to occupy a nominal indexed vertex of the profile or is defined as a linear interpolation between any two such vertices. Appealing to the definition of geodesic paths in a plane as defining a sequence of line segments proceeding through a sequence of monotonically decreasing slopes, an algorithm was written which identifies all such paths, and records the path index to all points in the profile and all constituent points encountered in a given path. A schematic presentation of the various paths to all points in the reduced profile is shown in Figure 15.

#### **4.1.2.4. Accumulation of Geodesic Paths and Horizon Arrays for all Points in Path**

Provided with the indexed paths and path contents to an arbitrary intermediate terrain location for which the path loss is desired, it becomes necessary to examine the properties of the associated path and to identify and record diffraction centers encountered along the path with proper regard to classification as either a component of a multi screen diffraction construct or as an element of an optically independent knife edge sequence. Since the path to a given point is geodesic and the geodesic paths are as depicted in Figure 15, the intermediate points of the path to a specified point each define a center of diffraction along the path to the static receiver. As an example the path to the final point of the profile is shown in Figure 16 where the geodesic path is drawn in red with the intermediate diffraction centers indicated by partial arcs centered at each diffraction center and spanning the angle between the corresponding effective transmitter and receiver.

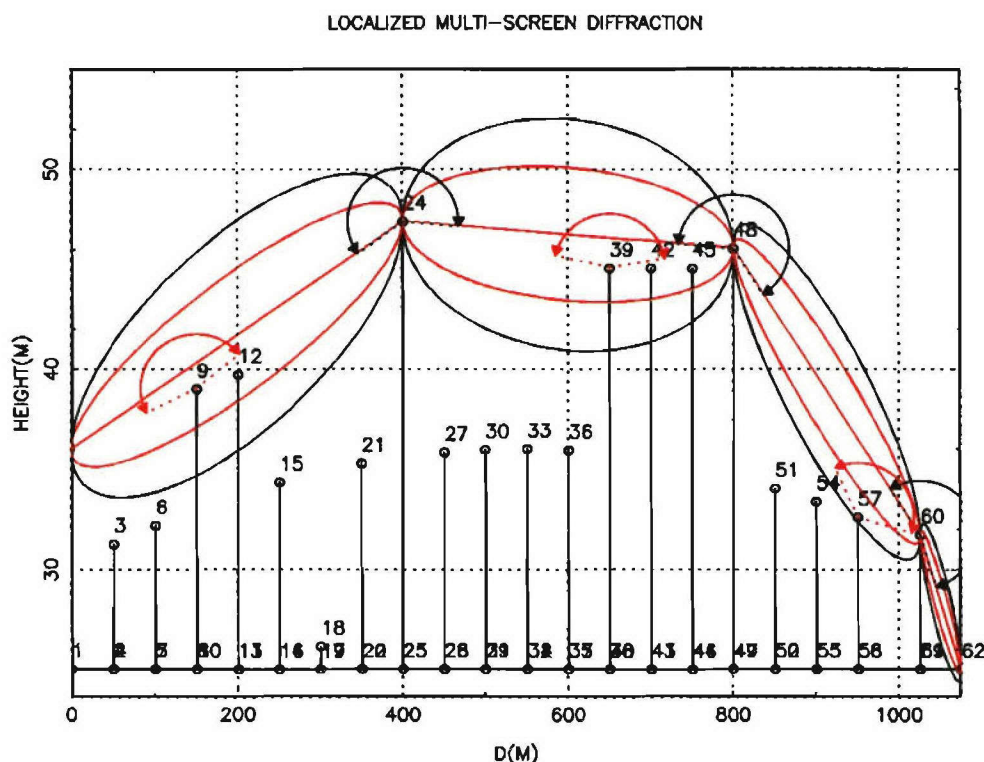


Figure 16

#### 4.1.2.5. Identifications of MSD Diffraction Centers

The optical environment of each ray of the geodesic path is next inspected to determine whether any intervening (sub-geodesic) structures penetrate the first Fresnel zone between the endpoints of the geodesic ray considered. Such sub-geodesic intrusions are readily apparent in Figure 16 as knife edges penetrating the relevant first Fresnel zones which are drawn for each segment of the geodesic path. Thus the first Fresnel zone between points (0) and (24) in the figure is penetrated by profile points (9) and (12). The sub-geodesic points of intrusions and the final profile point of the segment are interpreted as defining a multi-screen diffraction configuration in which the corresponding building dimensions are used to define the average spacing and building width as required to compute the relevant MSD contribution to the excess path loss. Designating the final point of the path as a center of rotation, the average orientation of roof tops is defined as the average angle from this appointed origin to each of the optically relevant buildings. The multi-screen diffraction loss is also a function of the normal coordinate above the average roof top alignment, the number of knife edges found to penetrate the first Fresnel zone and their average spacing. The MSD constructs are identified by three terrain indices which are the effective transmitter (first point of a geodesic ray), the first knife edge found to be of optical relevance and the endpoint of the geodesic ray. Three such MSD diffraction centers were identified in the example urban terrain and are shown in Figure 16 as red arcs centered on the second of these identifying terrain features and spanning the angle between the relevant ray path endpoints.



#### 4.1.2.6. Consolidation of Previously Independent MSD Constructs

Whereas the methodology described above activates sub-geodesic intrusions between principle vertices of a given geodesic path, an auxiliary procedure involves inspection of adjacent geodesic vertices for sufficient optical alignment to justify incorporation of adjacent elements into a single multi screen diffraction center. The common vertex of two adjacent but independent diffraction centers is then redefined as a diffracting element of a single multi-screen configuration composed of these originally independent elements. Thus the first two optical diffraction constructs shown in the top panel of Figure 17, initially modeled as (1) a single knife edge involving the transmitter and first two diffraction screens followed by (2) a 19 screen multi-screen diffraction configuration, are consolidated to create the single MSD shown in the second panel of Figure 17.

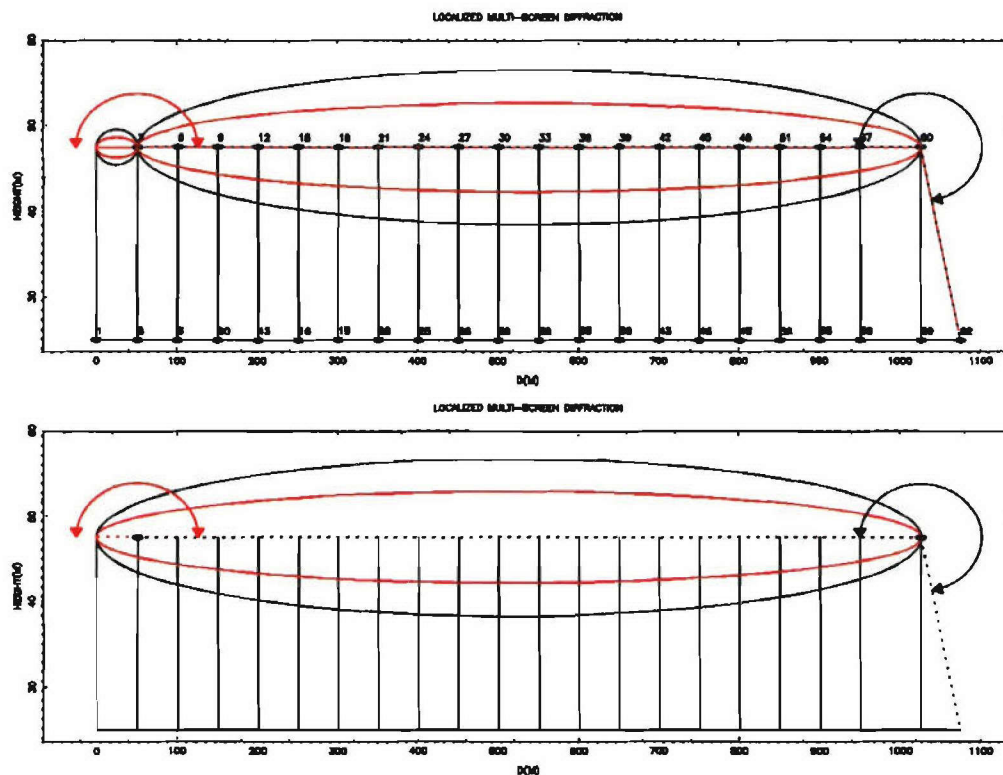


Figure 17

#### 4.1.3. Loss Evaluation Process

##### 4.1.3.1. Evaluation of Path Loss at Arbitrary Range, and H1 and H2

Whereas the earlier characterization of the geodesic path considered the terminal range of the urban terrain, the quantitative inclusion of comparable data for reconstructing the geodesic path to an intermediate range receiver makes possible the evaluation of excess path loss at any such point. Since the principle diffraction centers are the vertices of geodesic paths between antennas, provision of the geodesic path provides geometrical information essential to the calculation of path losses involving diffractive mechanisms.



To illustrate the mechanism, an elevated receiver at an intermediate range, as labeled in Figure 18, is analyzed by first recalling the (receiver) horizon of its most immediate terrain profile relation in the direction of the transmitter. If the slope from the most immediate horizon exceeds that of the geodesic approach to the horizon from the transmitter, the geodesic path to the horizon is examined in reverse order to establish the horizon of the specified field point. Since the geodesic paths to all points in the profile are known, identification of the receiver horizon among the profile points equivalently identifies the geodesic path to the specified (ground level) field point.

In the absence of back-scattering the geodesic path to ground level provides a full description of the optical environment of a receiver of any height above ground level and in general is required to enforce continuity of excess loss as a function of elevation at the specified range. Provision of the geodesic path to the specified receiver permits itemization of the relevant diffraction centers which are examined for prior classification as MSD or independent knife edge diffraction centers. If an intermediate diffraction center is identified as the central vertex of a multi-screen diffraction construct, the (multiple) knife edge count must be altered appropriately from the initial values established on the occasion of its initial detection. Thus the knife edge multiplicity count of the MSD considered MSD (2,3,4) in Figure 18 must be altered from its original value of four to the two intervening knife edges between the central vertex at 650 meters and the specified receiver. Alteration of the geodesic vertex assignments for the intermediate receiver may also alter the third vertex assignment of pre-existing single knife edges as required to compute altered maximum attenuation bounds appropriate for intermediate shadows. The final itemization of modified diffraction centers appropriate for calculation of the excess loss at the (elevated) intermediate field point shown in Figure 18 includes the first MSD diffraction center MSD(0,1,2), a single knife edge centered at point (2) and redirected to the intermediate receiver horizon and a second multi-screen diffraction center MSD(2,3,RXH) reconfigured for termination at the modified receiver horizon with a reduced constituent knife edge count of two.

Before detailing the numerical accumulation of the various partial excess losses, it is appropriate to recall the approximations of multiple knife edge diffraction originally due to Epstein and Peterson [9] which approximates the total multi-screen diffraction loss as a sum of single knife edge attenuation subject to an upper bound imposed by any subsequent diffraction screens. A typical urban terrain profile, after reduction to its component screens and consisting only of optically independent knife edges, is shown in Figure 19 with schematic arcs indicating the angular extent of each knife edge. At relatively remote elevations, the second knife edge introduces a negligible attenuation as suggested by the black vertical line segment in the figure. The cascaded implementation of successive knife edges requires that each component be deactivated at a specific maximum attenuation as the receiver approaches an elevation where the succeeding knife edge begins to exert an attenuation. This critical configuration corresponds to the elevation at which the succeeding knife edge first penetrates the first Fresnel zone between its effective source and the variable receiver height. Thus the attenuation of a given knife edge is set equal to a constant at the critical elevation corresponding to the onset of attenuation of its geodesic successor. Considering the succession between first and second knife edges in the Figure 19, the locus of points beyond the second knife edge associated with critical penetration of the relevant Fresnel zone (between the first knife edge and variable receiver) is shown as a blue dashed curve extending from the second knife edge.

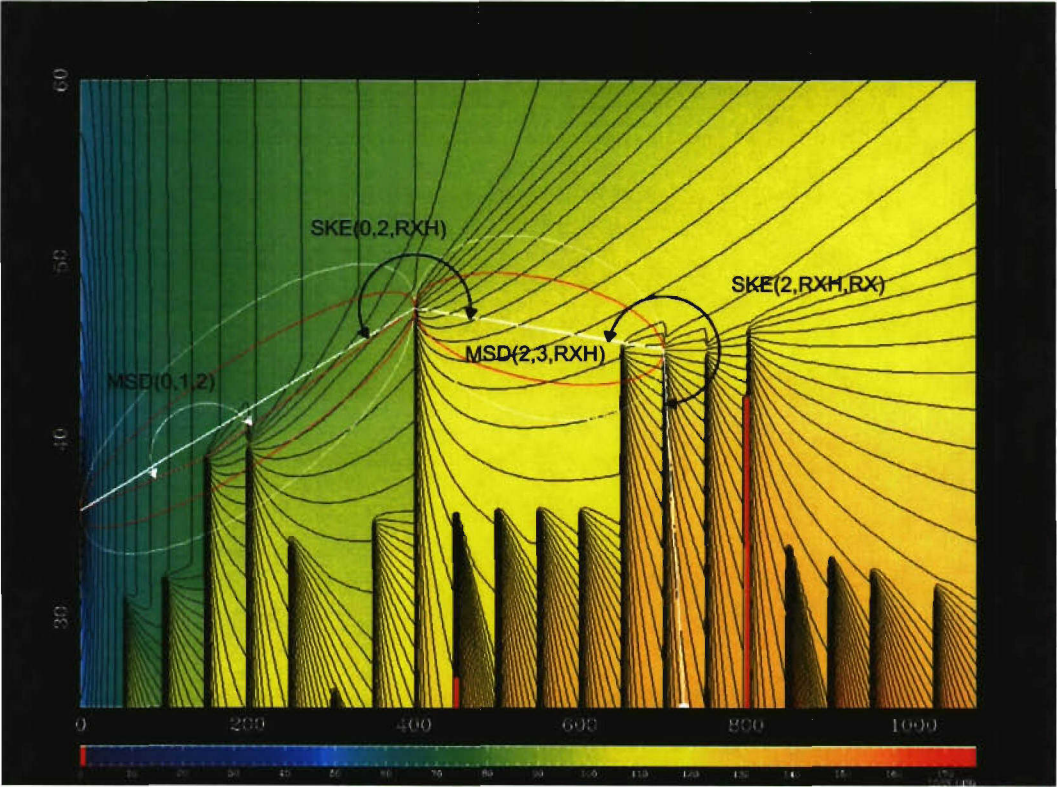


Figure 18

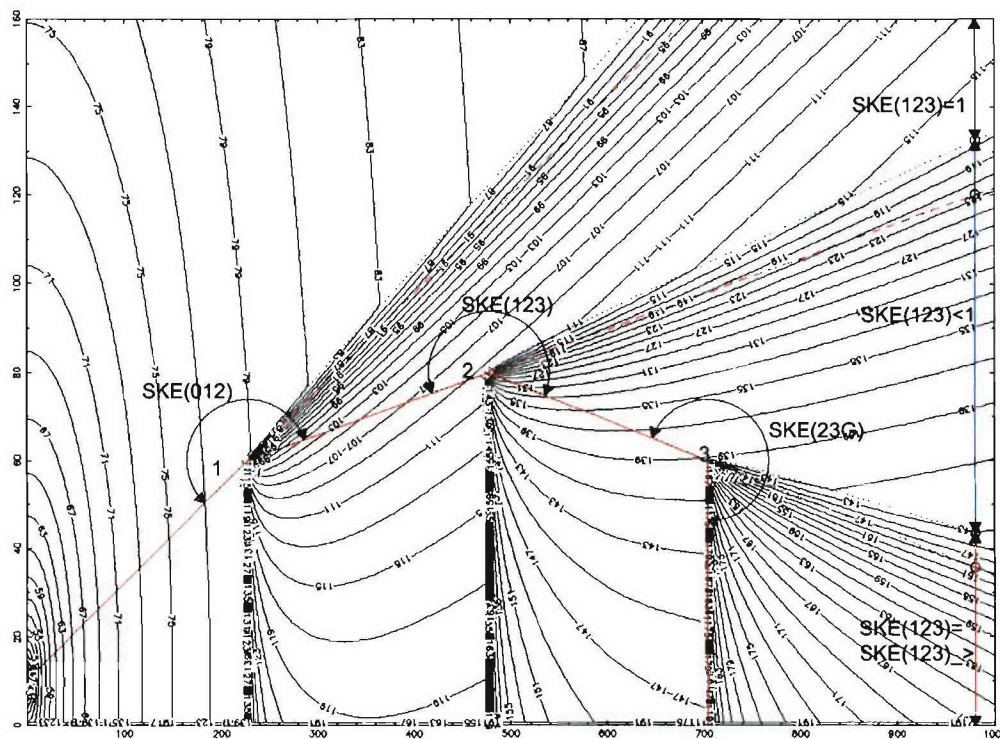


Figure 19

#### 4.1.3.2. Final Accumulation of Excess Loss

Returning to the final accumulation of excess loss appropriate for the receiver located at the intermediate range of Figure 19, the succession of independent excess losses due to each diffraction center is made apparent by considering an excursion in elevation initiated well above the line of sight beyond any diffractive influences. As the receiver elevation approaches the greater threshold of the first multi-screen diffraction center, a component of loss due to the MSD is introduced which increases to the maximum value obtained at the roof top level of the final knife edge of the MSD construct. The excess loss continues to increase as the second diffraction center, SKE (0,2,RXH) introduces a diffractive loss between its initiation threshold and that of the final knife edge centered at the receiver horizon. In the final segment of the excursion and descent to ground level, the diffractive influence of the final diffraction center SKE (2, RXH, RX) is added to the excess loss resulting in a total excess loss at the receiver of 52.3 dB. The various components of the total excess loss and their sum have been plotted as a function of the structural receiver antenna height in Figure 20.



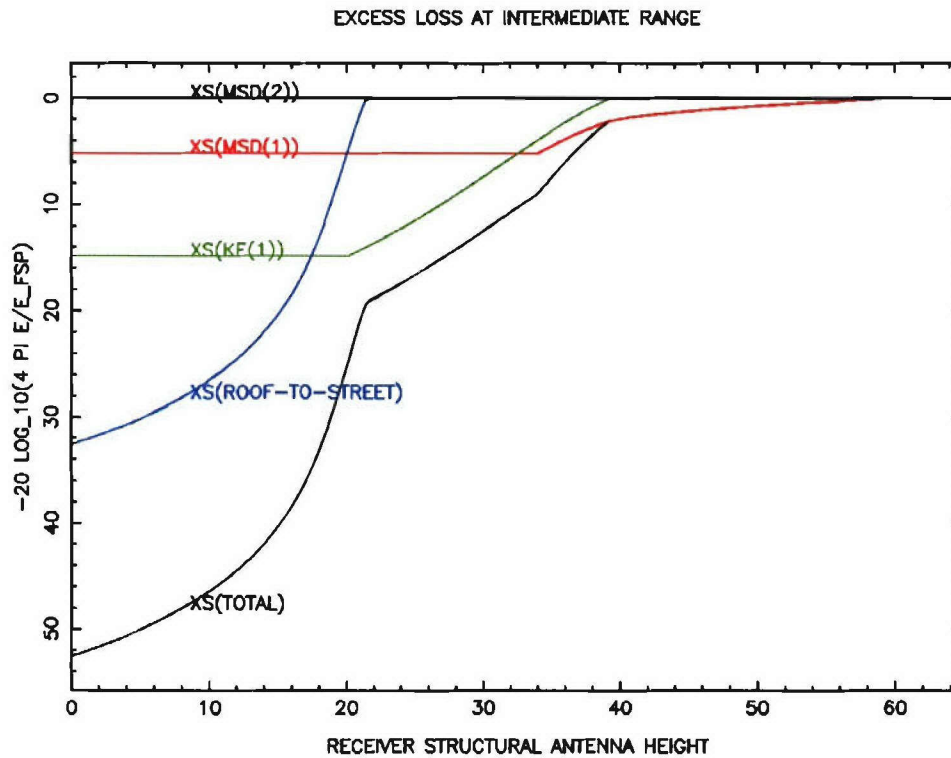
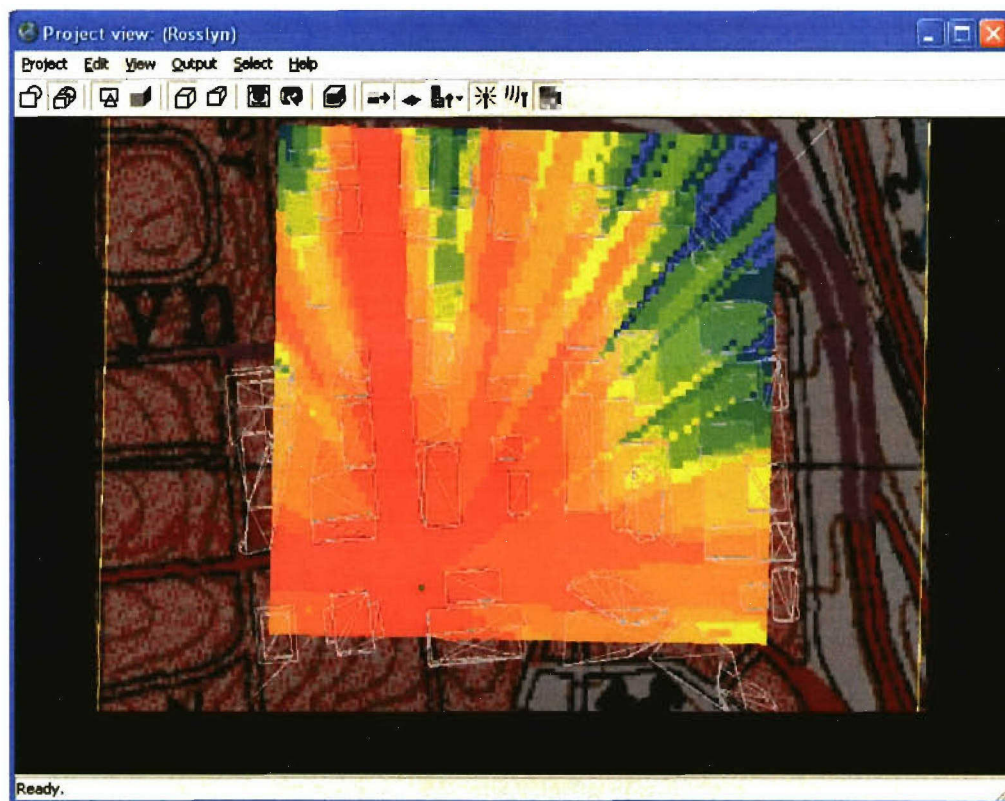


Figure 20

## 4.2. Fast Urban Predictions

### 4.2.1. Initial Effort

For the initial effort, it was deemed prudent to follow the methods used by MITRE in [10]. This effort proved to be a starting point for a fast urban path loss estimator. The optimized ray engine (ORE) was used in conjunction with a building counting algorithm and a path loss attenuation formula. This algorithm computes path loss based on the amount of free space path loss combined with path loss due to urban settings. Computing reflections, transmissions and diffractions aren't necessary because the building depth accounts for their contribution. The first implementation step used ORE to count the number of facets between the transmitting and receiving antennas.



**Figure 21: Colors showing number of walls passed through**

From there, a simple algorithm calculated the number of buildings between the transmitting and receiving antenna.



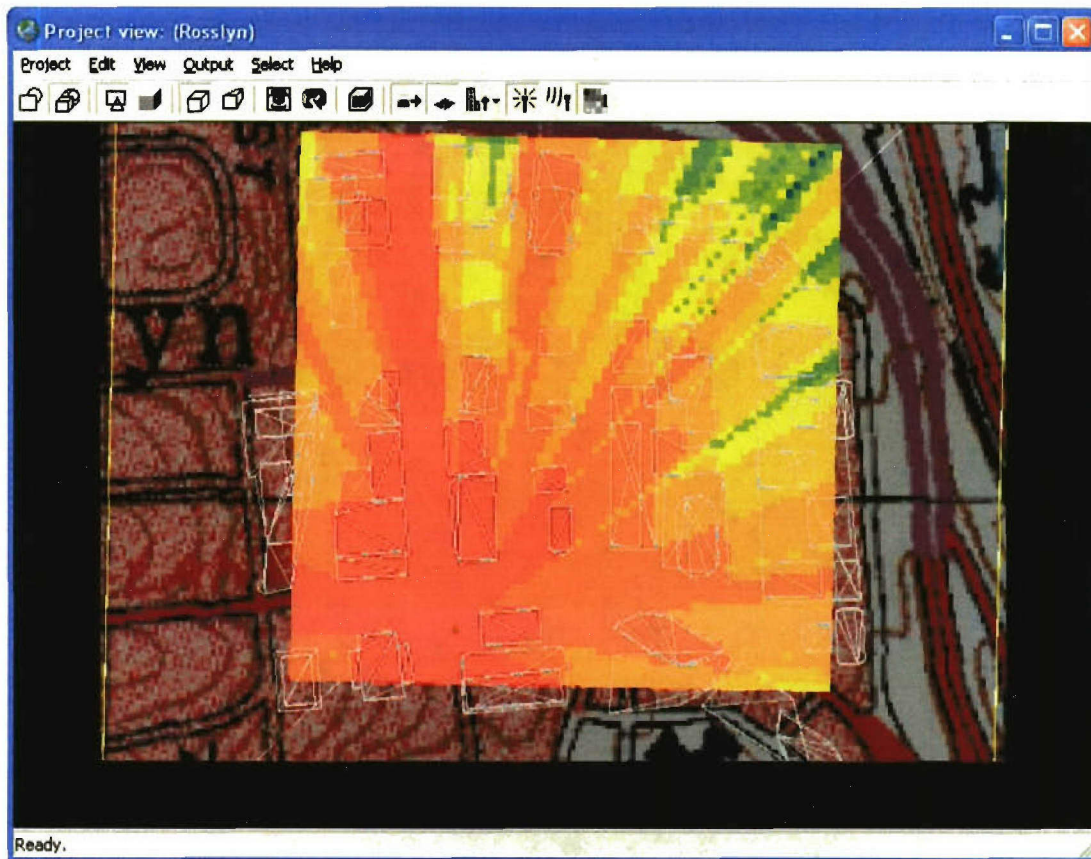


**Figure 22: Colors showing number of buildings passed through**

Now, knowing the building depth and the free space depth formulas from the [10] could be used to calculate path loss attenuation. Further work included automatic tuning of the model based on building material parameters and frequency as well as adding additional propagation mechanisms.

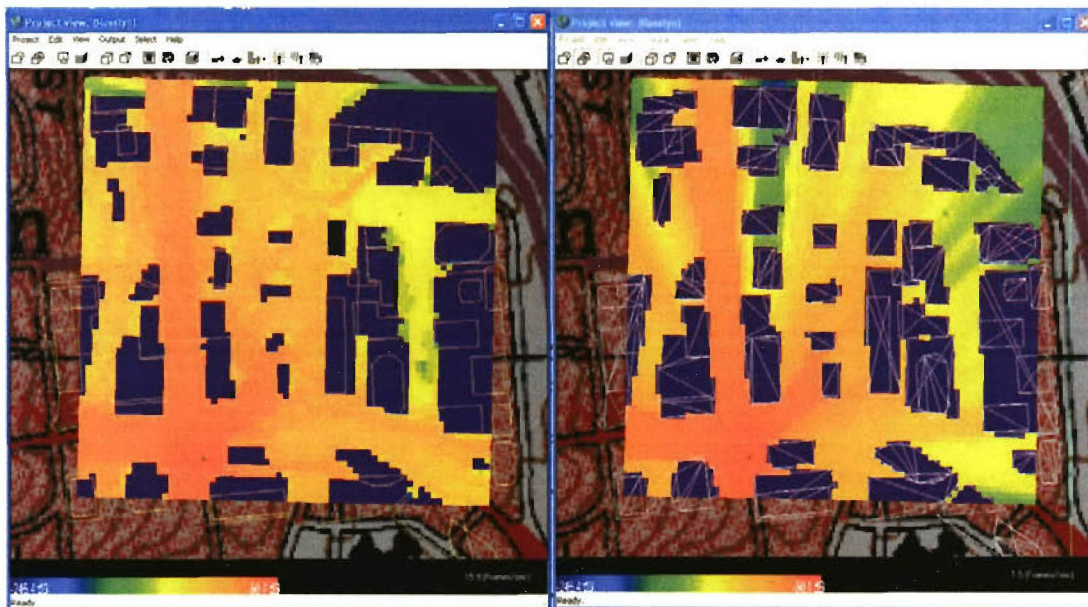


Figure 23: Left Wireless InSite Urban Canyon 2D, Right new model

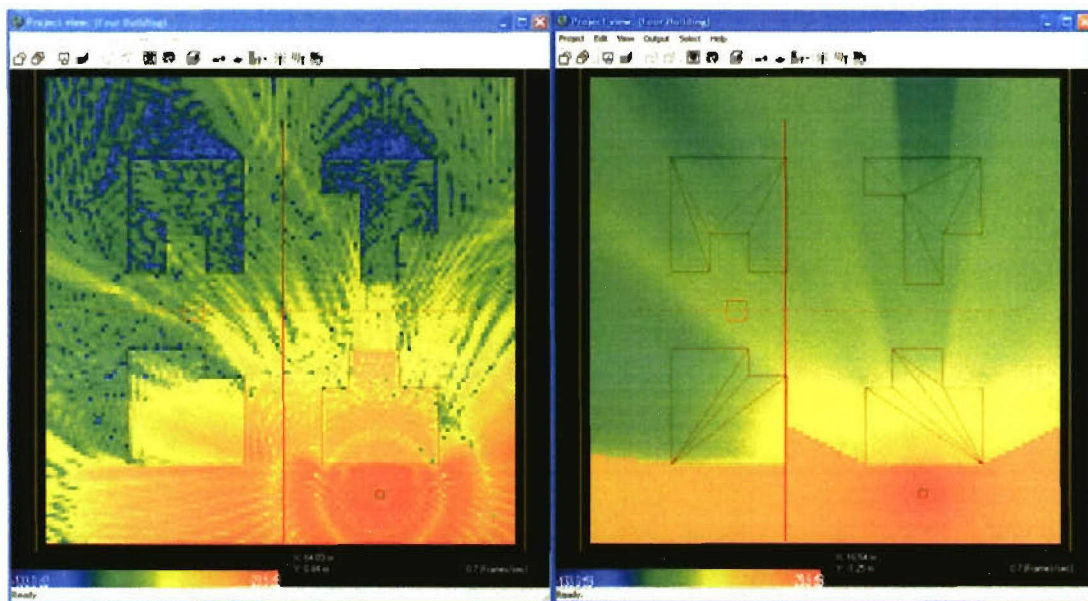


Figure 24: Left Urban Canyon FDTD, Right new model

Further Remcom compared the results of this model with both measured data and Wireless InSite predictions. These are shown in Figure 25, Figure 26, Figure 27 and Figure 28.



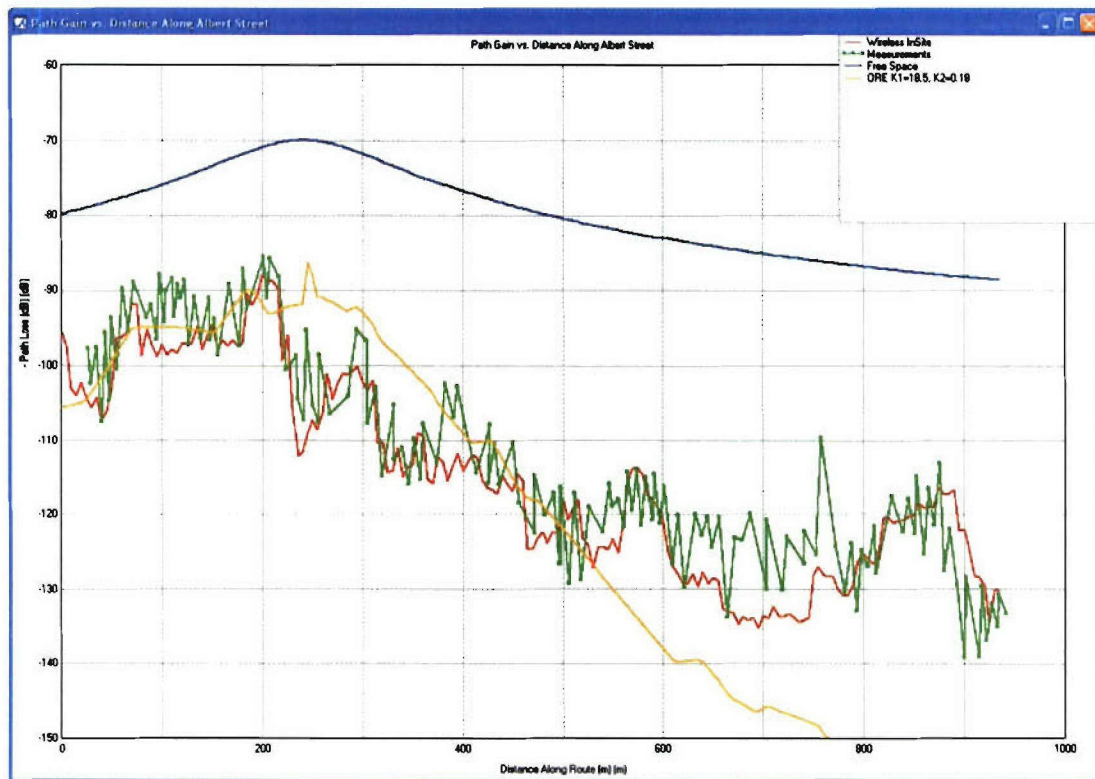


Figure 25: Comparisons of Path Gain on Albert Street, Ottawa Canada

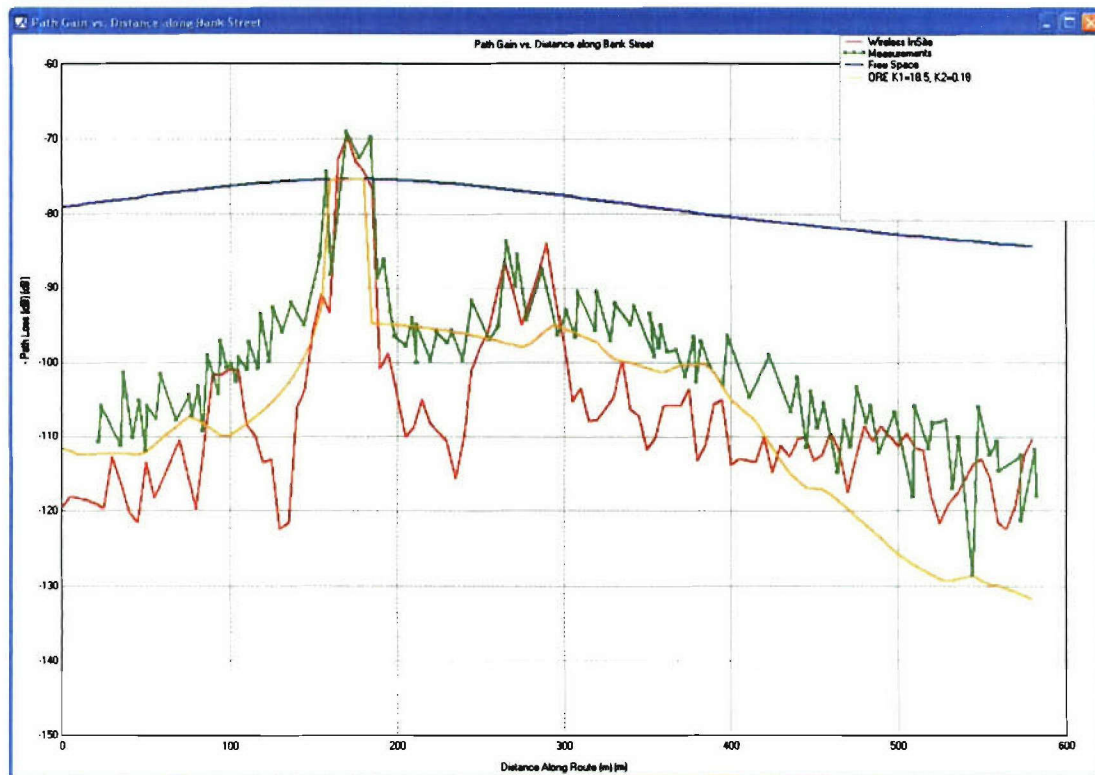


Figure 26: Comparisons of Path Gain on Bank Street, Ottawa Canada

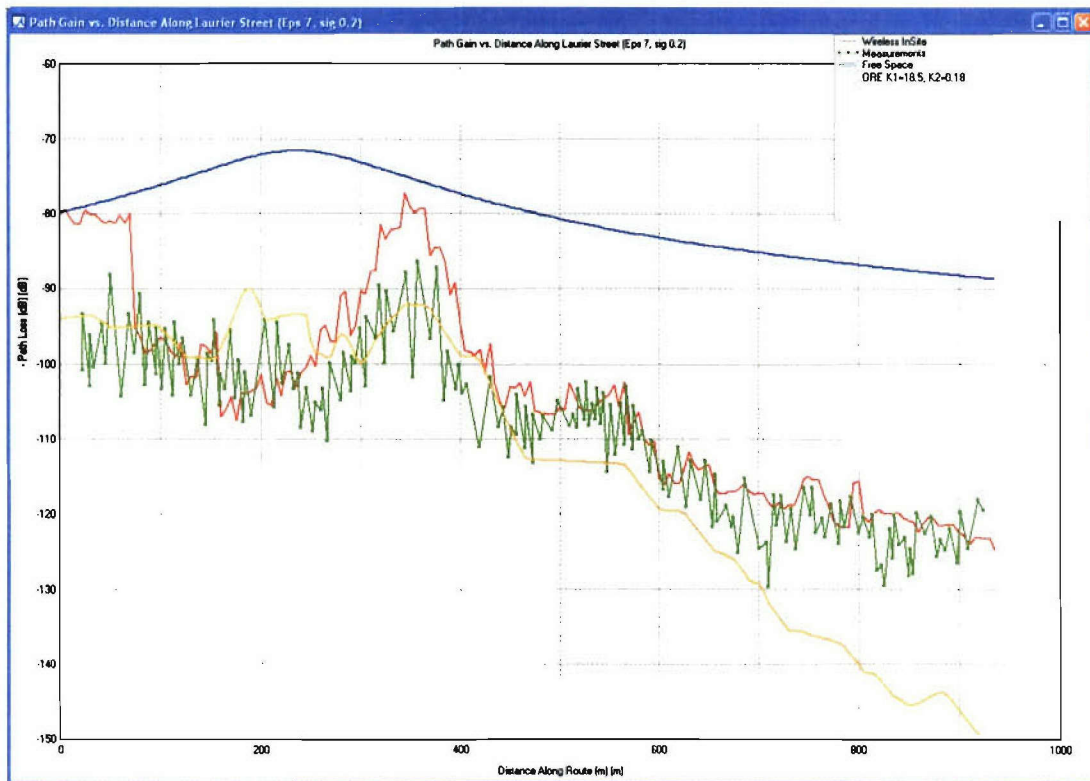


Figure 27: Comparisons of Path Gain on Laurier Street, Ottawa Canada

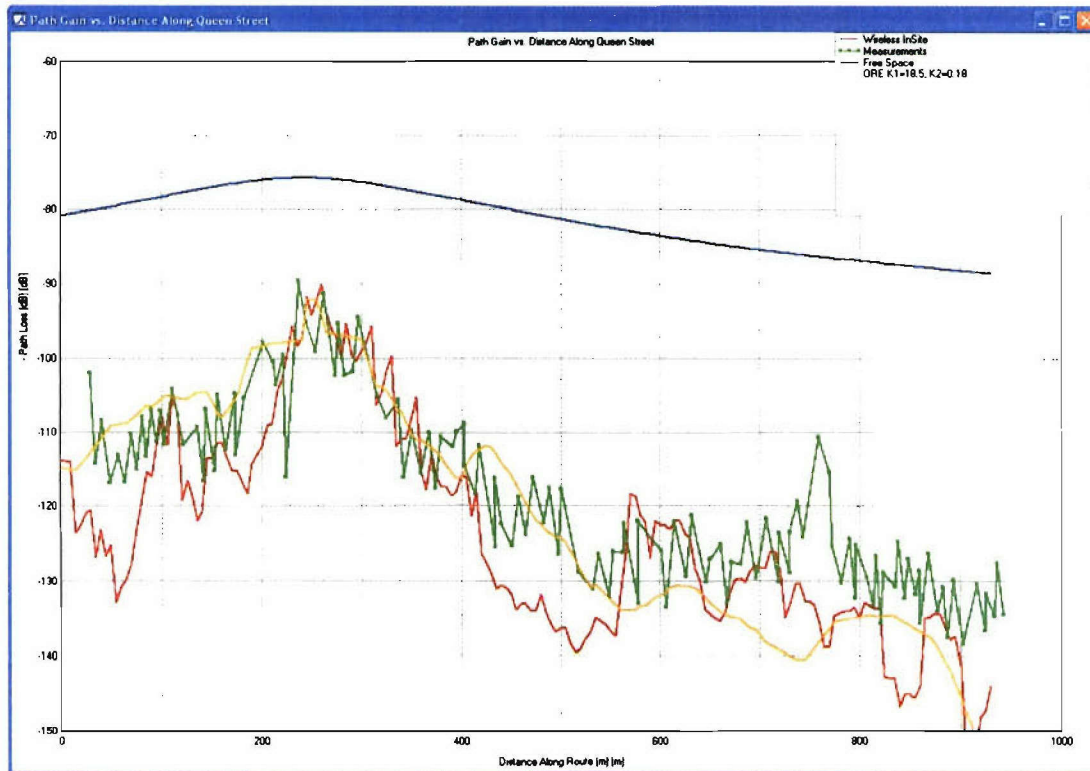
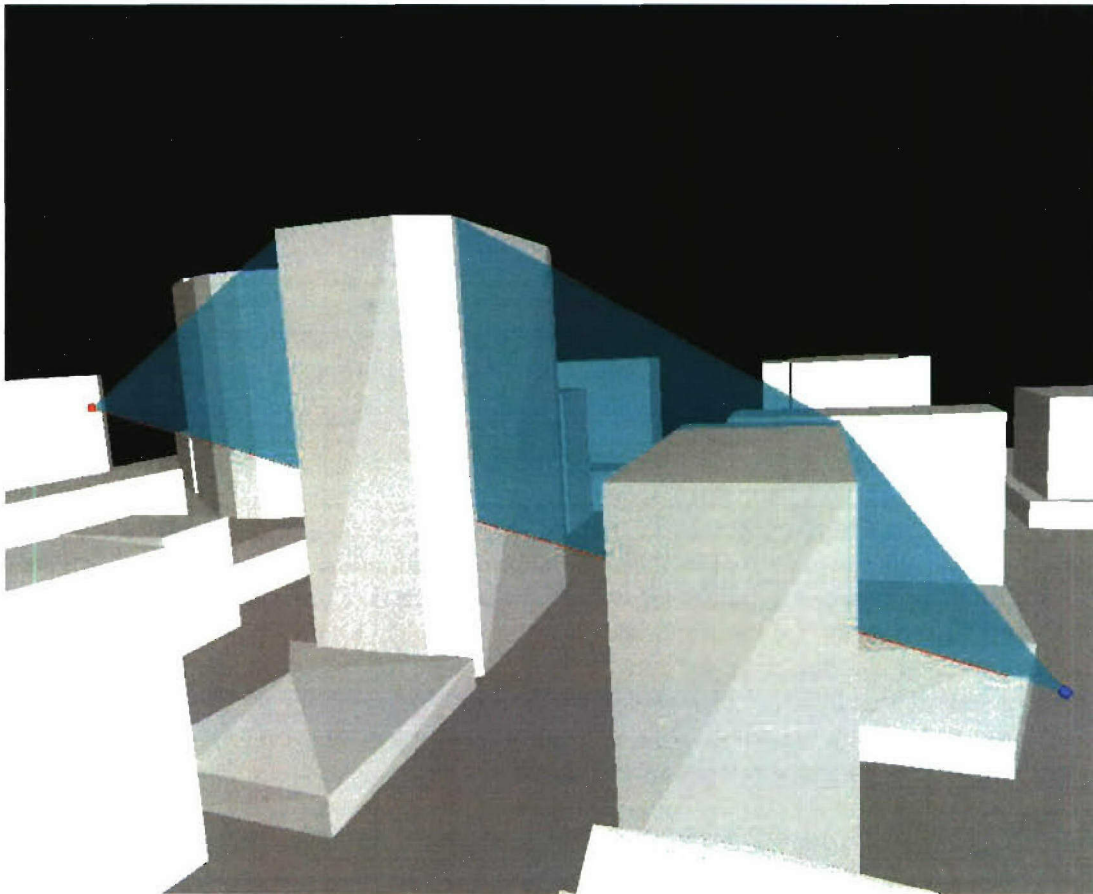


Figure 28: Comparisons of Path Gain on Queen Street, Ottawa Canada



Due to the semi-empirical nature of the fast prediction methods validation and tuning of the models are of great importance. Initial testing demonstrated in the above figures revealed the need to incorporate higher order propagation phenomena such as diffraction and reflection to account for discrepancies in long range paths that are dominated by such phenomena. How these effects and other geometric properties of the urban environment such as material definition, frequency, transmitter and receiver height, building geometry, and antenna pattern must all be factored into the model as appropriate weighting terms on loss functions has been the focus of current research. A series of tests was designed using REMCOM's Wireless InSite tool to study the effects of these properties using a GTD/UTD based urban canyon model and an Urban Canyon FDTD model. The results of these tests were then used as a baseline along with available measured results to tune the weighting parameters of the fast prediction model. Figure 29 and Figure 30 some of the higher order effects that can be determined by our fast model.



**Figure 29 Multiple over the roof top diffraction found by fast model**

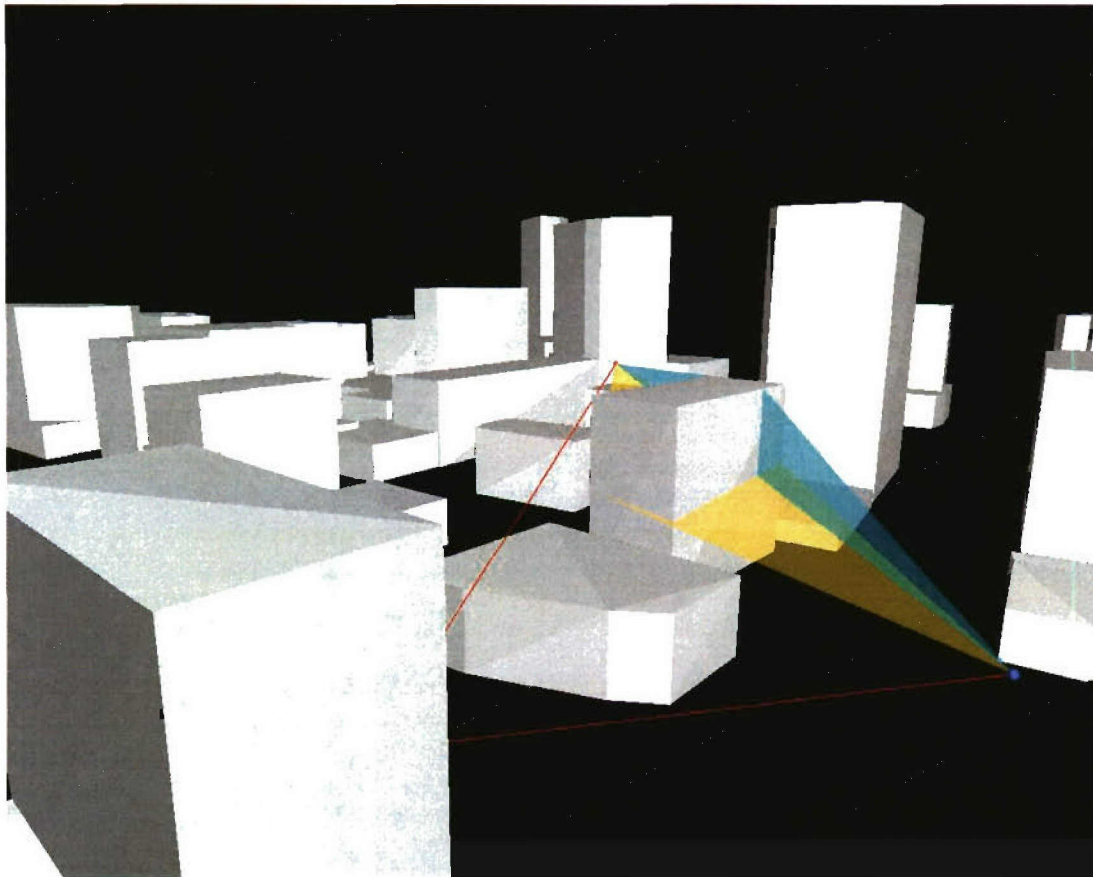


Figure 30 Multiple effects (horizontal plane diffraction, vertical over the roof top diffraction, and single reflections)

#### 4.2.2. Technical Details

The ORE engine makes use of spatial subdivision techniques and parametric traversal to compute a path through the urban environment. This path is composed of segments that are characterized by the media through which they are traversing. Each segment that occurs within an obstruction is attenuated using a statistical method based on its geometric characteristics. These segments are combined to provide a final path loss value on the order of 1000/second. If more time is available the engine will be capable of finding critical first order interactions and including these into the approximation for increased accuracy.

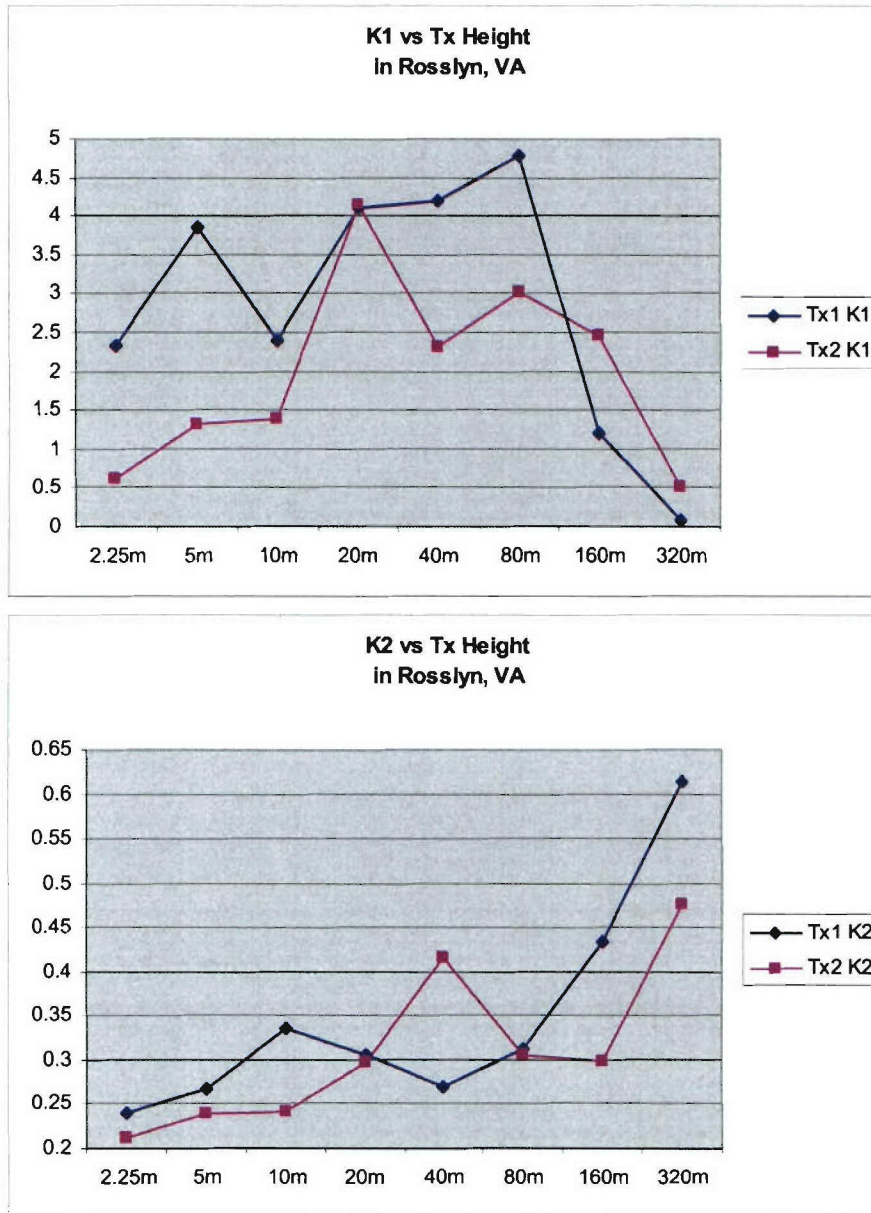
#### 4.2.3. MITRE Model

The MITRE model, [10], was selected to be the first model to test to meet the run time criteria. There are two tuning parameters available in this model. The attenuation due to buildings is described by the formula below.

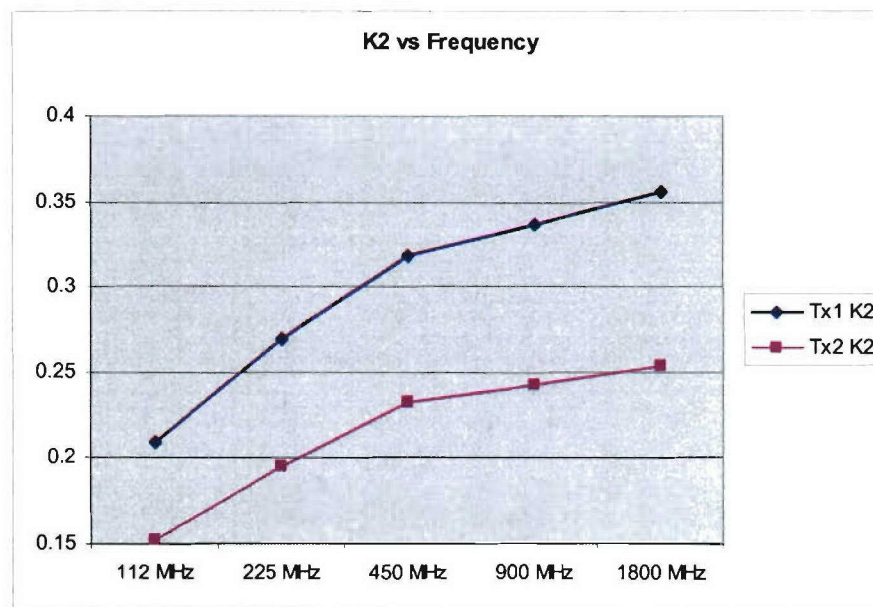
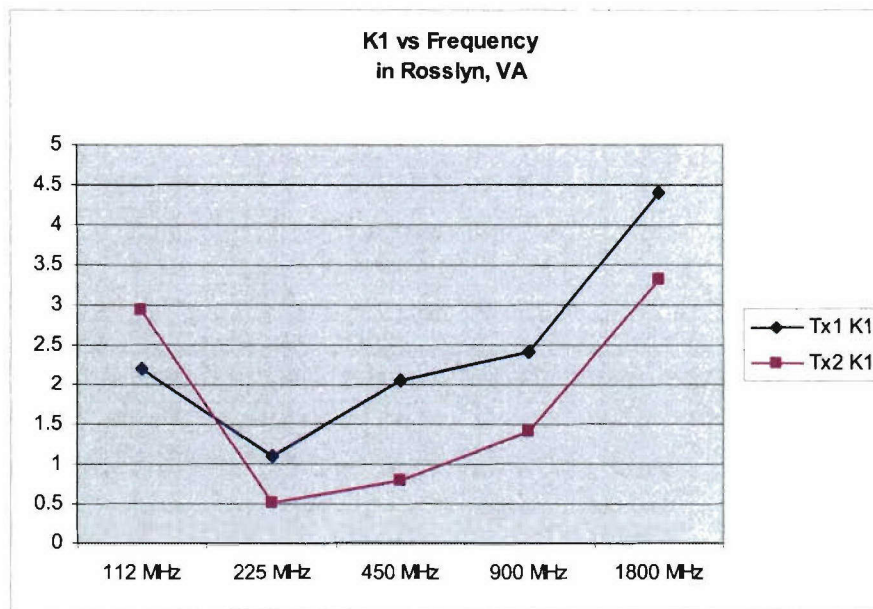
$$L_B = K_1 * (0.6)^f + K_2 * D_B$$

$D_B$  is the amount of building depth in meters;  $f$  is Frequency in GHz and the two  $K$  factors are used to tune the building attenuation.

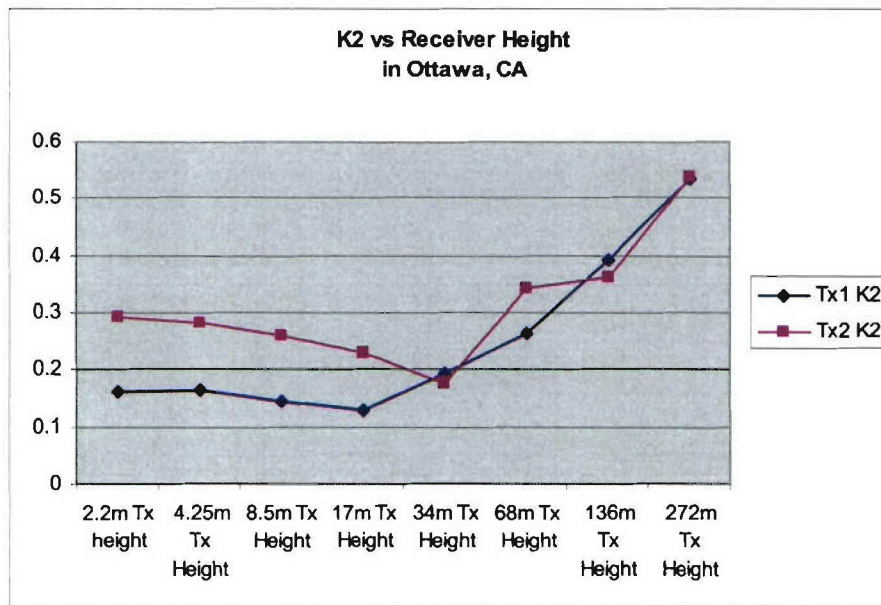
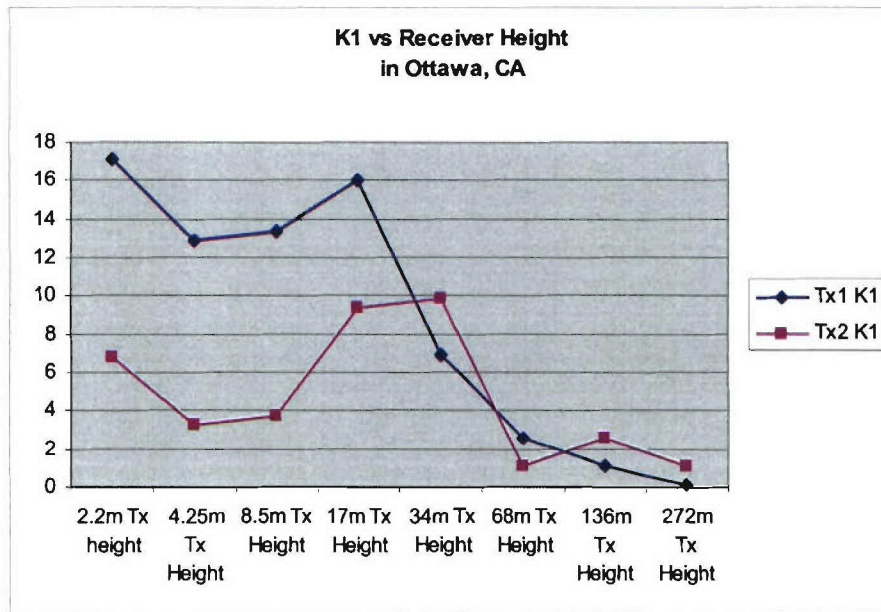
Given measured or calculated results, K factors can be tuned using a best fit line solution. Two approaches were available to alter these factors in each given scenario. If the factors were consistent throughout the given urban geometry, a high fidelity model could run as a preprocessing phase. Measured results in the cities of Ottawa, Bern, and Rosslyn were used in conjunction with Wireless InSite UTD calculated results to determine the consistency of the behavior in a given urban scenario. Below are graphs showing K1 and K2 vs Transmitter height and frequency in order to determine if they are constant on a per city basis.

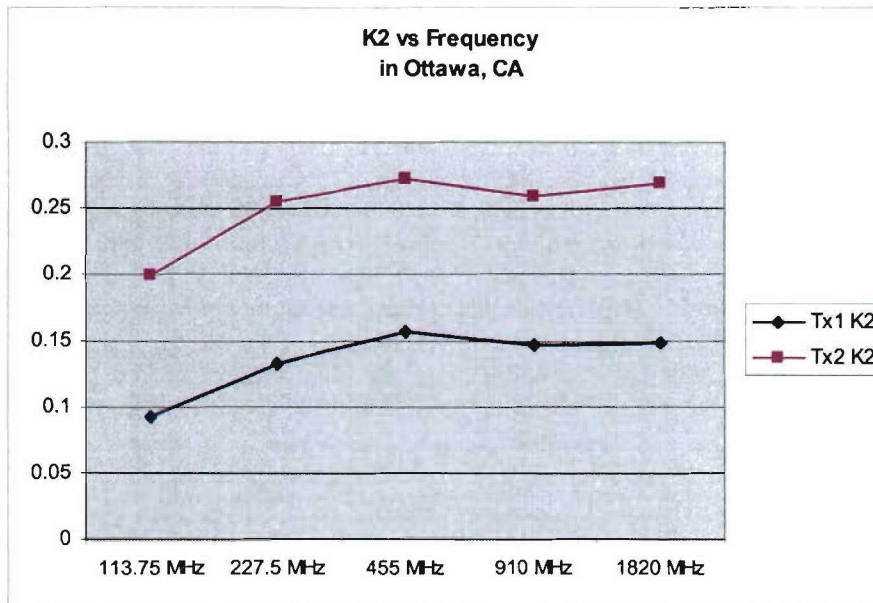
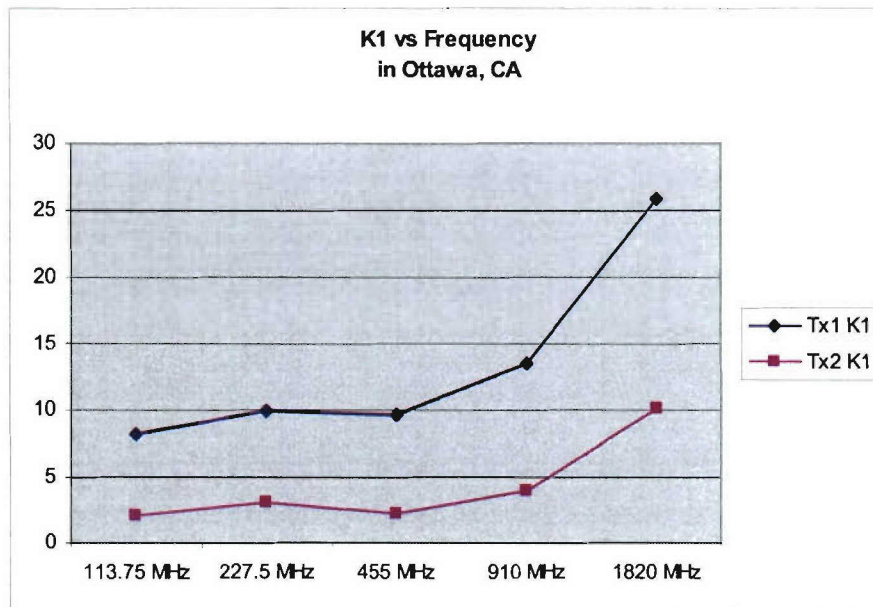








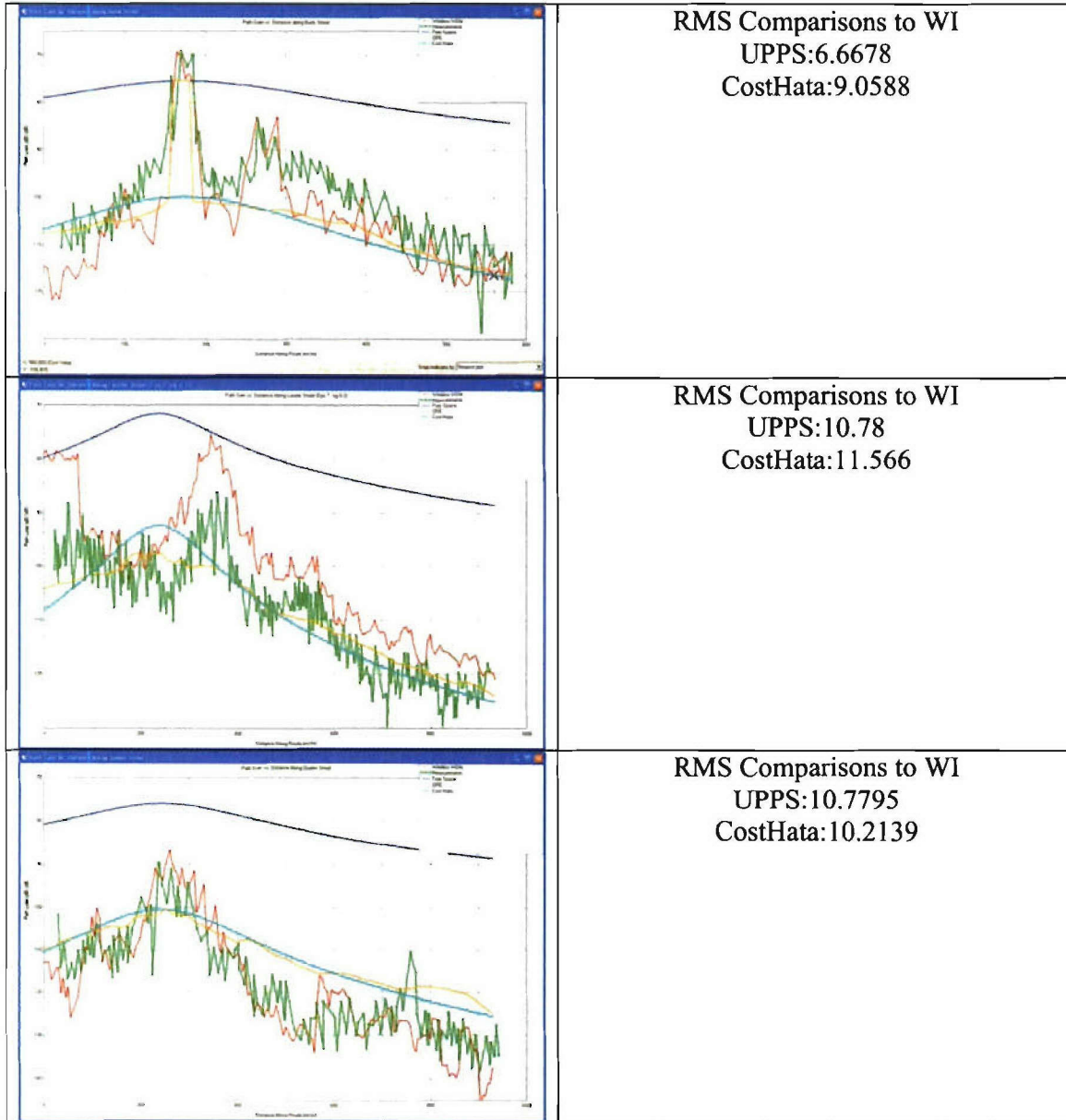


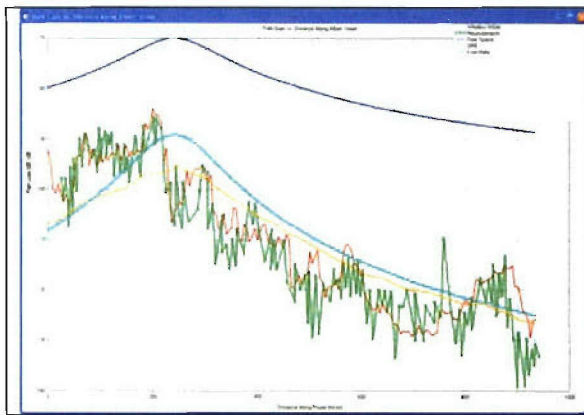


Once the analysis was completed it was clear that the factors were not consistent throughout the city and no correlation could be determined based on relative transmitter or receiver location.

Since the high fidelity tuning failed, our second approach was to tune the MITRE model using the empirical COST-HATA model. The theory being that COST-HATA was relatively good for certain scenarios, and could be more deterministic knowing building depth. Below are results for three cities using the MITRE model tuned with the empirical model.

**Ottawa**  
 $K1 = 37.9877$   
 $K2 = .0393$



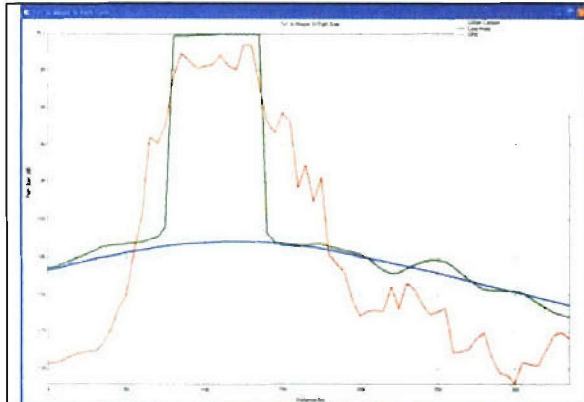


RMS Comparisons to WI  
UPPS:6.4895  
CostHata:7.435

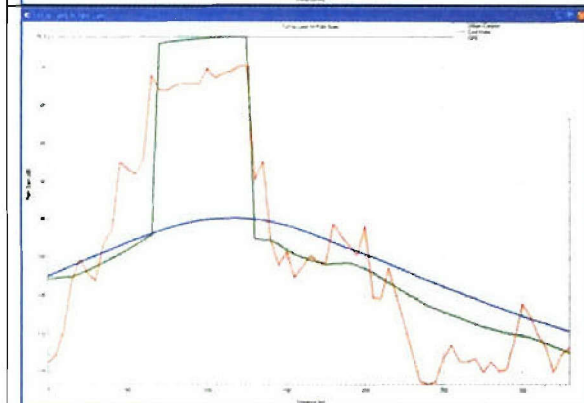
**Rosslyn**

K1 = 39.66

K2 = .0603



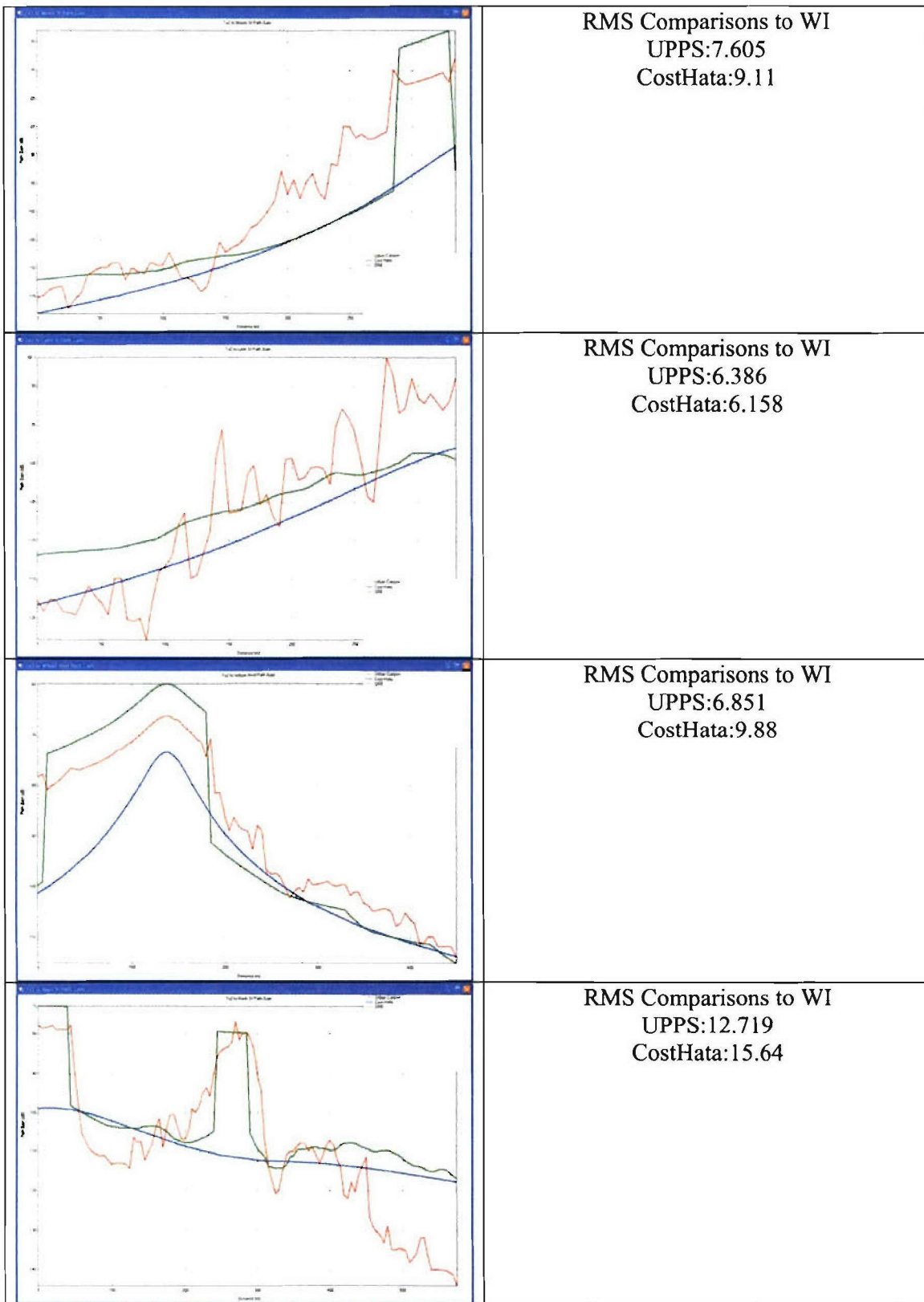
RMS Comparisons to WI  
UPPS:11.7255  
CostHata:13.348

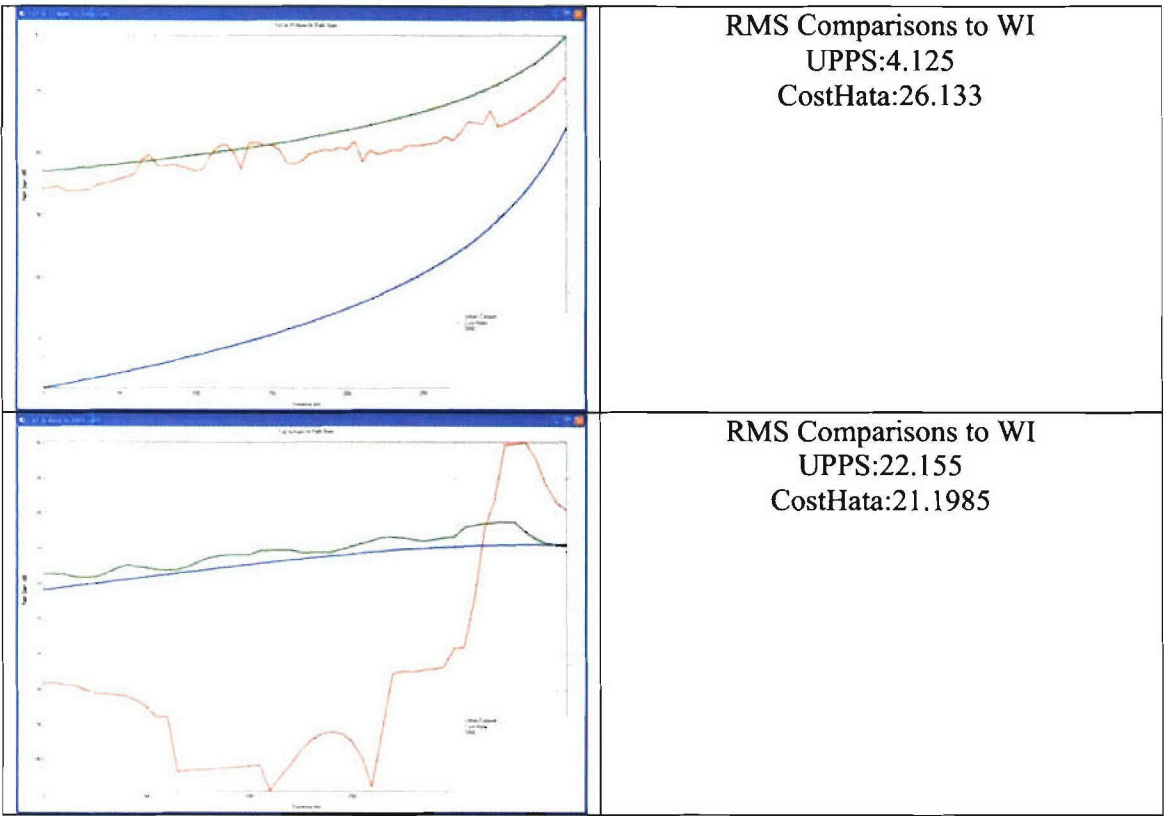


RMS Comparisons to WI  
UPPS:6.0763  
CostHata:10.3937

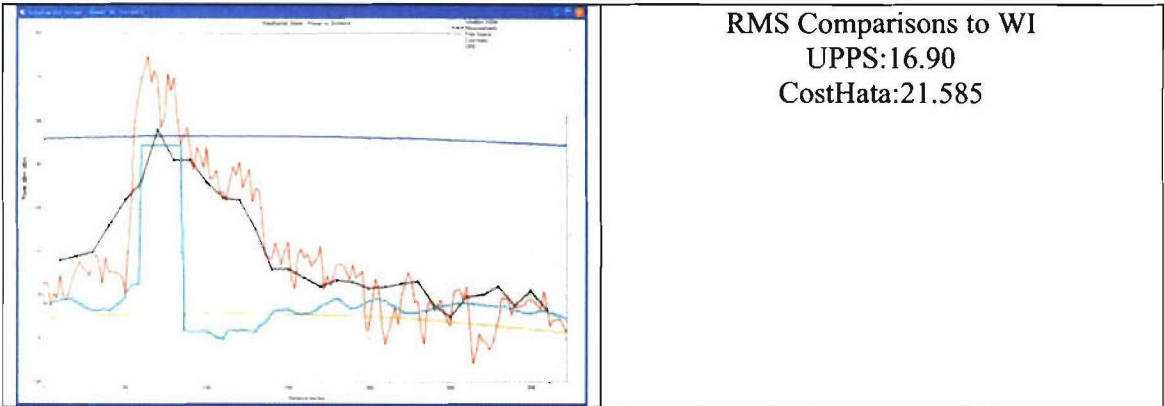


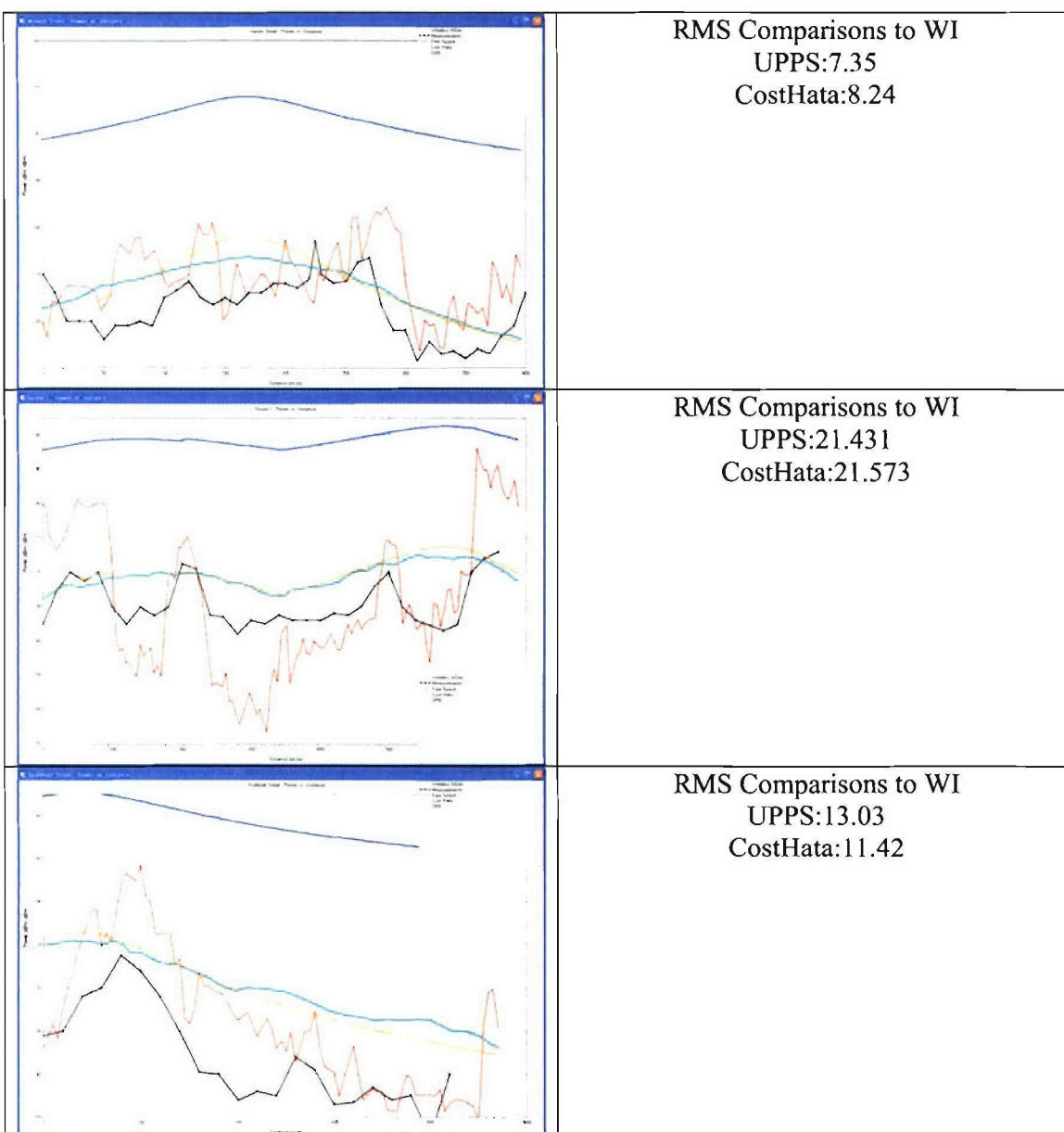
	<p>RMS Comparisons to WI UPPS:11.096 CostHata:14.048</p>
	<p>RMS Comparisons to WI UPPS:10.701 CostHata:16.419</p>
	<p>RMS Comparisons to WI UPPS:14.268 CostHata:16.738</p>
	<p>RMS Comparisons to WI UPPS:4.4344 CostHata:21.864</p>





**Bern**  
K1 = 80.79  
K2 = .0925





As seen from the graphs, the results are better than COST-HATA, but mostly only in line-of-sight regions. The conclusion from these tests is that tuning the MITRE model on-the-fly does not have the accuracy desired. Another drawback to using an empirical model to tune the MITRE model is that empirical models are only valid in limited environments.

From these two studies it became apparent that the MITRE model was not a viable solution for a fast accurate deterministic model. Efforts shifted towards researching other possible models.



#### **4.2.4. Other models**

The C-style API was used to integrate the newly developed fast urban models into network modeling tools such as OPNET and QualNet. Further an API manual was completed. In order to facilitate using the API, a sample program was written as an example for first time users. The API includes the following empirical propagation models:

- HATA
- Cost-HATA
- Freespace
- OPAR
- Extended Walfisch-Ikegami (WI) model.

Further to make it easier to use some of the models algorithms have been implemented to determine city type for HATA, Cost-HATA and WI depending on building heights and building densities.

As part of an effort to implement the vertical plane urban path method model, the new ray tracer was enhanced to quickly query the status of a point, whether it is outside, inside a building or inside the terrain. This method uses geometry pre-processing, edge caching, a method for fast vertical and horizontal convex hull determination. As the dominant path method is refined and the algorithm understood better, this method shall be included in the API.

### **4.3. Building Simplification**

#### **4.3.1. Two Dimensional**

##### **4.3.1.1. Simplification Technical Details**

A common problem for urban propagation is generating appropriate representation of the buildings. Too many faces on the buildings cause anomalous propagation results as well as extensive computation time. This will be especially troublesome when urban models are hybridized. Thus, an easy to use, transparent to the user, and computationally efficient method is required to simplify buildings. Remcom has investigated many methods from computer graphics to solve this problem. Recently Remcom tested an improved method for urban canyon propagation. This method successfully reduced the city shown in Figure 31 to one less than half the original size (Figure 32) and finally to a final rendition (Figure 33) that was 10% of the original size.



**Figure 31: DuPont Circle: Original (30,000+ vertices)**



**Figure 32: DuPont Circle: first level of simplification (14,430 vertices)**

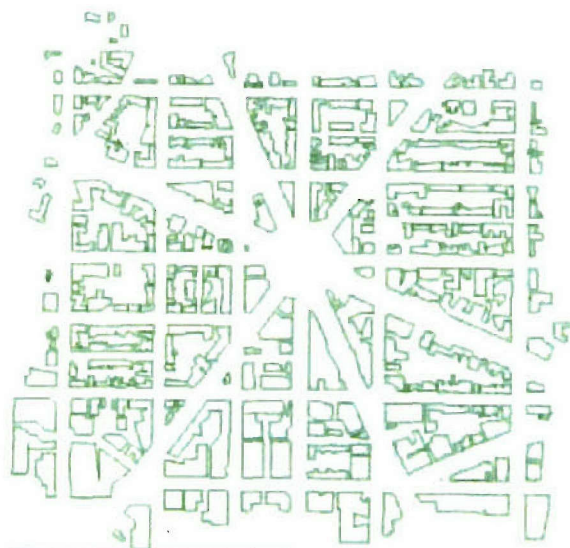


**Figure 33: DuPont Circle: final simplification (3,135 vertices)**

The simplified city models were then used to compute propagation loss (Figure 35) and the results were compared to the results found for a full-resolution city (Figure 34).

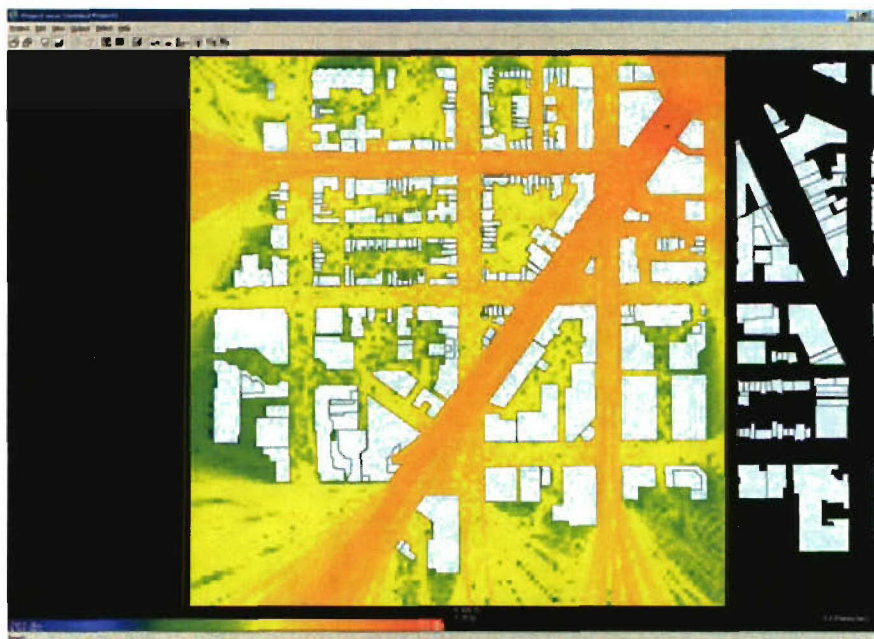


**Figure 34: DuPont Circle propagation coverage example with full building resolution**

In many areas the propagation loss is comparable. In fact the results seem to differ most in the inner courtyards. This is largely caused by the unioning groups of buildings into one.



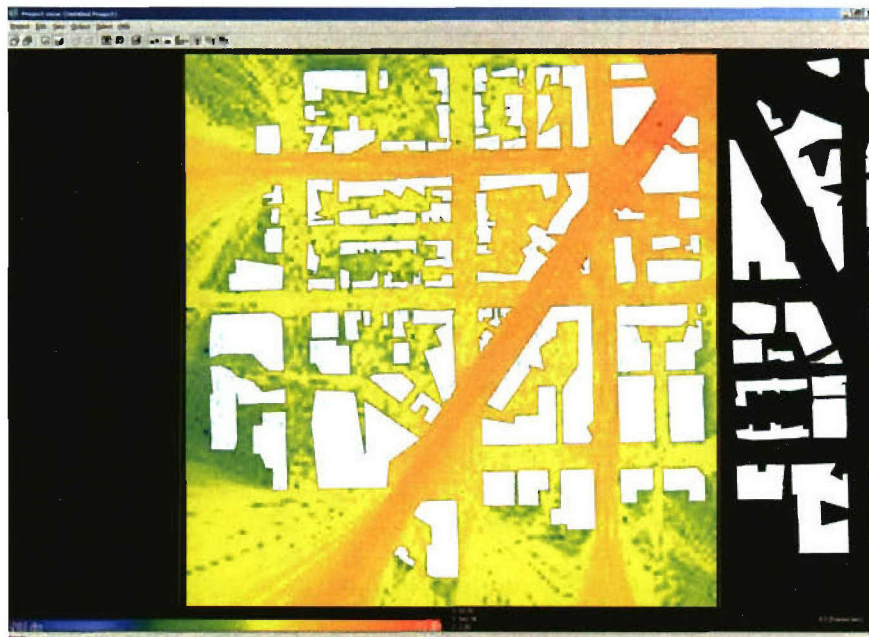


**Figure 35: Example of the above test with the simplified city.**

To better quantify the differences the loss was computed along the two routes shown in Figure 36, Figure 37, and Figure 38.

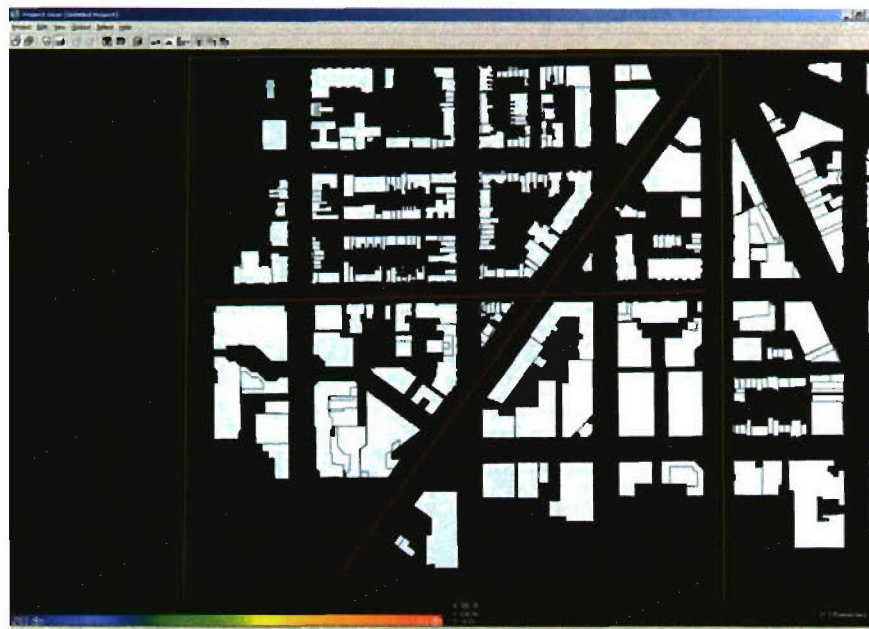


**Figure 36: Two example routes used to compare the results**

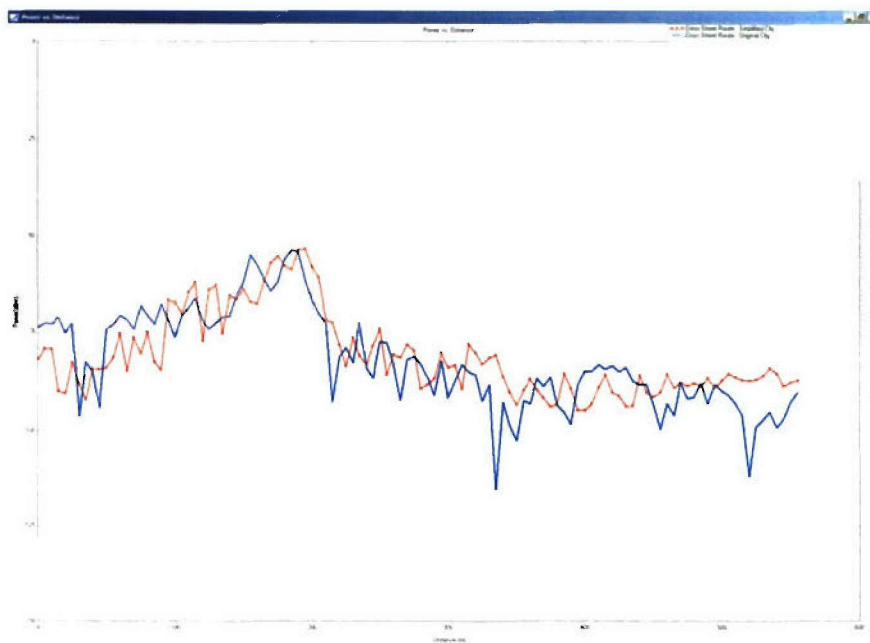


**Figure 37: The loss down the diagonal street for the original city (blue) and the simplified city (red)**

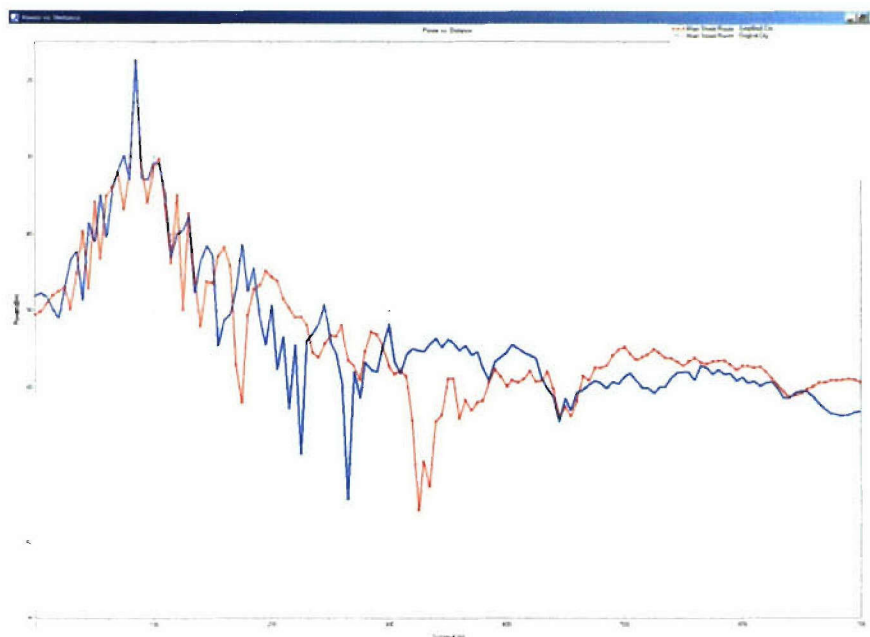


**Figure 38: The loss along the cross street for the original city (blue) and the simplified city (red)**

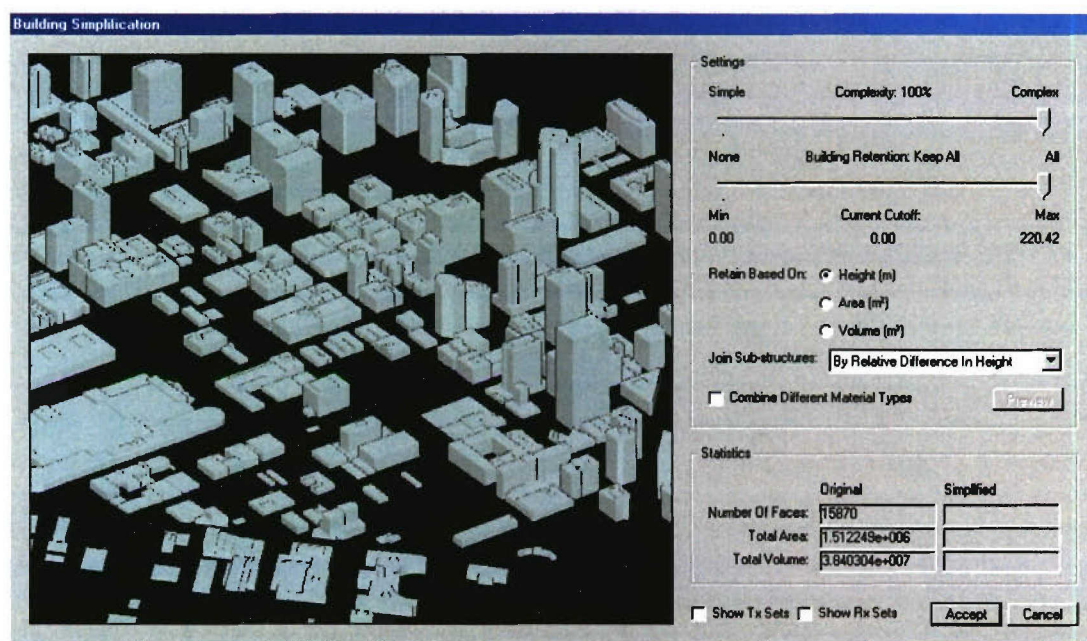
These methods to simply building footprints in support of urban canyon modeling were integrated into Wireless InSite®. The previous method applied sophisticated methods but was best applied to buildings of similar complexity. That is, often the tolerances for simplification for a complex building were too stringent for a simple building. Thus, global metric and corresponding algorithms are being developed to allow the user to use a single metric to achieve

varying degrees of building simplification over a large portion of a city. This involves balancing the reduction of simpler shaped buildings with those that are more complex. The Douglass-Pueker polyline simplification algorithm was modified to be performed on polygons. Utilization of this algorithm provides a global metric that is based on local variants. In our case a tolerance was constructed for simplification of a vertex within the building footprint using a percentage of the distance from the vertex to the footprint centroid. This tolerance acts as the tolerance found in Douglass and Pueker's initial work. A more in depth sensitivity study shall be constructed in order to validate that the building simplification does not unduly perturb the propagation predictions.

#### 4.3.1.2. Integration in Wireless InSite

The simplification library was utilized within Wireless InSite to perform building simplification.

The current simplification process opens a window as shown below.



The window has two sliders; one for controlling the amount of simplification to perform, and another that controls the amount of buildings to remove based on established criteria. The Complexity slider controls the tolerance parameter for the Douglass-Puecker simplifier that is used. Lowering the complexity raises the amount of tolerance that is allowed and therefore removes more points from the final product.

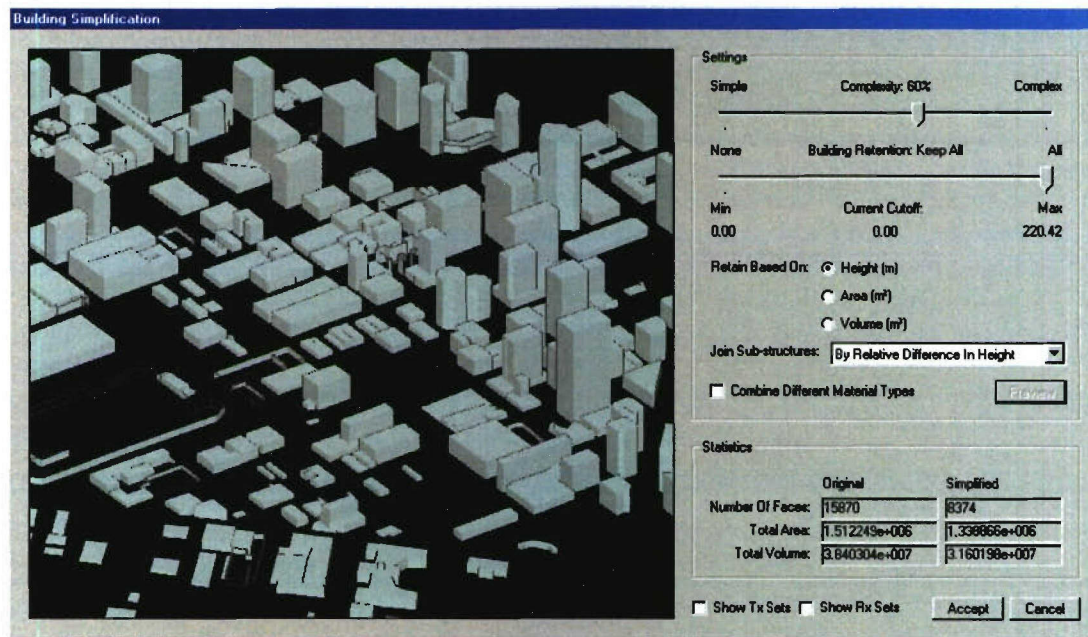
The Building Retention slider will control the minimum size that a building must have in order to be retained. At present, retention can be determined by height, area or volume. It was decided to keep all of these options as they make sense for different models. If you were to remove buildings based on area, then narrow towers would be removed that would be important. However, if you removed buildings based on volume, then the tower would be more likely to be retained over lower, broader buildings that might not be as relevant to the calculation. Buildings



with differing materials can be combined, but is provided as a deactivated option as materials play an important part in the final calculation.

Information is provided about the simplification process that shows how much of an impact the current settings have had. The user can also decide to show the transmitter and receiver sets of the project in the simplification window. This is useful for determining if the simplification process caused a building to envelope any or all points of a set, in which case the client may decide to increase the complexity in order to prevent this occurrence.

Here is an example of the simplification performed on the above geometry:



#### 4.3.2. Three Dimensional Simplification

Our efforts on building simplification focused on building foot prints in a 2 and 2.5D scenario. Although this method alone has shown promising results with urban canon FDTD testing it was sufficient to attain acceptable results and significantly reduce run times when using full 3D ray tracing. The problem of full 3D simplification is very difficult. Many areas of geometric modeling, computer graphics and finite element analysis have developed innovative algorithms for 3D triangular manifold simplification. These algorithms however are highly constrained on representations of geometry to fully connected well formed triangular meshes and often primary concern is with visual appearance of the model instead of the electromagnetic complexity. Couple this with the fact that urban models very rarely are represented within these constraints, and to modify the models to conform is an equally challenging problem, and many known methods become unusable. Therefore, research in this area was focused on more novel approaches that allow flexibility in model representation while reducing runtime requirements and maintaining accuracy in EM simulation.

One such technique investigated was introduced by Josilin, this technique attempts to retrieve the significant facet from a group of neighboring facets in the model geometry. This significant facet is then used to represent the entire group. One of the most attractive aspects of the method introduced is that it relies on spacing parameters that can be modified to have frequency dependence. This would allow custom model simplification based on frequency to enhance the accuracy of results. Other methods investigated include 3D feature extraction and removal.

The extraction of features was done using a pseudo Constructive Solid Geometry (CSG) approach. Once features are extracted they can be stored into a database according to electromagnetic size. In this scenario a Level of Detail (LOD) model could be constructed to only include the significant features at a given frequency. The difficulty with this method is the extraction of features which is very computationally intensive and not well defined in the literature.

## **4.4. Extended Semi-Empiricism for (Complex) Soil Permittivity**

### **4.4.1. Preface**

The initial approach to computing the soil dielectrics used a bi-cubic spline method. However, it was recognized that the bi-cubic spline methodology developed during the initial phases of this effort, while invoking the advantages of established two-dimensional interpolation techniques, sacrificed the full generality of a working algorithm with explicit dependence upon soil solids gravimetric fractions. The current algorithm features a refinement of an earlier intermediate process which retains the explicit dependence upon soil solids composition and uniquely permits a recent modification to include a composite of two established semi-empirical algorithms intended for the frequency ranges 300-1300 MHz and 1400 MHz -18GHz. The current report summarizes the essentials of the final algorithm with a particular emphasis upon the adaptation of semi-empirical methods.

### **4.4.2. Introduction**

A comprehensive numerical algorithm capable of evaluating complex permittivity of soil for arbitrary frequency, volumetric water content, and soil solids composition is constructed. The semi-empirical methods of Hallikainen and Dobson [13]-[14](1400 MHz-18GHz) and of Peplinski [15]-[16] (300 MHz-1300 MHz) are extended to lower frequencies (.01 MHz -50 MHz) by numerical modeling of measured data and supplemented by other interpolative algorithms to uniformly span the intended frequency range of .01 MHz to 18 GHz. The log of the permittivity as a function of frequency is displayed in Figure 39 which is labeled along the frequency axis to indicate the principal subdivisions within which the dominant data sources and methodologies determine the corresponding computational logic. As indicated in the figure, the semi-empirical methods of Hallikainen, Dobson and Peplinski [13], [14], [15] and [16] are utilized in the frequency range  $\nu > 300$  MHz. In an intermediate frequency range 1-50 MHz, the measurements of Campbell [11]-[12] collected at (1,2,5, 10,20 and 50)MHz are used to generate cubic polynomials in volumetric moisture at each frequency. The use of the polynomials to calculate complex permittivity in the range 1-50 MHz is then extended to the semi-empirical regime with an interpolative transition between 50 and 300 MHz. Finally the algorithm is extended to frequencies as low as .01 MHz with the measurements of Sternberg [17] for sand and Montmorillonite clay which are each reported at single values of moisture from .001 MHz to the lower limit of the second frequency range reported here as 1.0 MHz.



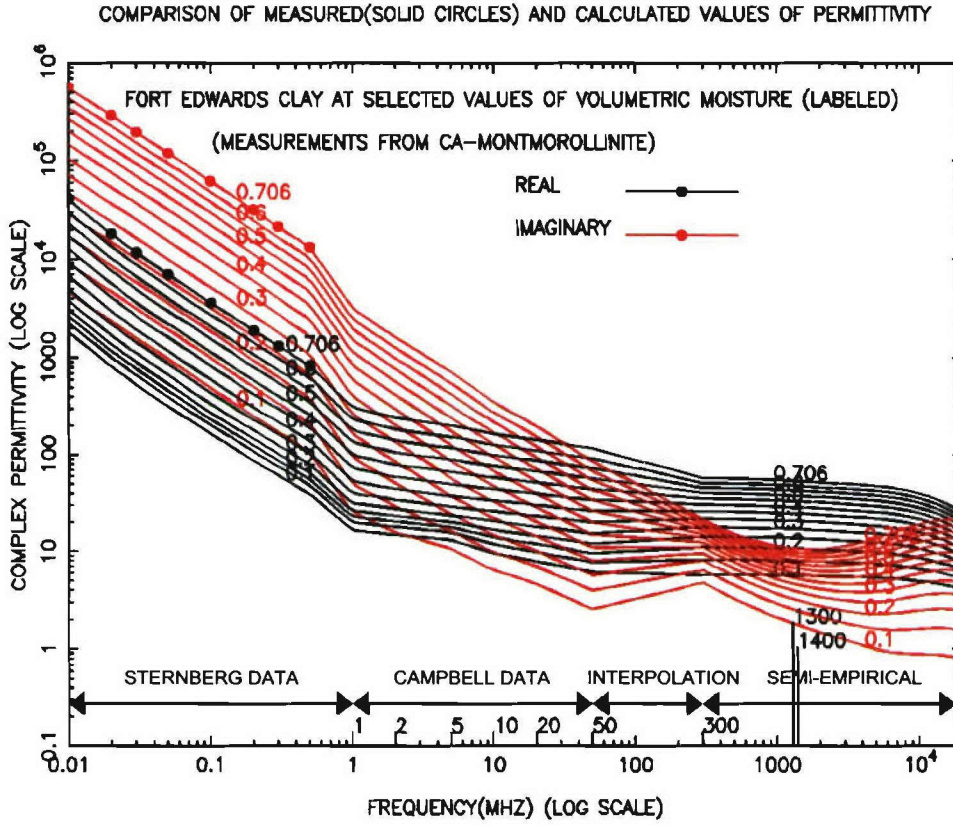


Figure 39

#### 4.4.3. Empirical Algorithm for Frequency Range 1400-18000 MHz

The original work of Hallikainen et al [13] and of Dobson [14] provided empirical methods consisting of polynomials quadratic in volumetric moisture at selected frequencies between 1400 MHz and 18 GHz. The coefficients of the quadratic polynomials were modeled as linear combinations of gravimetric fractions of the primary soil components silt, sand, and clay. Also provided was a semi-empirical algorithm which retained the desired dependence upon accessible physical soils properties such as volumetric moisture, bulk and specific densities, and (weight fractions) of the primary soil components of silt, sand and clay. The explicit form of the polynomials provided by Hallikainen and Dobson [13]-[14] (parametrically dependent upon frequency  $\nu$  and soil solids gravimetric fractions  $\overline{w_{si}}$ ,  $\overline{w_{sa}}$  and  $\overline{w_{cl}}$ , and explicitly dependent on volumetric moisture  $\overline{v_w} = \frac{v_w}{v_b}$ ) is given by

$$\mathcal{E}'(\{\nu, \overline{w_{si}}, \overline{w_{sa}}, \overline{w_{cl}}\}, \overline{v_w}) = \sum_{n=0}^2 c_n' \overline{v_w}^n \quad (1)$$

This expression for  $\mathcal{E}'$  is accompanied by an identical form for the imaginary part of the complex permittivity given by

$$\mathcal{E}''(\{\nu, \overline{w_{si}}, \overline{w_{sa}}, \overline{w_{cl}}\}, \overline{v_w}) = \sum_{n=0}^2 c_n'' \overline{v_w}^n \quad (2)$$

Each coefficient of a specified power  $n$ ,  $c_n$  is given by a linear combination of the weight fractions of the primary soil solids sand and clay and of the explicit form

$$c_n = a_{n0} + a_{n1} \overline{w_{sa}} + a_{n2} \overline{w_{cl}} \quad (3)$$

where the dimensionless scaled masses are given by the ratio of the respective component mass to that of (dry) soil according to the expressions

$$\overline{w_{si}} = \frac{w_{si}}{w_s} \quad \overline{w_{sa}} = \frac{w_{sa}}{w_s} \quad \overline{w_{cl}} = \frac{w_{cl}}{w_s}$$

The coefficients of like power from each of the varieties of soil may be understood to occupy the elements of a column vector which may be expressed as the product of a weight fraction matrix  $\mathbf{W}$  with rows corresponding to soil varieties and (three) columns corresponding to each of the three primary soil components which are silt, sand and clay.

$$|\mathbf{c}\rangle_n = \mathbf{W} |\mathbf{a}\rangle_n \quad (4)$$

Although theoretically more elegant semi-empirical formulations have been presented, the original empirical polynomials, which expressed real and imaginary parts of the complex permittivity as quadratics in volumetric moisture (with coefficients linearly dependent upon the soil solids gravimetric fractions) may retain their appeal for simplicity, replication of experimental data and dependence upon readily available soil physical quantities and because of the absence of a uniform semi-empirical algorithm for the entire frequency range of 300MHz-18GHz. This report will therefore consider the modeling provided by both the (empirical) polynomials and of the corresponding semi-empirical equations. As reported by Peplinski [15]-[16] the semi-empirical method may underestimate the real permittivity at 1400 MHz; in addition it has been observed locally that the equation for the imaginary part of the permittivity at 1400 MHz may provide non-physical (negative) results for soils with a dominant sand composition and at large values of volumetric moisture. Consequently the empirical model presented here is a modification of the polynomials reported by Hallikainen and Dobson in which the coefficient of the sand weight fraction in the expression for the quadratic coefficient of the imaginary component of sand at 1400 MHz ( $c_1 = -.313$  in Table II of reference [13]) has been divided by four. The plots shown in Figure 40 and Figure 41 display the behavior of a modified set of polynomials for the five varieties of the soil examined by Hallikainen and Dobson. [13]-[14]. Also shown as representative of measured data (as open circles) are results obtained from the original polynomials of Hallikainen and Dobson. The agreement is seen to be identical with the exception of the results shown for 1400 MHz for which the reported coefficients were modified as explained above. As it is the objective of this work to provide methods for estimating complex permittivity for soils of arbitrary solids texture composition, including those outside the loamy compositions considered by Hallikainen and Dobson, Figure 41 displays the behavior of the complex permittivity modeled by the empirical polynomials for the three primary soils represented by silt, sand and clay and selected to be of a composition suggested by the work of Campbell [11]-[12]. An alternative perspective of the empirical modeling in the frequency range 1400MHz - 18GHz is shown in Figure 42 and Figure 43 which display (for the five soils of the Hallikainen-Dobson study and for primary soils silt, sand and clay) both components of the



complex permittivity as a function of the logarithm of frequency at selected values of volumetric moisture. The original polynomials of Dobson and Hallikainen are used with the exception of 1400 MHz where the sand dependent coefficients of the (quadratic) coefficient,  $c_1$  was divided by a factor of four. The imaginary part of the permittivity, shown in red, is observed to exhibit the characteristic minimum above 1400 MHz as associated with the lower frequency effects of the free water relaxation near 20 GHz. Below 1400 MHz, the curves are extended by interpolation to the highest frequency studied by Campbell [11]-[12] at 50 MHz. (As will be discussed more thoroughly in later sections, the measured data of Sternberg for frequencies below 1 MHz are shown in the upper right and lower left panels of Figure 43, corresponding respectively to sand and clay. Both sets of data are observed to fall on the moisture curve which was selected for the corresponding component considered: .095 for sand and .706 for clay.) In the following section, the results of an alternative semi-empirical treatment are presented for the same selection of soil texture and physical parameters and frequency range as considered in Figure 40, Figure 41, Figure 42 and Figure 43.

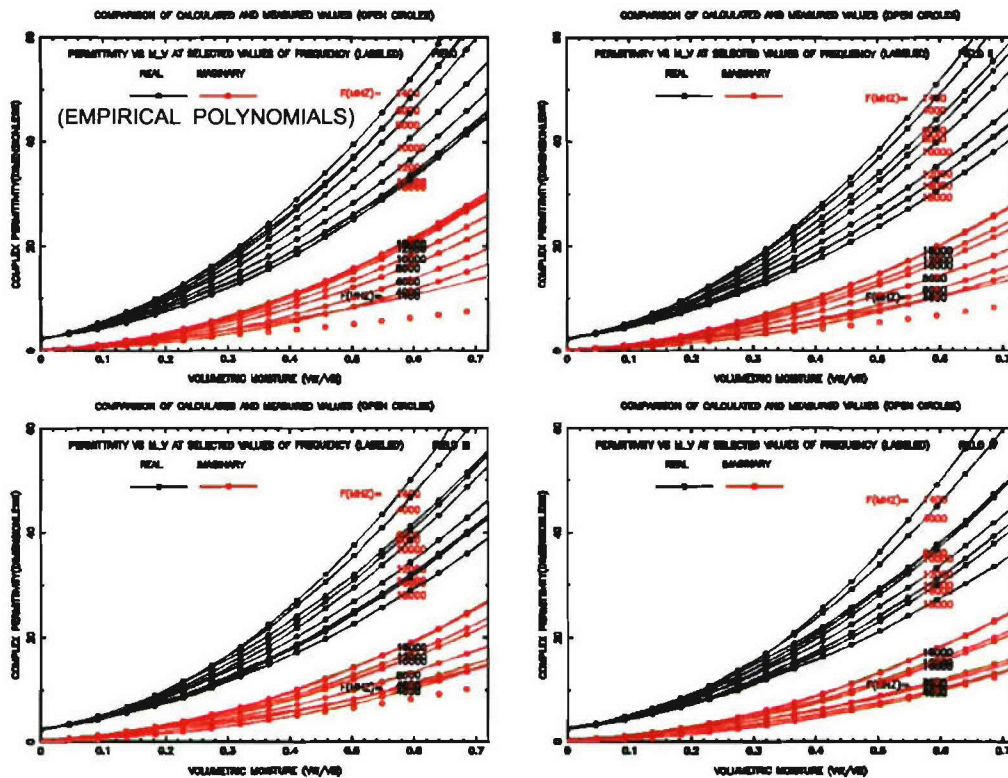


Figure 40



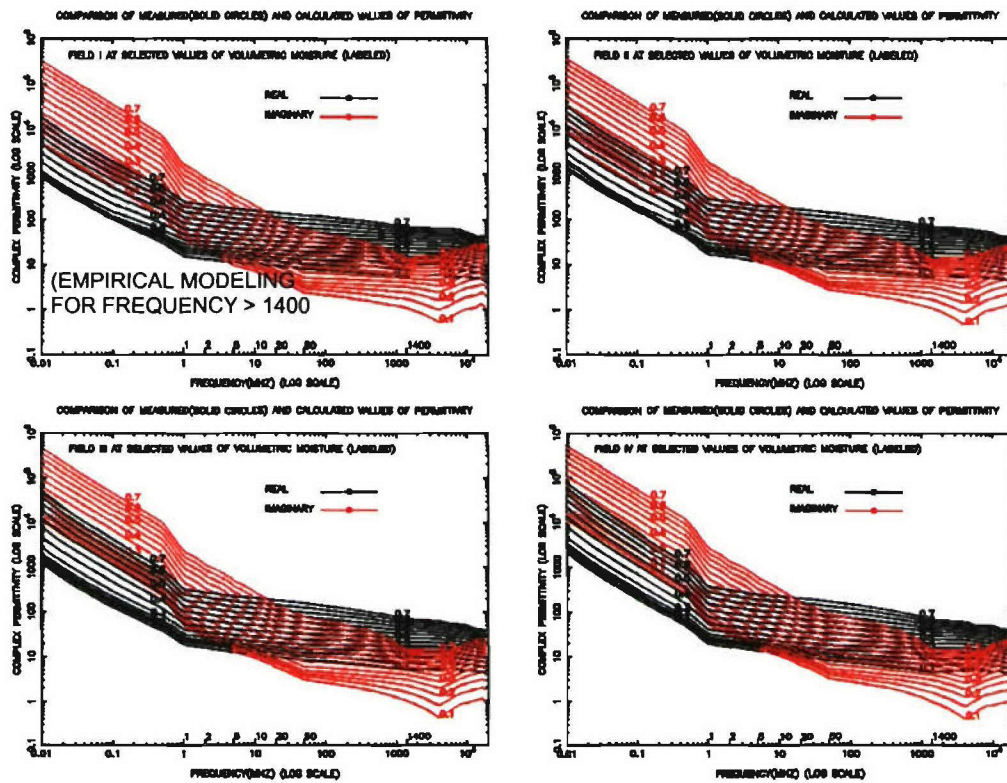


Figure 42



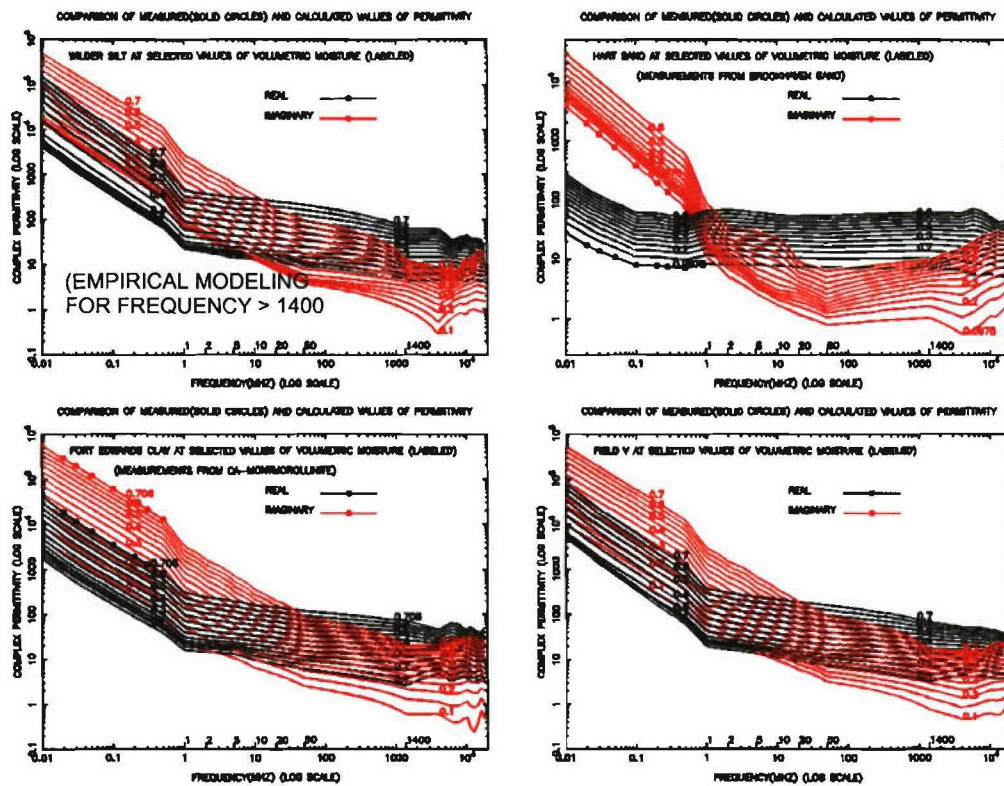
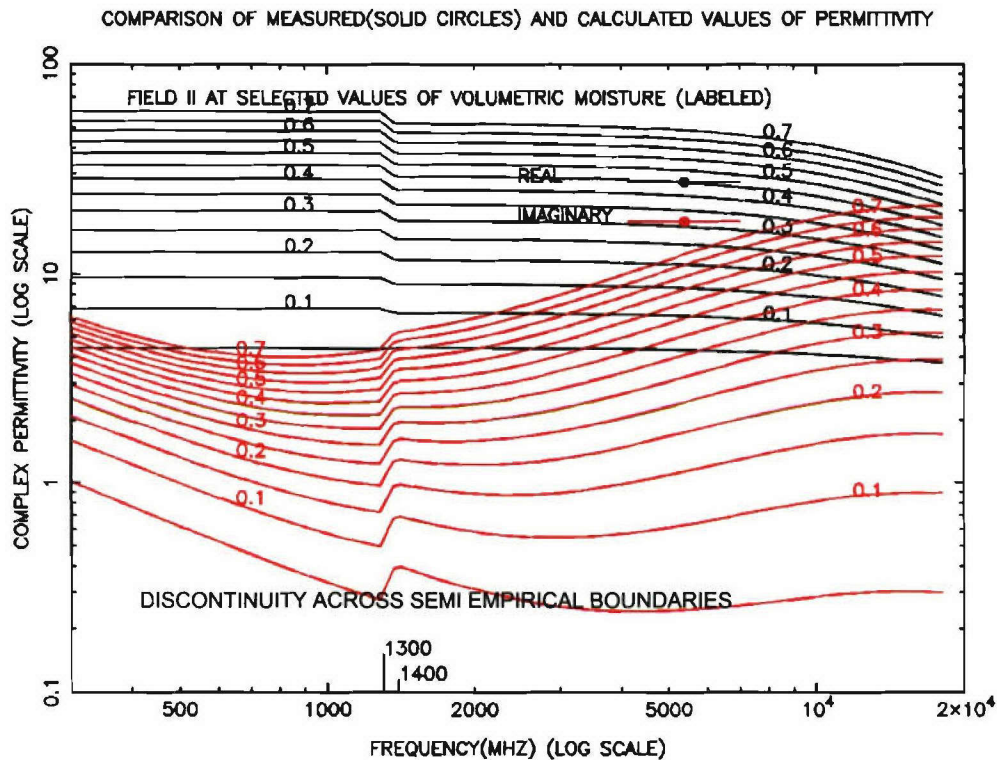


Figure 43

#### 4.4.4. Independent Semi-Empirical Algorithms for Frequency Ranges 300-1300 MHz and 1400-18000 MHz

The initial work of Hallikainen and Dobson [13]-[14] presented a set of parameters for a semi-empirical formalism based on a modified version of the Cole-Cole procedure for computing permittivity for aqueous suspensions and moist inorganic solids intended for the frequency range 1400 MHz -18GHz. Peplinski [15]-[16] later adapted the semi-empirical method for the frequency range 300-1300 MHz. Figure 44 is shown a representative plot, chosen as Field II from the work of Hallikainen and Dobson, of the entire semi-empirical frequency range of 300 MHz to 18 GHz in which each of these formalisms is implemented in its respective assigned range. A distinctive discontinuity is apparent in the intermediate frequency regime between 1300 and 1400 MHz. Peplinski's modification of the semi-empirical methodology involved a linear scaling and shift of the results obtained using the earlier model and provided an alternate (optimized) form for the effective conductivity.



#### 4.4.5. (Unified) Semi-Empirical Algorithm for Frequency Range 300-14000 MHz

The discontinuity between 1300 and 1400 can be diminished by introducing Peplinski's modified forms over a broader range (in the approach to the transition frequency from frequencies exceeding 1300 MHz) and with switching functions to introduce the changes gradually through a transitional continuum. (Whereas the original semi-empirical algorithm was intended for frequencies exceeding 1400 MHz, Peplinski extended the methodology with an alternate set of parametric equations for frequencies in the range 300-130a MHz. In the present work, a composite of the methods has been used for the full frequency range of 300 MHz-18GHz). The results for such a hybrid semi-empirical approach appear in Figure 45 where the discontinuity is essentially undetectable and the curves smoothly approach the two bounding limiting forms appropriate for frequencies above or below 1300 MHz. Figure 46 presents a larger frequency range perspective of these same results showing the interface between the semi-empirical methods above 300 MHz and the empirical polynomial modeling below 50 MHz. Shown in Figure 47 and Figure 48 are the results for permittivity as a function of volumetric moisture using the semi-empirical methodology for exactly the same frequency ranges and physical conditions as considered in the plots of the empirical results shown in Figure 40 and Figure 41. Whereas the agreement is less striking than that obtained with empirical polynomials, the semi-empirical method retains the appeal of its more theoretical motivation and structure and its adaptability to similar methods at lower frequencies. In addition the data points shown as open circles do not correspond to exact measurements but rather to numerical approximations of measured data. Figure 49 and Figure 50 display the semi-empirical results for complex

permittivity as a function of frequency for the same physical conditions and soil compositions as considered in the calculation of the empirical results shown in Figure 42 and Figure 43.

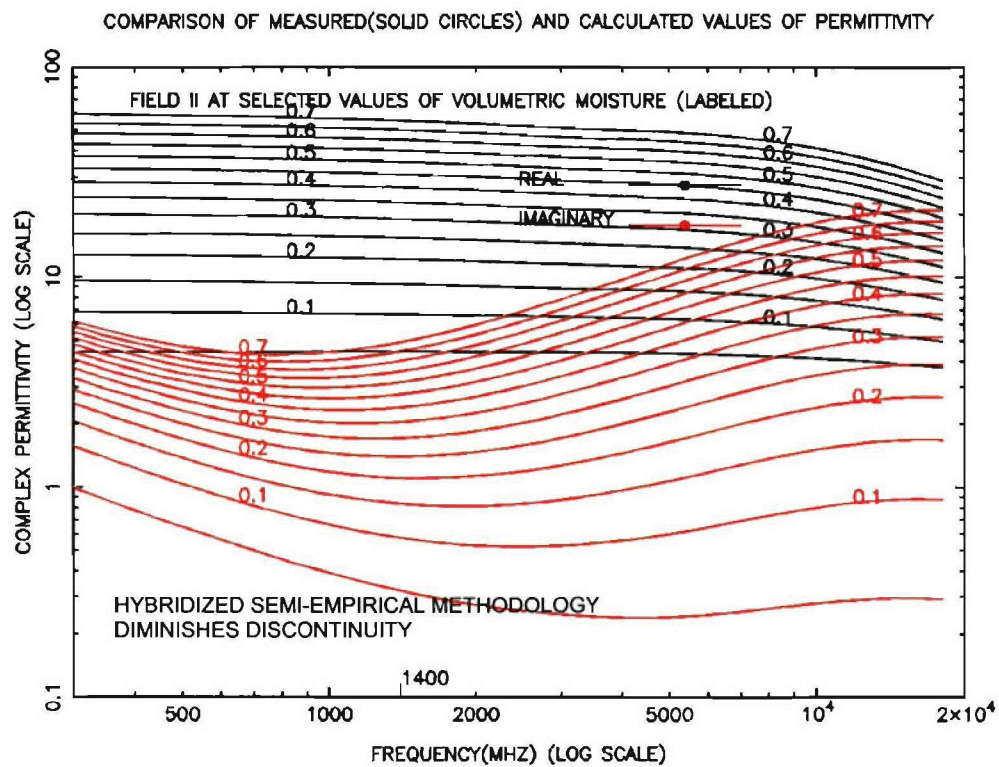


Figure 45



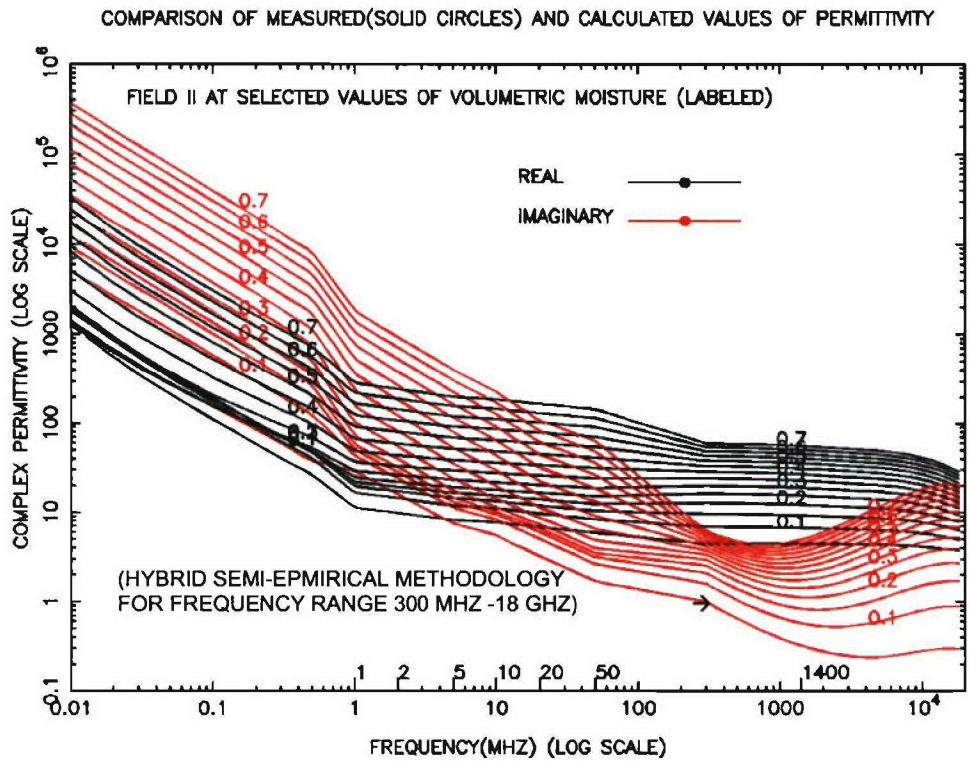


Figure 46

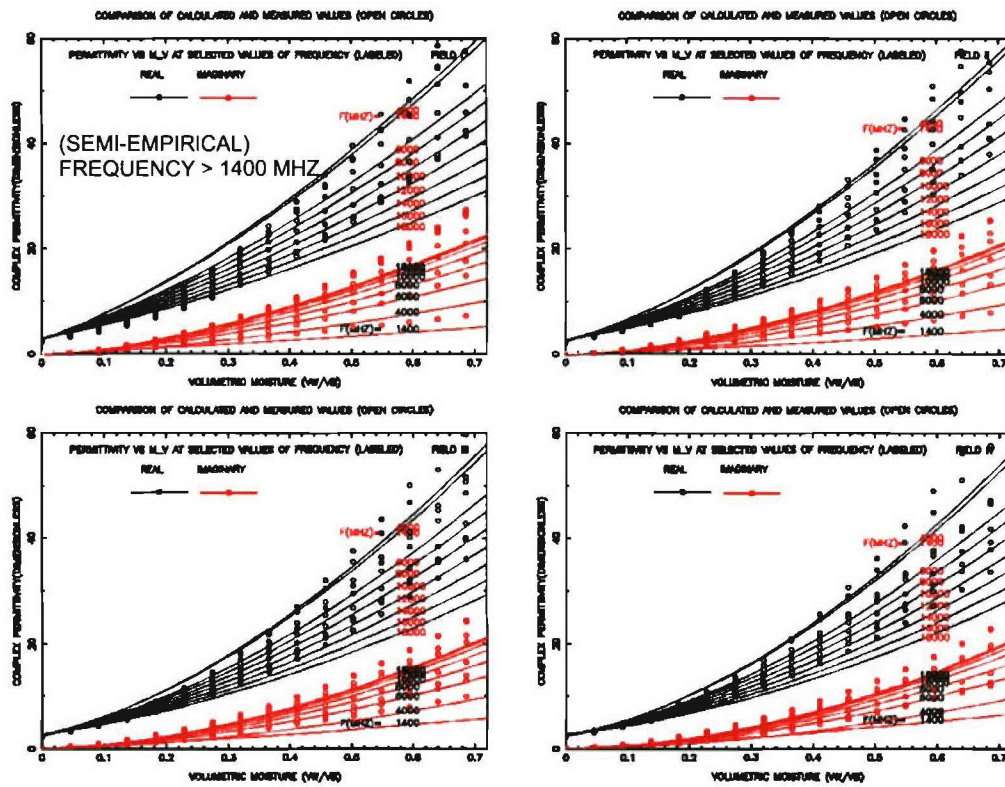


Figure 47

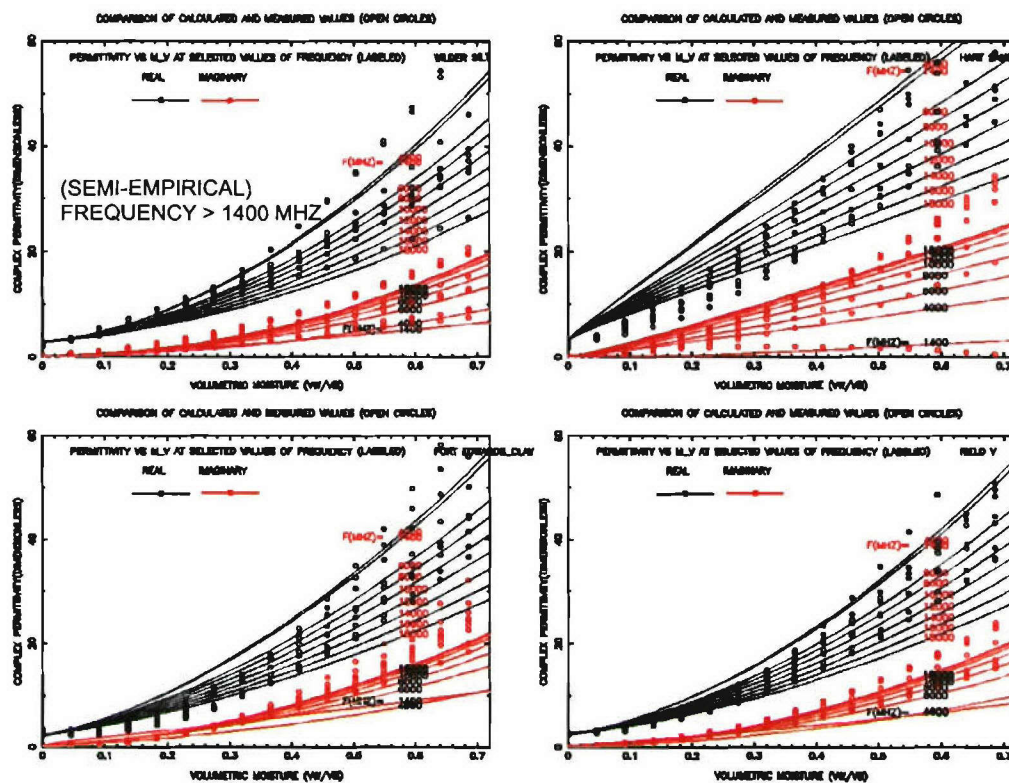


Figure 48



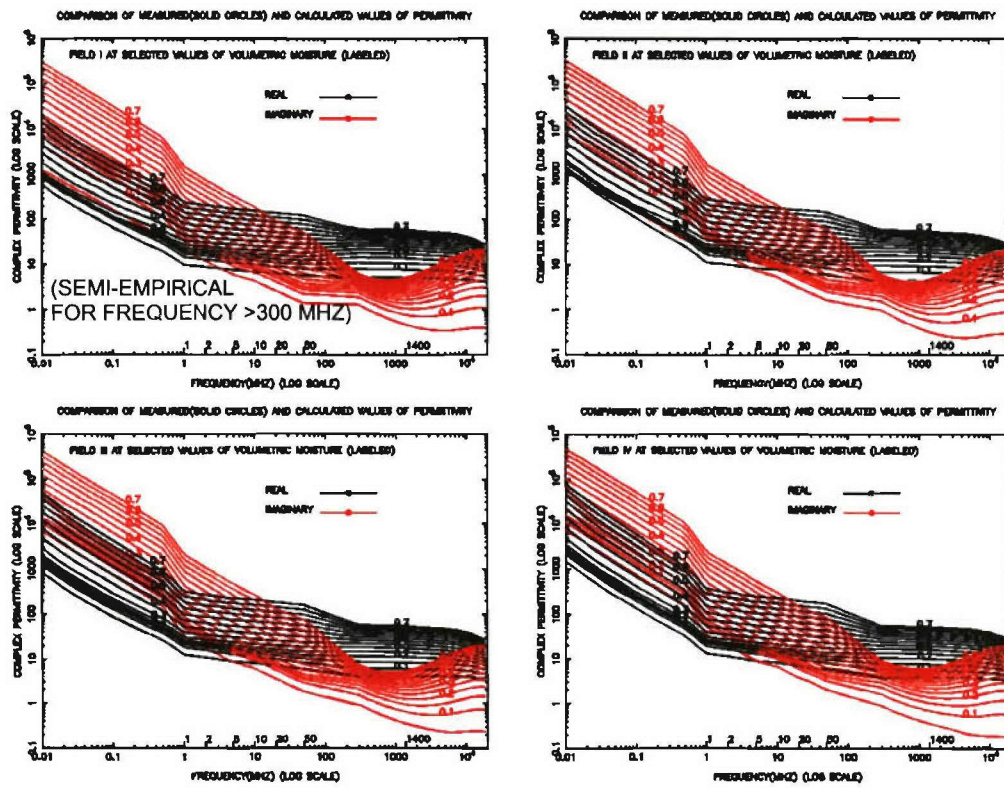


Figure 49

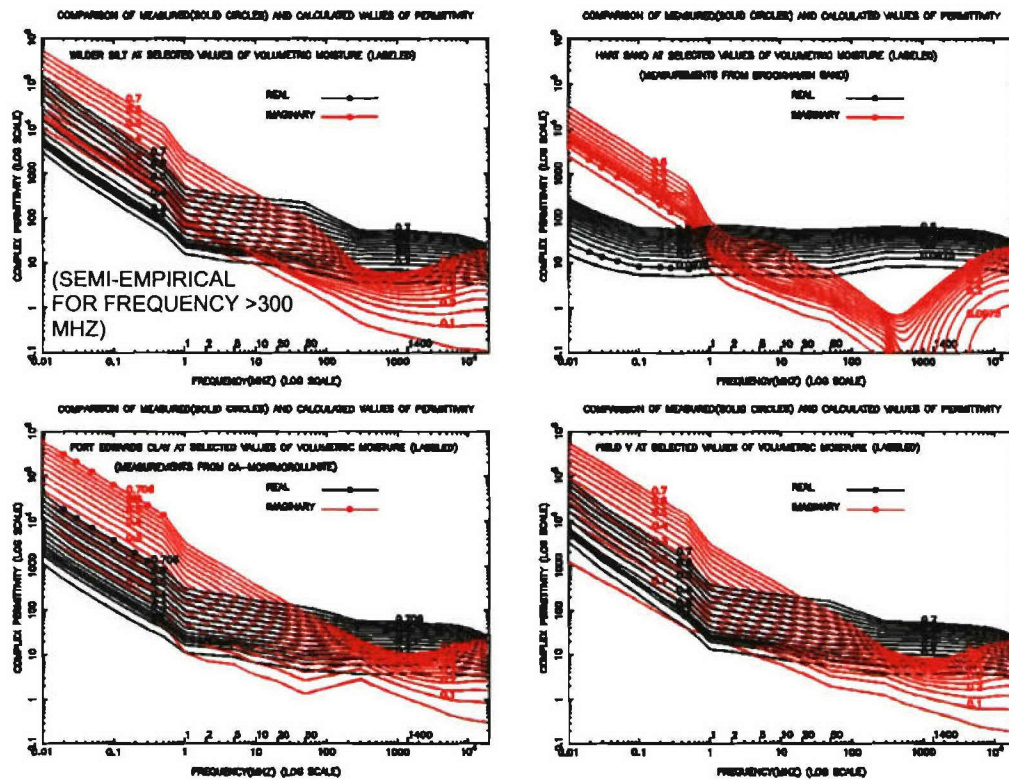
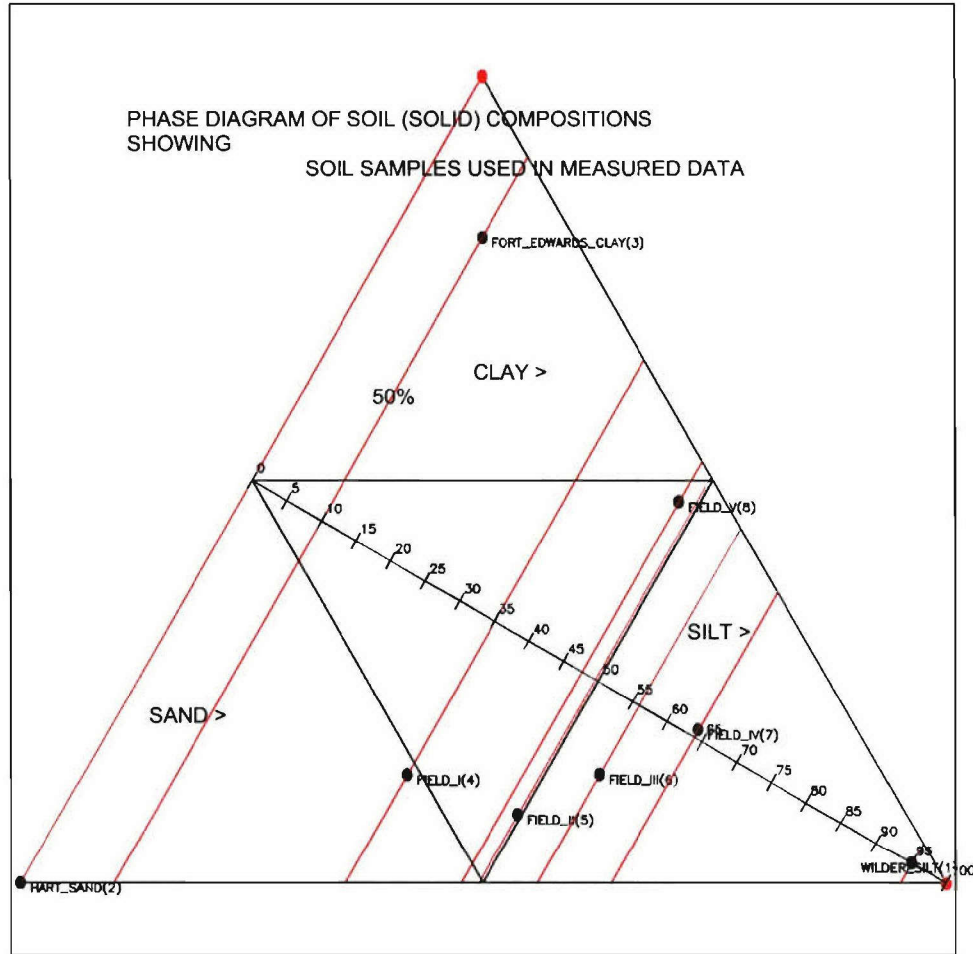


Figure 50

#### 4.4.6. Applied Linear Regression Analysis in the Frequency Range 1-50 MHz

In order to construct a comprehensive numerical algorithm capable of evaluating complex permittivity for arbitrary frequency, volumetric water content, and as a function of the weight fraction of the primary solid components silt sand and clay, it is required to collect sufficient data which adequately spans the full range of the mixtures understood to comprise soil solids. The numerical curve fitting (of permittivity as a function of moisture content and soil solids composition) of Dobson [14], provides an initial model of the desired functional dependence but restricted to the frequency range 1400-18,000 MHz. As becomes apparent from the phase diagram in Figure 51 where the soil compositions considered by Dobson are indicated by solid black circles numbered 4,5,6,7 and 8 (corresponding to his designations Fields I, II, II, IV and V respectively), the soils considered are relatively localized to the (central) loam and silt triangles and cannot be expected to adequately characterize soil sample significantly displaced into the sand and clay triangles. The data of Campbell [11]-[12], in its consideration of the primary soil varieties (Wilder) silt, (Fort Edwards) clay and (Hart) sand extends the data set to the primary extremes of the phase diagram introducing the red circles at each of the three vertices. The data of Campbell is also of interest in its consideration of frequencies below the lower limit of the Dobson range of 1400 MHz to include measurements at (1,2,5) MHz and (10,20, 50) MHz. Experimental data for even lower frequencies is found in the studies of Sternberg [17] who explores the full range of frequencies 0.01 - 100.00 MHz for Ca-Montmorillonite (clay), natural sand (Avra Valley), and for pristine (Brookhaven) sand, assumed to correspond to the lower left vertex of the sand triangle.



**Figure 51**

The data of Campbell [11]-[12], provided in graphs as a function of volumetric moisture at six frequencies was digitized and processed by linear regression analysis to extract the best coefficients for a polynomial of third order in the volumetric water content. The results for the modeling of the data of Campbell (including digitized measurements and modeling as cubic polynomials) at each of the six frequencies considered by Campbell are shown in Figure 52, Figure 53 and Figure 54 for Wilder Silt, Hart Sand and Fort Edward's clay, respectively. Plots of the logarithm of permittivity for otherwise identical physical conditions are shown in Figure 55, Figure 56 and Figure 57. The modeling expresses the permittivity as polynomial cubic in the (fractional) moisture content according to the expressions

$$\varepsilon'(\{v, w_{si}, w_{sa}, w_{cl}\}, m_v) = \sum_{n=0}^3 c'_n m_v^n$$

$$\varepsilon''(\{v, w_{si}, w_{sa}, w_{cl}\}, m_v) = \sum_{n=0}^3 c''_n m_v^n \quad (5)$$



This formalism is extended to arbitrary composition by assuming that the coefficients in the above equation may be expressed as a linear combination of their compositional fractions in silt sand and clay

$$|c>_n = W |a>_n \Rightarrow |a>_n = W^{-1} |c>_n \quad (6)$$

where the column vector consists of a coefficients ( $|c>_n$ ) of the nth power from each of the three independently modeled soils. The unknown combinatorial coefficients  $|a>$  are obtained through inversion of the composition matrix W. The composite modeling of the primary soils in the intermediate range as described above extends the lower frequency range of permittivity as a function of frequency and moisture content at arbitrary soils solids compositions from 1400 MHz to 1 MHz.

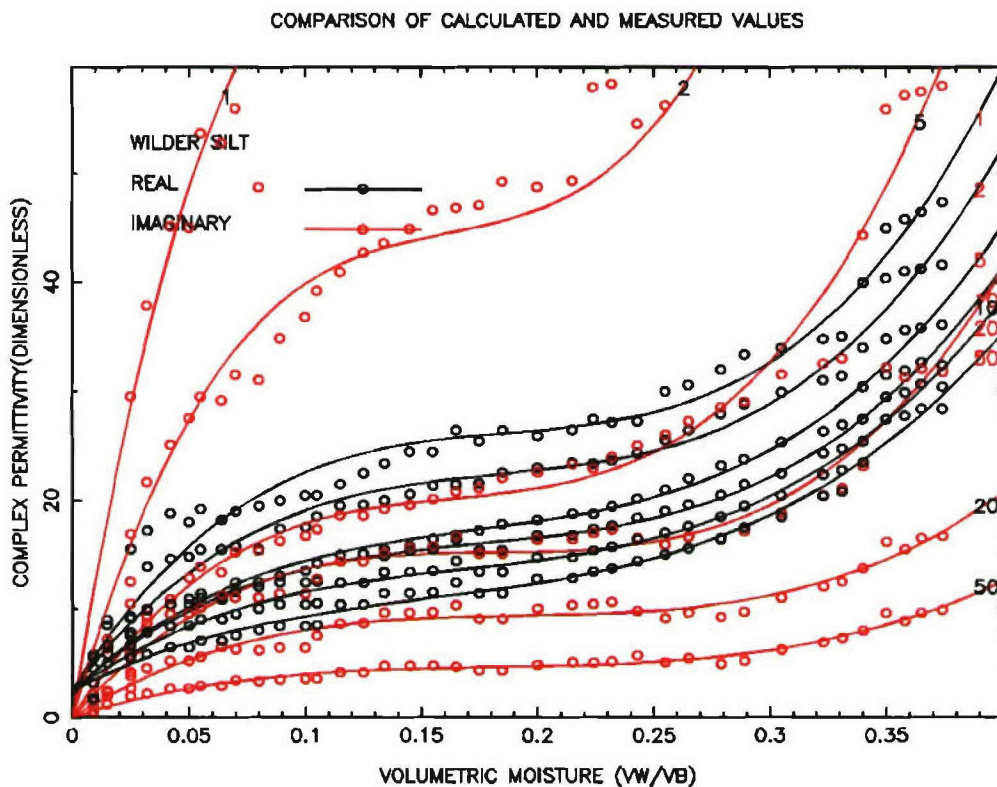


Figure 52

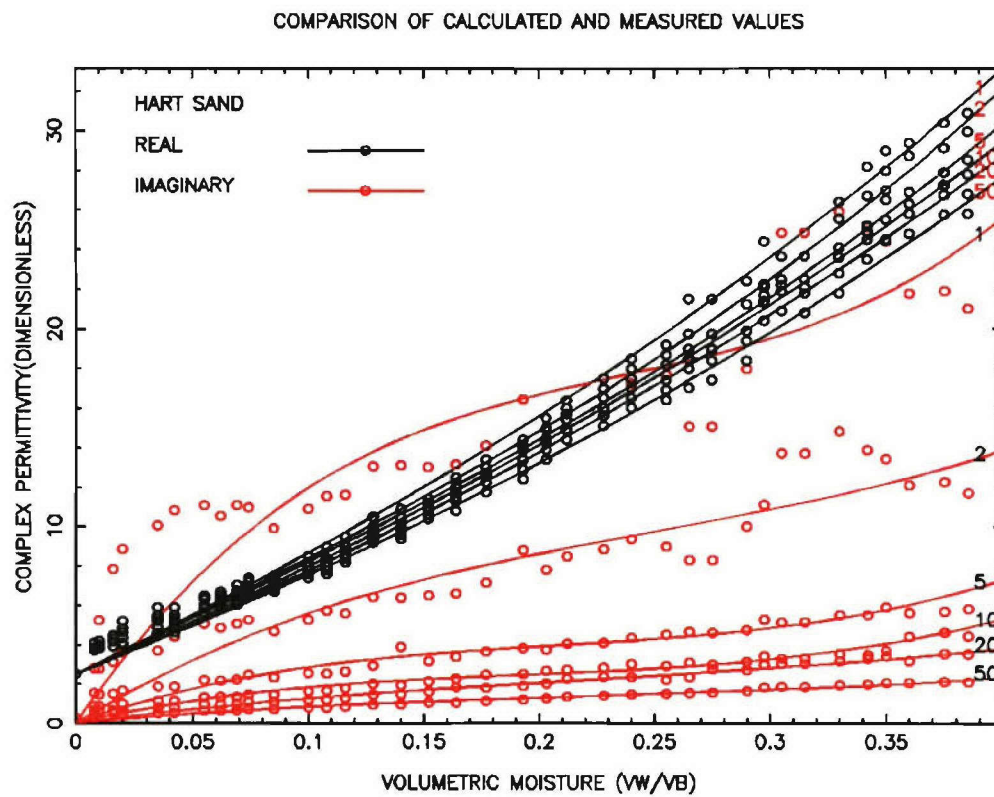
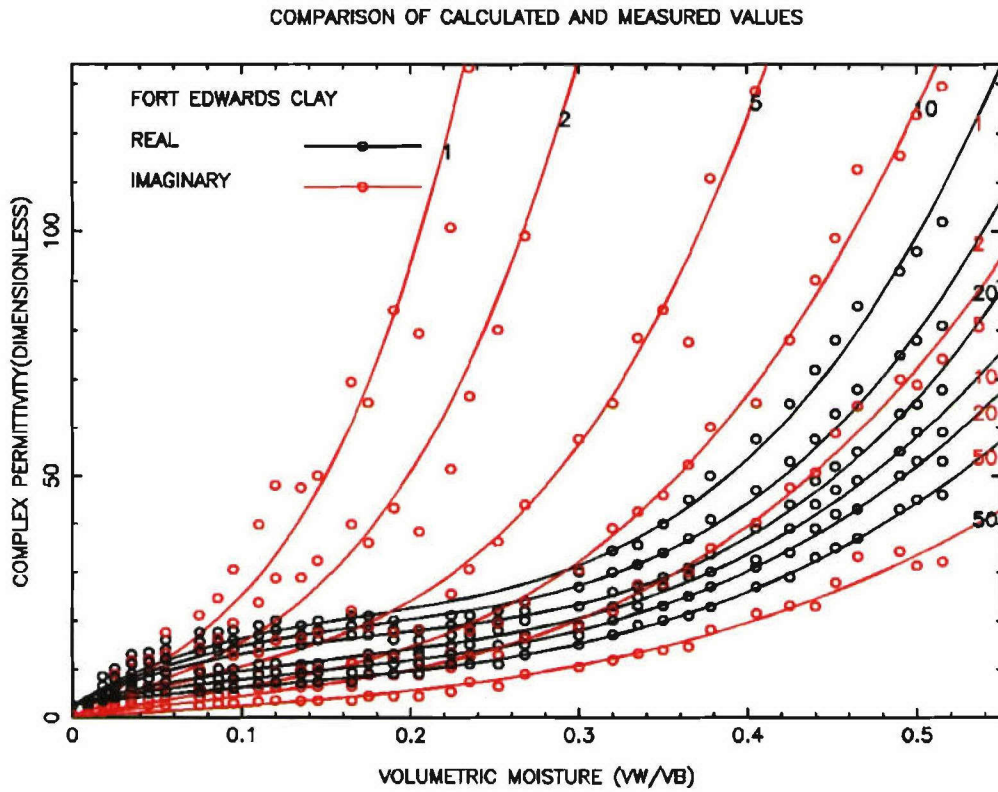


Figure 53





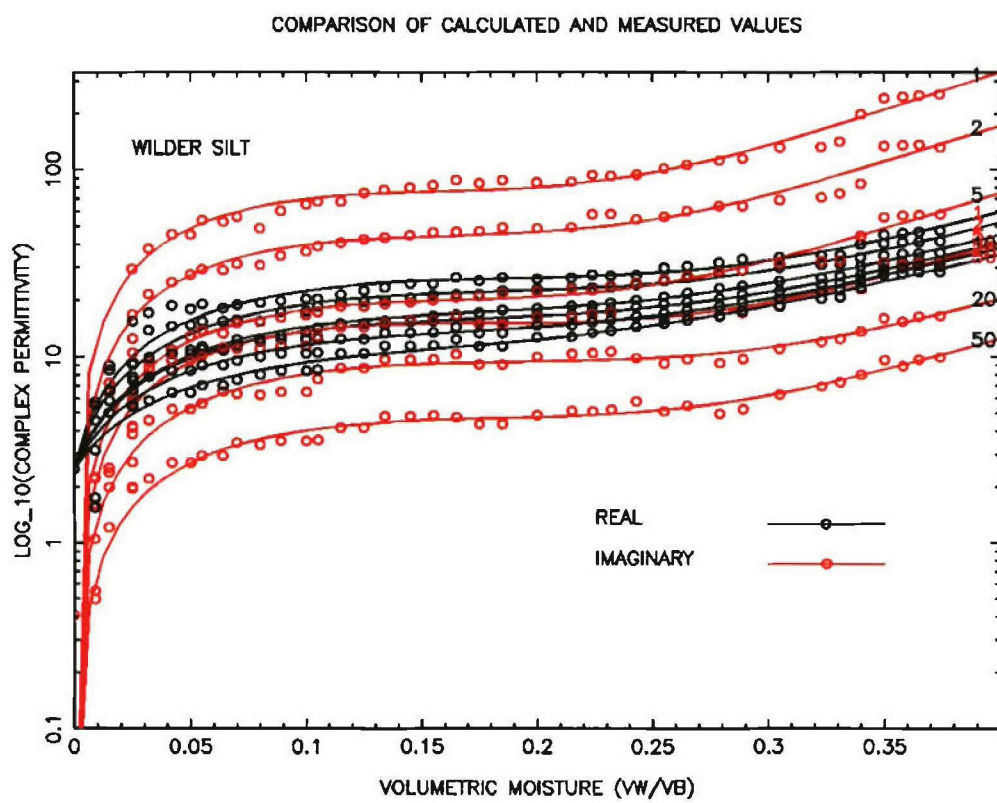


Figure 55

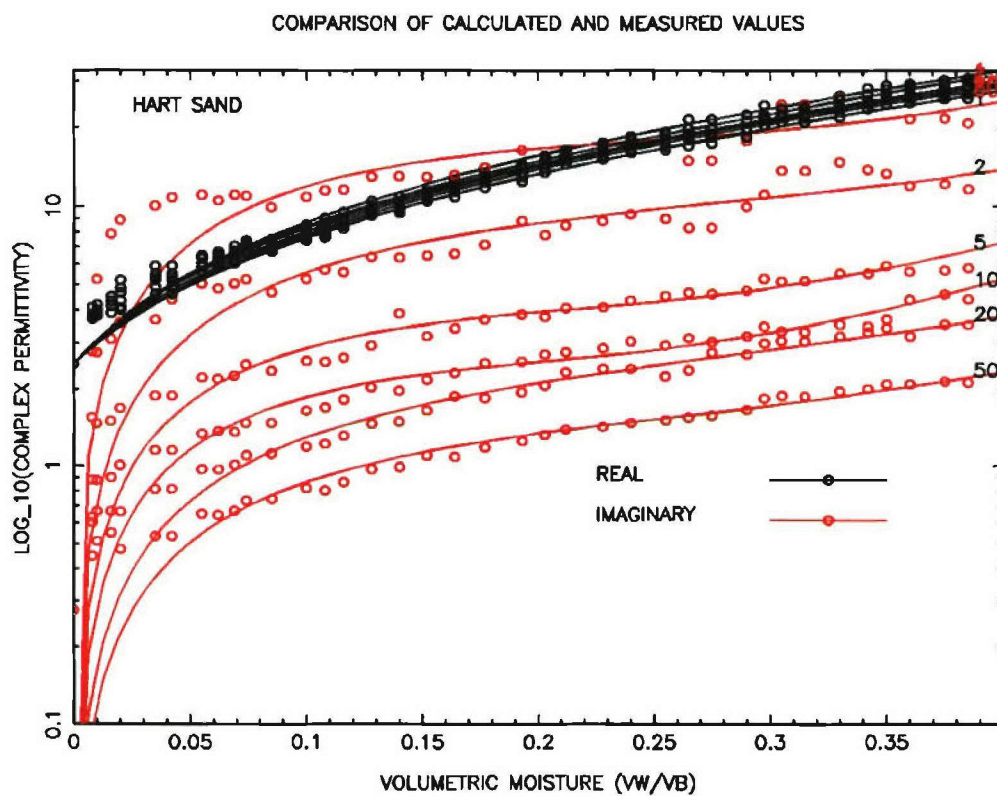


Figure 56

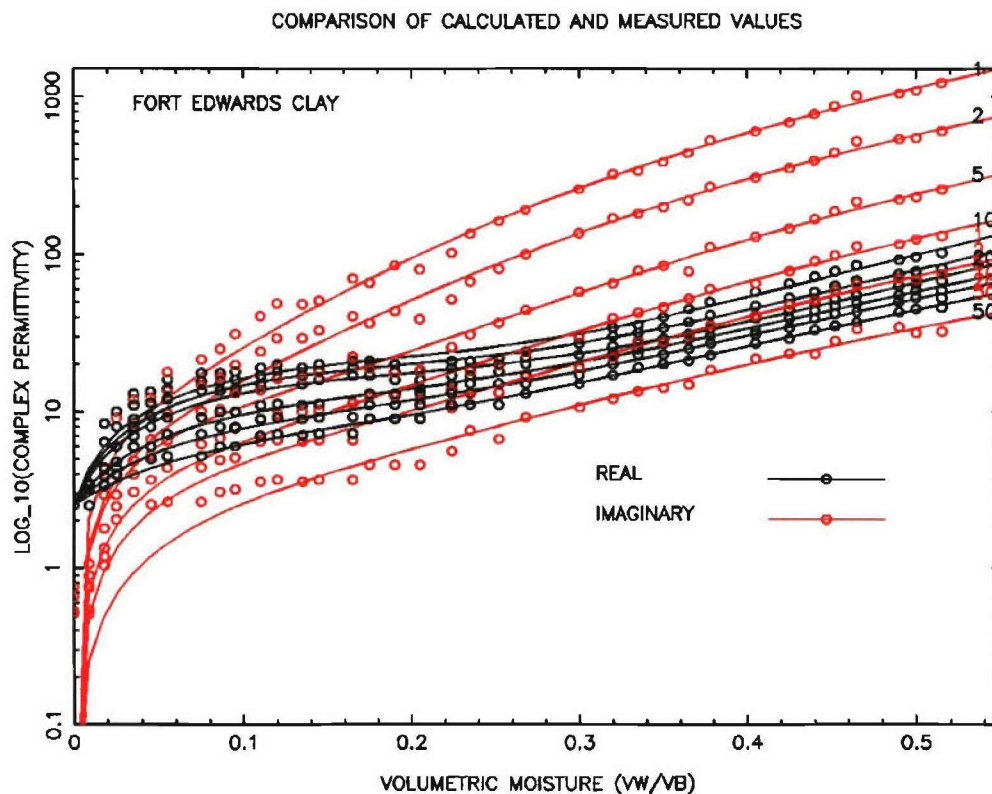


Figure 57

#### 4.4.7. Projected Scaling to Measured Data in the Frequency Range .01-100 MHZ

Since the lower frequency data of Sternberg is only available for each soil considered at a single value of volumetric moisture, the permittivity below 1 MHz was modeled as a scaled projection of the behavior at 1 MHz. The scaling factor is determined by the ratio of the permittivity at the lower frequency and single specified moisture to that at 1 MHz of the same volumetric moisture. The results of the scaled projection of Hart sand and Fort Edward Clay to Sternberg's data below 1 MHz for Brookhaven Sand and Ca-Montmorillonite clay respectively are shown in Figure 58 and Figure 59. Values of the complex permittivity of soils of arbitrary texture at the lower frequencies are obtained by first computing their values at 1 MHz relative to that of the known bounding extremes (sand and clay) at 1 MHz. The absolute values at the lower frequencies are then obtained from the known bounding values at the lower frequency (as obtained from the experimental data) such that the ratios of the permittivity of the arbitrary texture to that of the bounding values (at 1 MHz and at the lower frequency) are preserved.



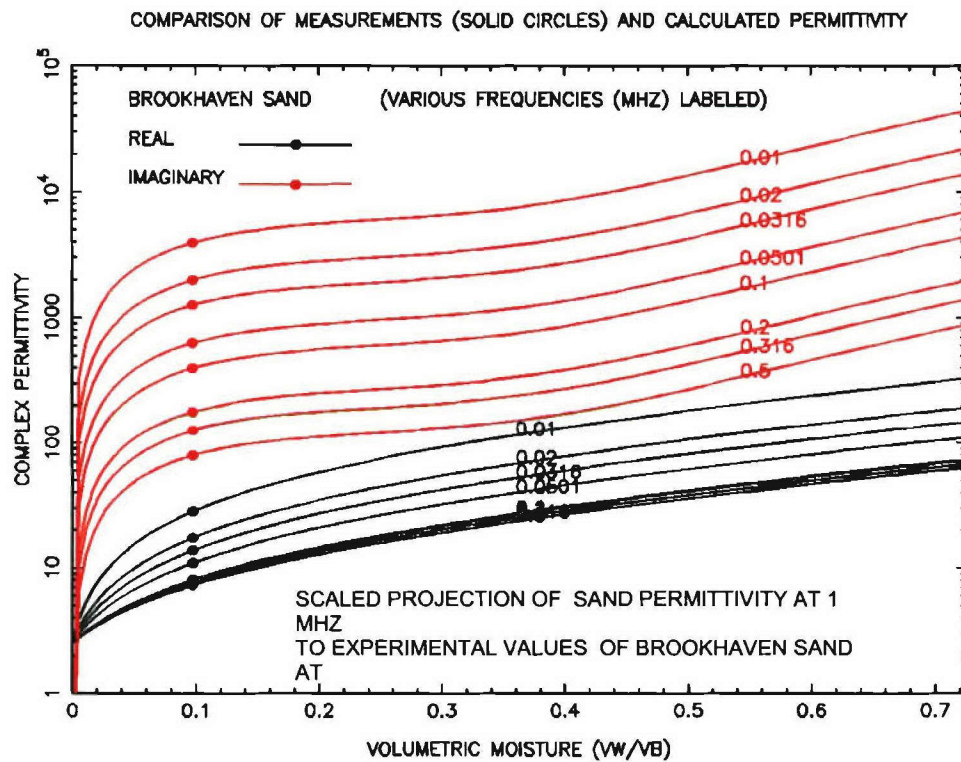
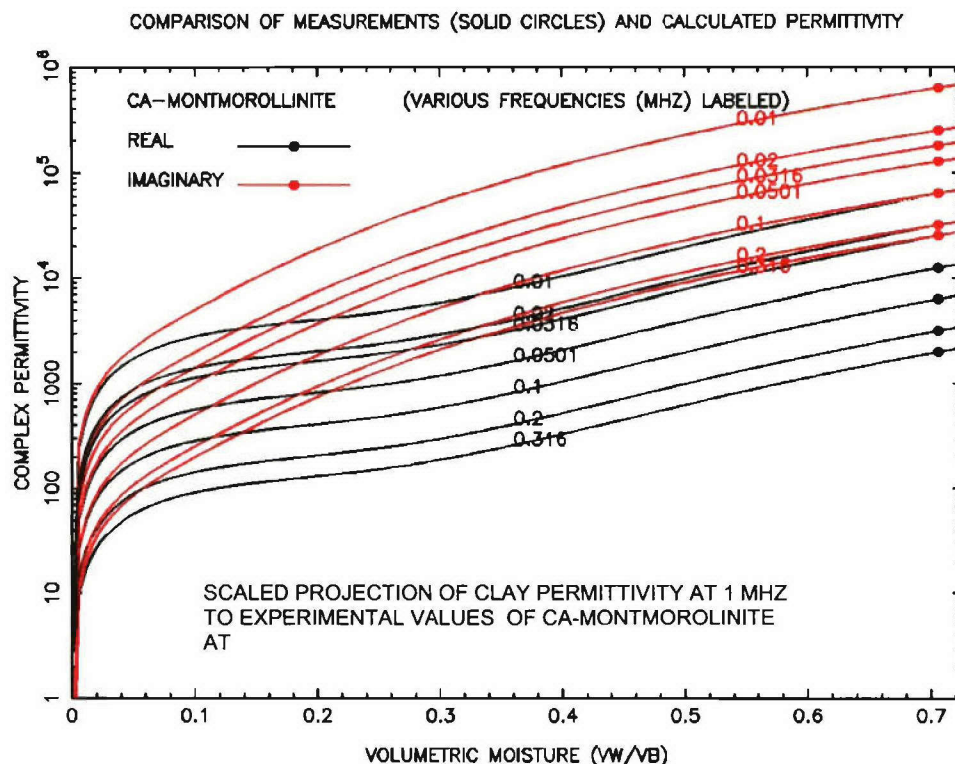


Figure 58



#### 4.4.8. Performance of the Model over Full Frequency

##### 4.4.8.1. Range for Representative Soil Compositions

Plots of both real and imaginary parts of the complex permittivity for each of the five soils considered by Hallikainen and Dobson and for the primary compositions considered by Campbell (using the semi-empirical model above 300 MHz) are shown in Figure 60, Figure 61, Figure 62, Figure 63, Figure 64, Figure 65, Figure 66 and Figure 67. Where explicit data is not available as a function of frequency or between major frequency subdivisions, the (log) of the permittivity is interpolated as a function of the log of frequency using the bounding values of data of the relevant subinterval. The data of Sternberg for Brookhaven sand and for Ca-Montmorollinite is also shown on the two plots corresponding to these respective varieties of soils and are accompanied by the corresponding calculated values computed at the same value of volumetric moisture as the data.

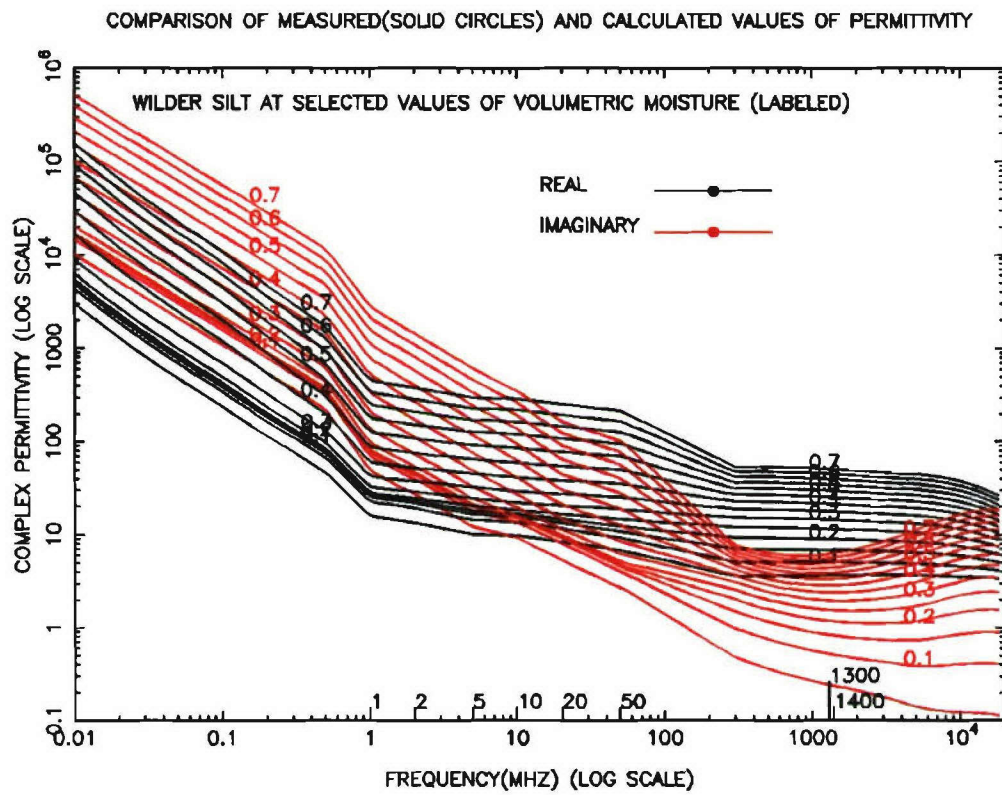


Figure 60



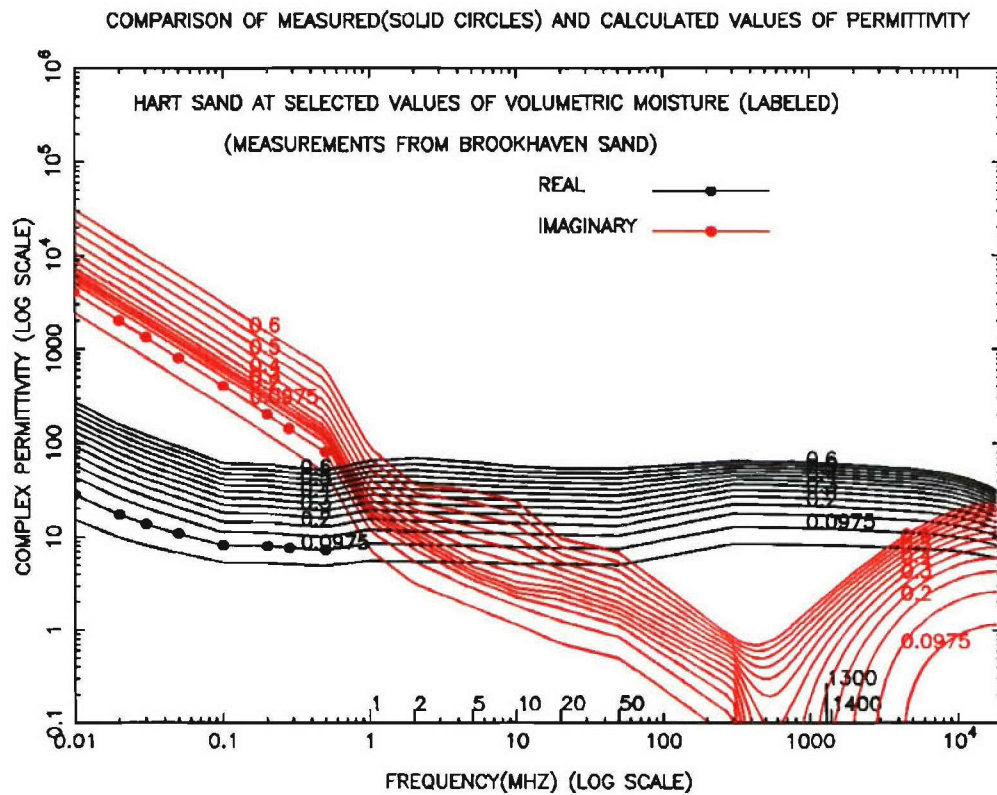


Figure 61

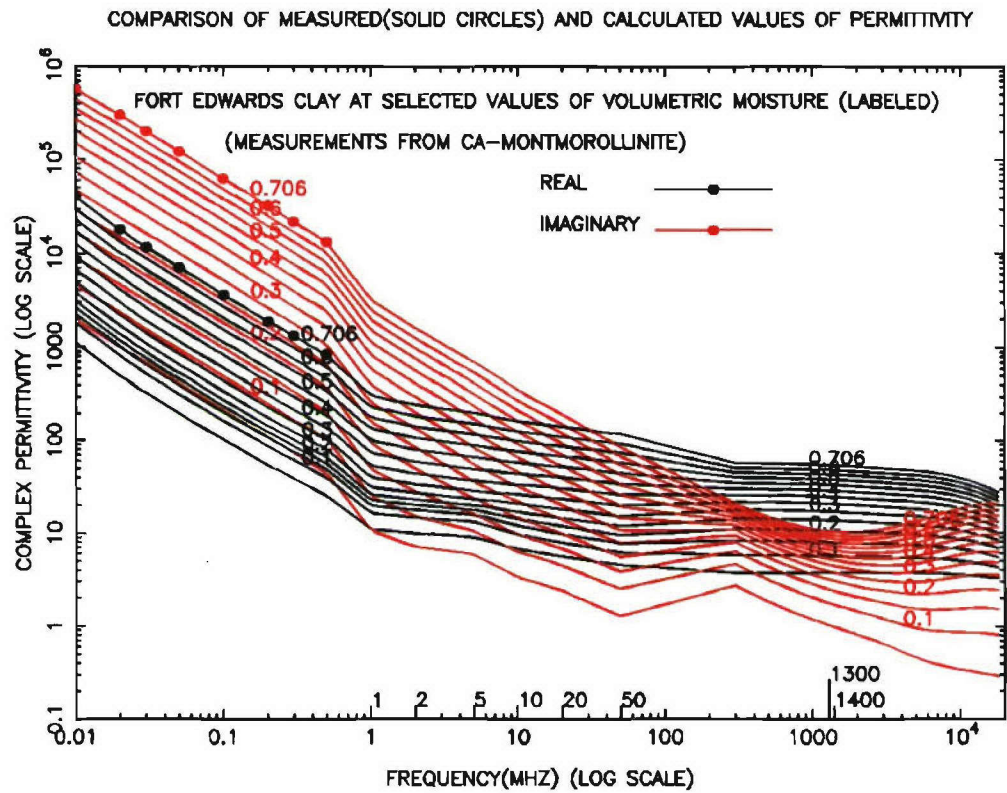


Figure 62

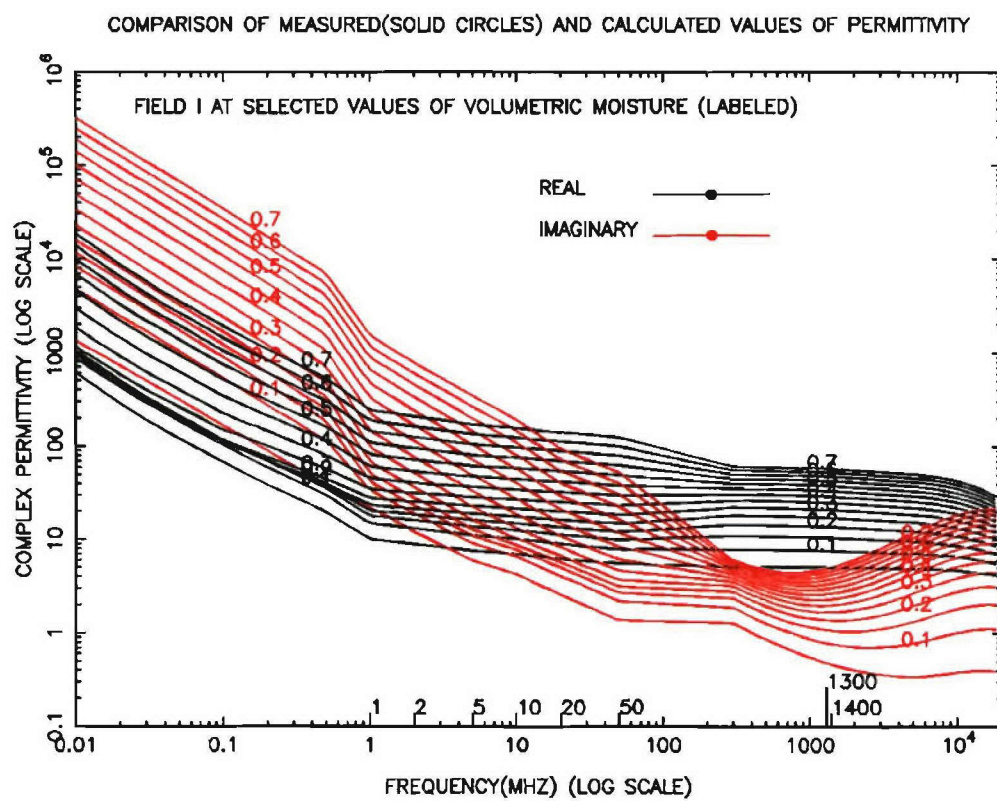


Figure 63



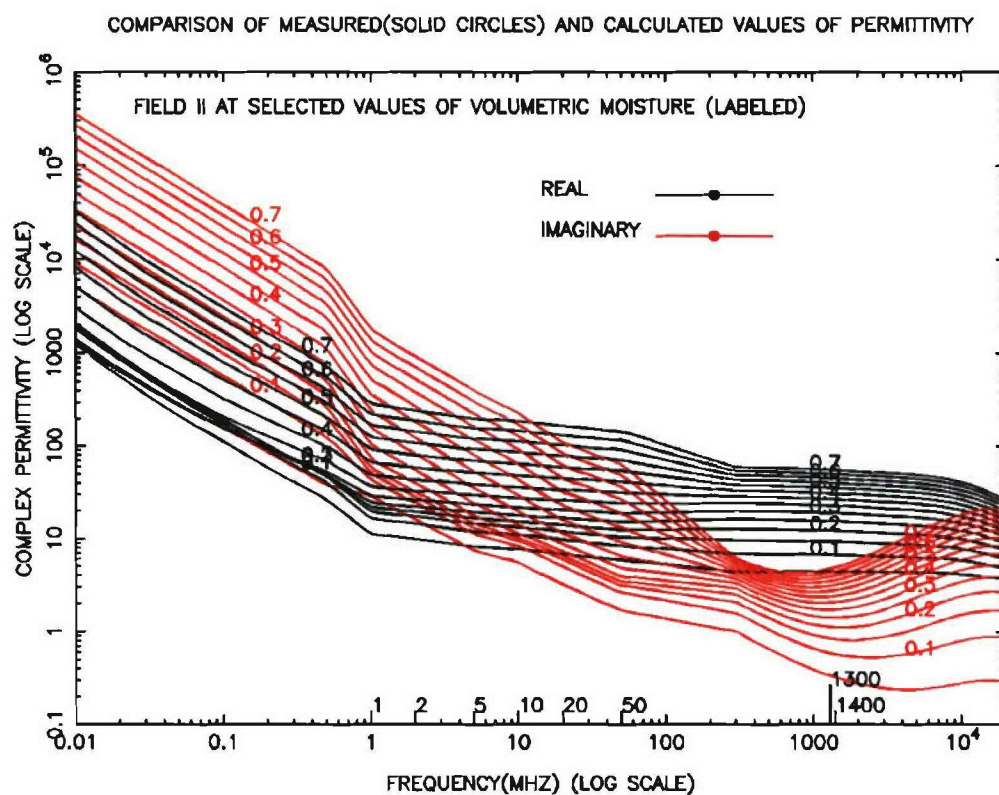


Figure 64

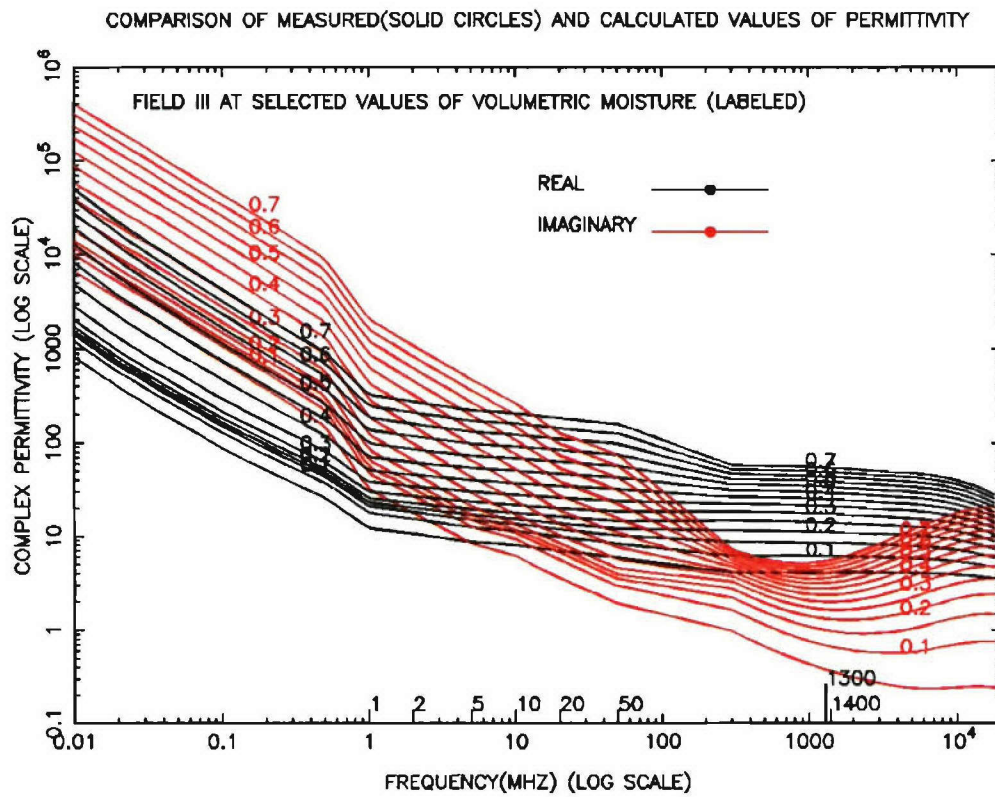


Figure 65

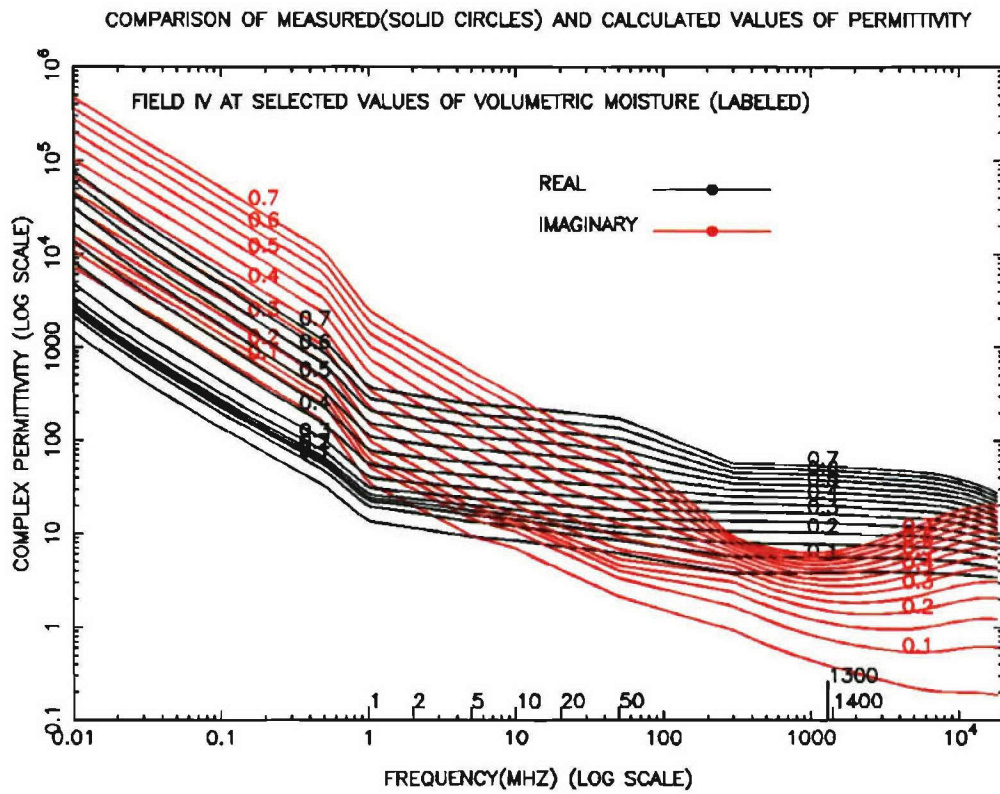
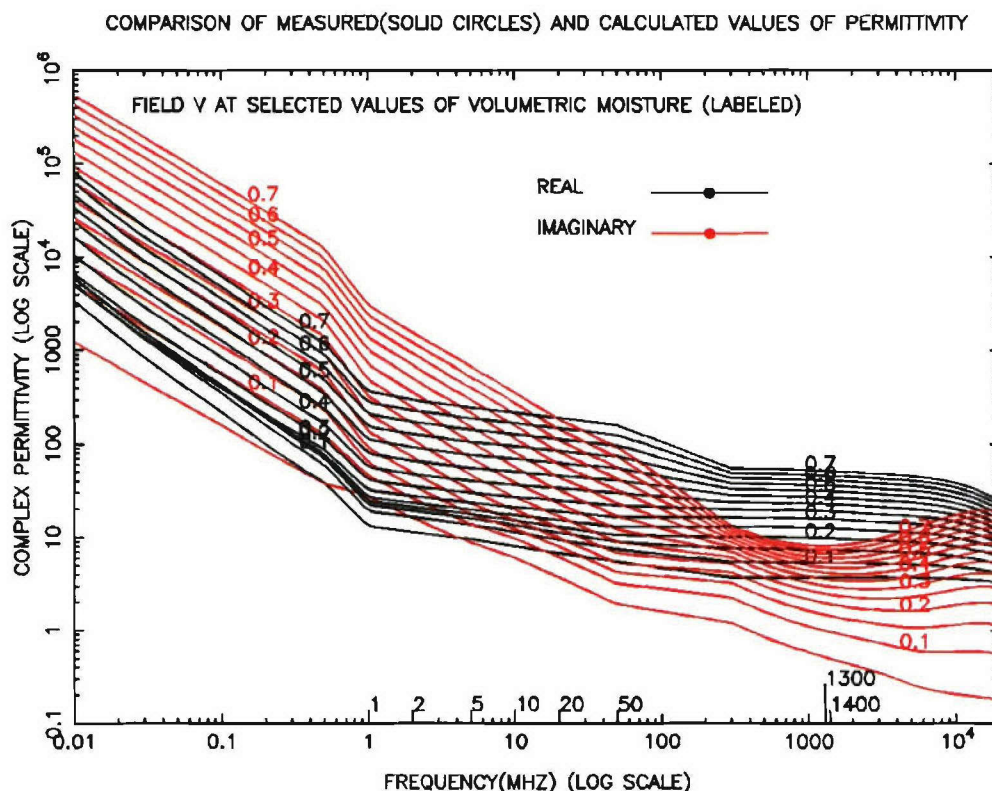


Figure 66



#### 4.4.9. References

- [1]. Boesma, J., On Certain Multiple Integrals Occurring in a Waveguide Scattering Problem, SIAM J. Math. Anal. 9 (2), 377-393 (1978).
- [2]. Felsen, L.B and Marcuvitz, Radiation and Scattering of Waves, Englewood Cliffs, NJ, Prentice-Hall, 652-665 (1973).
- [3]. Holm, P., A New Heuristic UTD Diffraction Coefficient for Non Perfectly Conducting Wedges, IEEE TAP 48(8), 1211-1219 (2000).
- [4]. Kouyoumjian, Robert G. and Pathak, Prabhakar H., A Uniform Geometrical Theory of Diffraction for a Perfectly Conducting Surface, Proc. IEEE 62(11), 1448-1461 (1974).
- [5]. Maciel, L.R., Bertoni, H.L., and Xia, H.H., Unified Approach to Prediction of Propagation Over Buildings for All Ranges and Base Station Antenna Height, IEEE Transaction of Vehicular Technology 42(1), 41-45 (1993).
- [6]. Stuber, G.L., Principles of Mobile Communication, (Second Edition), Kluwer Academic Publishers, 109-110 (2001).



- [7]. Bertoni, H.L., Radio Propagation for Modern Wireless Systems, Prentice Hall PTR, Upper Saddle River, N.J., 147-148, (2000).
- [8]. Walfsch, J. and Bertoni, H.L., A Theoretical Model of UHF Propagation in Urban Environments, IEEE TAP 36(12), 1788-1796 (1988).
- [9]. Epstein, J., and Peterson, D.W., An Experimental Study of Wave Propagation at 850 Mc, Proc. IRE 41(5), 595 (1953).
- [10]. Comparetto, G, Schwartz, J, Schult, N and Marshall, J. "A communication Analysis Tool Set That Accounts for the Attenuation Due to Foliage, Buildings and Ground Effects", The MITRE Corporation
- [11]. Campbell, J.E., Dielectric Properties And Influence Of Conductivity In Soils At One to Fifty Megahertz, Soil Science Society American Journal 54(3),332(1990).
- [12]. Campbell, J.E., *Dielectric Properties of Moist Soils at RF and Microwave Frequencies*, (Doctoral Dissertation, Dartmouth College, 1988), University Microfilms International, Ann Arbor, Michigan (1988)
- [13]. Hallikainen, M.T., Ulaby, F.T., Dobson, M.C., El-Rayes, M.A., and Wu, Lin-Kun, *Microwave Behavior Of Wet Soil, Part I*, IEEE Transactions on Geoscience and Remote Sensing 23(1), 25 (1985)
- [14]. Dobson, M.C., Ulaby, F.T., Hallikainen, M.T., and El-Rayes, M.A., *Microwave Behavior Of Wet Soil, Part II*, IEEE Transactions on Geoscience and Remote Sensing 23(1), 35 (1985)
- [15]. Peplinski, N.R., Ulaby, F.T., and Dobson, M.C., *Dielectric Properties of Soils in the 0.3 -1.3 GHz Range*, IEEE Transactions of Geoscience and Remote Sensing 33(3), 803 (1995)
- [16]. Peplinski, N.R., Ulaby, F.T., and Dobson, M.C., *Corrections to Dielectric Properties of Soils in the 0.3 -1.3 GHz Range*, IEEE Transactions of Geoscience and Remote Sensing 33(3), 803 (1995)
- [17]. Sternberg, B.K., Levitskaya, T.M., Electrical Parameters Of Soils In Frequency Range 1 kHz To 1 GHz Using Lumped Circuit Methods, Radio Science 36(4),709 (2001)